TECHNISCHE UNIVERSITÄT
KAISERSLAUTERN

# AG Magnetismus

Prof. Dr. Burkard Hillebrands

## Annual Report 2007

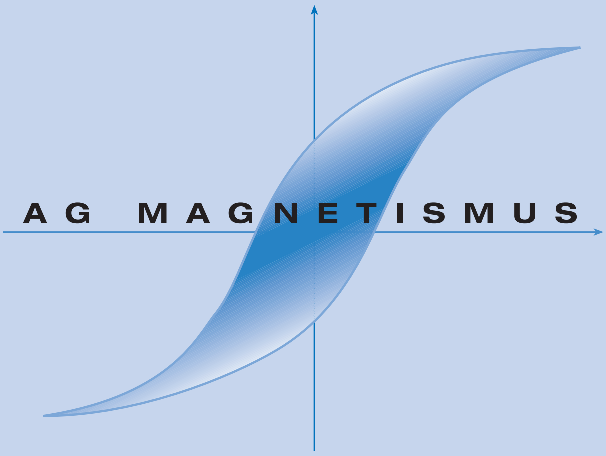

FACHBEREICH PHYSIK

# Annual Report 2007

AG Magnetismus
TU Kaiserslautern

Address: Prof. Dr. Burkard Hillebrands
Fachbereich Physik
Technische Universität Kaiserslautern
Erwin-Schrödinger-Straße 56
67663 Kaiserslautern, Germany
Tel.: +49-(0)631-205-4228
Fax.:+49-(0)631-205-4095

Postal address: Postfach 3049
67653 Kaiserslautern, Germany

Internet: http://www.physik.uni-kl.de/hillebrands/
E-Mail: hilleb@physik.uni-kl.de

# Our Group

From left to right:

Prof. Dr. Burkard Hillebrands, Dieter Weller, Dr. Britta Leven, Helmut Schultheiss, Dr. Patricia Martin Pimentel, Sebastian Hermsdörfer, Christian Sandweg, Dr. Jaroslav Hamrle, Alexander Paul, Sebastian Schäfer, Georg Wolf, Dr. Andreas Beck, Sibylle Müller, Björn Obry, Christopher Rausch, Dr. Andrii Chumak, Florin Ciubotaru, Thomas Schneider, Roland Neb, Dr. Alexander Serga, Dr. Andrés Conca Parra

# Contents

Appendix:

# Chapter 1: Introduction

Dear Colleagues and Friends,

with this report we present our results obtained in the last 12 months, covering the period of November 2006 to October 2007.

Again, we feel this was a very successful year for us. We made several advancements in the field of spin-wave propagation and manipulation, for instance showing that spin waves can be stored and recovered by parametric stimulation. We made further progress in the field of "magnon gases", we continued to work on the understanding of quantized modes in finite ring structure investigating the influence of finite coherency, and we made good progress in understanding the very interesting magnetic properties of Heusler compounds.

A general highlight of this year 2007 is the award of the Nobel Prize to Peter Grünberg and Albert Fert in recognition of their finding of the giant magnetoresistance effect. We are sending our best congratulations to both of them. Concerning Peter Grünberg I am very happy to look back to a long contact with him - we were together running joint projects in the DFG-funded Collaborative Research Centres SFB 125 and SFB 241, 1986–1994, which actually were my first projects funded by the Deutsche Forschungsgemeinschaft. Albert Fert is a member of the EU-Marie Curie Training Network "SPINSWITCH", and he received a honorary doctorate degree of the University of Kaiserslautern last year.

The SPINSWITCH network, which commenced last year, coordinated here in Kaiserslautern, is now up and running, and most young researchers are hired and contribute to the work in the network.

This year a new Transregional Collaborative Research Center "Condensed matter systems with variable many-body interactions" has been granted by the Deutsche Forschungsgemeinschaft. Researchers from the Universities of Frankfurt, Kaiserslautern and Mainz are working together to understand complex order phenomena caused by the interaction of a large number of quantum objects. Study objects are systems of variable complexity ranging from quantum simulators to real materials. We contribute with work on magnon gases as a model system, which is very suited to study correlation effects between bosons.

Intensive collaborations have been put forward with groups in Japan, in particular with the groups of Y. Ando at Tohoku University, Sendai and, since recently, with Y. Otani at Riken, Tokyo. Building on a joint JST-DFG funded workshop in November 2006, projects have been granted which are co-funded by both funding agencies of Germany and Japan, DFG and JST. With the group of Y. Ando exchange of students works very well - Sebastian Hermsdörfer and Oksana Gaier from my group spent several months in Sendai, and we were happy to have Takahide Kubota visiting us.

The field of physics of Heusler alloys is very well progressing. The proposal for the next three-year funding period of our joint Mainz-Kaiserslautern Research Unit "New materials with high spin polarization" was positively evaluated, and the group of Y. Ando at Tohoku University, Sendai was accepted as a new member - the first Japanese group joining a DFG-funded German Research Unit.

Our long-time technician Bernd Pfaff went on retirement. We wish him all the best for his new life as a retiree. We are happy to welcome his successor, Alexander Paul, as a new member of the group.

Many new people joint the group. They are Andrii Chumak, Andrés Conca Parra, Abdelghani Laraoui (Postdocs), and Florin Ciubotaru and Roland Neb (Ph.D. students). Sebastian Schäfer started his Ph.D. after completing his Diploma.

Our work would not have been possible without valuable collaborations with people all over the world. They are too many to list them here all. In particular we would like to thank, in alphabetical order, Yasuo Ando, Christian Back, John Chapman, Claude Chappert, Oksana Chubykalo-Fesenko, Darrell Comins, Russell Cowburn, Vladislav Demidov, Sergej Demokritov, Bernard Dieny, Günter Dumpich, Hajo Elmers, Jürgen Fassbender, Gerhard Fecher, Claudia Felser, Claude Fermon, Jacques Ferré, Albert Fert, Suzanna and Paulo Freitas, Hubert Grimm, Kouichiro Inomata, Gerhard Jakob, Martin Jourdan, Boris Kalinikos, Matthias Kläui, Mikhail Kostylev, Liesbet Lagae, Jürgen Langer, Norbert Laube, Wolfram Maaß, Jan Marien, Roland Mattheis, Andrezj Maziewski, Gennadiy Melkov, Jacques Miltat, Alexandra Mougin, Fabrizio Nizzoli, Yoshichika Otani, Carl Patton, Dorothée Petit, Kamil Postava, Günter Reiss, Karsten Rott, Ulrich Rüdiger, John R. Sandercock, Rudi Schäfer, Gerd Schönhense, Andrei Slavin, Bob Stamps, André Thiaville and Stefan Visnovsky for their interactions with us and their strong input to our work.

Collaborations within the Fachbereich Physik at the University of Kaiserslautern (in particular Martin Aeschlimann, James Anglin, Sebastian Eggert, Michael Fleischhauer, Egbert Oesterschulze, Hans-Christian Schneider, Volker Schünemann, Herbert Urbassek, Christiane Ziegler and their groups), the Institut für Oberflächen- und Schichtanalytik, as well as the Nano+Bio Center have been very stimulating. I am especially grateful to Heinz Busch and Udo Grabowy and their start up company NTTF GmbH for the close contact. I am much obliged to Peter Pesch and his team from the TZO GmbH for providing convenient general conditions for our work in Rheinbreitbach.

I would also like to thank all our sponsors, which are the Deutsche Forschungsgemeinschaft, the Bundesministerium für Bildung und Forschung, the Humboldt Foundation, the Deutscher Akademischer Austauschdienst, the European Community, INTAS, NEDO, the State of Rheinland-Pfalz and the University of Kaiserslautern. My special thanks go to Andreas Beck and Sibylle Müller for their help in preparing this report and to Hubert Gerber from Photo-Repro-Druck, TU Kaiserslautern.

It is my special pleasure to greet all former group members. May this report help to stay in touch with each other.

If you are interested in our work I would be happy to hear from you. If you have any questions, comments, suggestions, or any kind of criticism, please contact us.

With all my best wishes for Christmas, and a Happy New Year,

Burkard Hillebrands

Kaiserslautern, November 2007

# Chapter 2: Personnel

## 2.1 Members of the group

### Group leader:

Prof. Dr. Burkard Hillebrands

### Senior scientists:

Dr. Britta Leven, Akad. Rätin
Dr. Jaroslav Hamrle
Dr. Alexander Serga

### Postdocs and long-term guest scientists:

| | |
|---|---|
| Dr. Andreas Beck | since 10/07 |
| Dr. Steffen Blomeier | until 06/07 |
| Dr. Patrizio Candeloro | until 05/07 |
| Dr. Andrii Chumak | since 06/07 |
| Dr. Andrs Conca Parra | since 08/07 |
| Dr. Abdelghani Laraoui | since 10/07 |
| Dr. Patricia Martin Pimentel | since 07/07 |
| Dr. Seong-Gi Min | until 08/07 |
| Dr. Natalia Sergeeva | until 04/07 |

### PhD students:

| | |
|---|---|
| Dipl.-Phys. Andreas Beck | until 09/07 |
| Dipl.-Phys. Sebastian Becker | until 11/06 |
| Dipl.-Phys. Steffen Blomeier | until 02/07 |
| Dipl.-Phys. Ulla Böde (Rheinbreitbach) | until 10/07 |
| Dipl.-Phys. Florin Ciubotaru | since 09/07 |
| Dipl.-Phys. Oksana Gaier | |
| Dipl.-Phys. Sebastian Hermsdörfer | |
| Dipl.-Phys. Lisa Kleinen (Rheinbreitbach) | |
| Dipl.-Phys. Patricia Martin Pimentel | until 06/07 |
| Dipl.-Phys. Roland Neb | since 08/07 |
| Dipl.-Math. Timo Neumann | |
| Dipl.-Phys. Maciej Oskar Liedke | until 05/07 |
| Dipl.-Phys. Sebastian Schäfer | since 08/07 |
| Dipl.-Phys. Thomas Schneider | |
| Dipl.-Phys. Helmut Schultheiss | |

### Diploma Students:

| | |
|---|---|
| Christian Sandweg | until 09/07 |
| Sebastian Schäfer | until 07/07 |
| Georg Wolf | until 09/07 |

## Erasmus student:

| | |
|---|---|
| Ewelina Sieczkowska | since 10/07 |

## Engineers and Technicians

| | |
|---|---|
| Jörg Elmer (Rheinbreitbach) | |
| Alexander Paul | since 08/07 |
| Bernd Pfaff | until 03/07 |
| Dipl.-Ing. (FH) Dieter Weller | |

## Secretary:

Sibylle Müller

## 2.2 Visiting scientists, postdoctoral fellows and exchange students

**Prof. Boris Kalinikos**, Electrotechnical University St. Petersburg,
St. Petersburg, Russia 15.05.07 - 17.05.07

Boris was visiting us for a short period. He was participating in discussions on nonlinear dynamics of short spin-wave packets in closed active loops in the frame of the ongoing work on our joint DFG Project 436 RUS 113/644/0-2 "Kohärente nichtlineare Spinwellenzustände in ferromagnetischen Filmen und ferromagnetisch/ferroelektrischen Schichtstrukturen". In May 2007 the preparation of the new project as well as possible future joint investigations were additionally discussed.

**Takahide Kubota**, Department of Applied Physics,
Graduate School of Engineering, Tohoku University, Sendai, Japan 27.09.07 - 24.10.07

His stay in Kaiserslautern is a continuation of a collaboration and student exchange between Sendai and Kaiserslautern, as from our group students Oksana Gaier and Sebastian Hermsdörfer have spend several month in Sendai. The collaboration with Tohoku is run within the Research Unit 559 *"New materials with high spin polarization"* funded by the Deutsche Forschungsgemeinschaft and by the NEDO International Joint Research Grant Programm 2004/T093. Takahide's project in Kaiserslautern was investigation of magnetic properties in $Co_2MnAl_xSi_{1-x}$ Heusler compound using MOKE and BLS technique.

**Elvira Paz**, Instituto de Ciencia de Materiales de Madrid (ICMM),
Madrid, Spain 01.03.07 - 31.08.07

Elvira was staying with us to work on Brillouin light scattering spectroscopy of spin-wave dynamics in structured metallic magnetic films. She also was involved in magneto optical Kerr effect measurements with time resolution and microwave assisted switching experiments during her stay.

**Dr. Ryszard Gieniusz**, University of Bialystok, Poland 27.04.07 - 25.05.07
17.08.07 - 15.09.07

Ryszard visited our group as a visiting scientists, coming from the group of Prof. Andrzej Maziewski. In our group he studied the phonon properties of thin Co films using Brillouin light scattering spectroscopy.

**Prof. Andrei Slavin**, University of Rochester, Michigan, U.S.A. 15.05.07 - 16.06.07

Andrei's stay was supported by our Graduate School ("Graduiertenkolleg"). He delivered a course of lectures on nonlinear spin-wave effects as well as on microwave spin-torque phenomena. During his visit he also was working on theoretical description of nonlinear behavior of standing spin-wave modes in thin ferrite films.

**Prof. Gennadiy Melkov**, National Taras Shevchenko
University of Kiev, Ukraine 10.07.07 - 31.07.2007

Gennadiy's visit was supported by the Deutsche Forschungsgemeinschaft in the frame of SFB/Transregio-49 project "Condensed Matter Systems with Variable Many-Body Interactions". Gennadiy was focusing on experimental and theoretical study of collective effects and instabilities of a magnon gas caused by a strong parametric electromagnetic pumping.

## 2.3 Guest seminars

| | |
|---|---|
| Dr. Sabine Wurmehl<br>04.12.2006 | Johannes Gutenberg-Universität, Mainz<br>*Spin polarised Heusler compounds*<br>Seminar |
| Nicolas Biziere<br>19.01.2007 | CEA, Grenoble, France<br>*Detection of hyperfrequencies with magnetoresistive sensors*<br>Sonderseminar |
| Federico Cebollada Baratas<br>14.05.2007 | ETSIT-UPM, Madrid, Spain<br>*Coercivity mechanisms of magnetic antidots and stripes arrays*<br>Sonderseminar |
| Prof. Dr. A. Slavin<br>21.05.2007 | University of Rochester, USA<br>*Nonlinear magnetic relaxation in a non-ideal magnon gas*<br>Sonderseminar |
| Prof. Dr. H.C. Schneider<br>26.07.2007 | TU Kaiserslautern<br>*Lateral spin transfer phenomena*<br>Sonderseminar |

## 2.4 Visits of group members at other laboratories

| | |
|---|---|
| Sebastian Hermsdörfer | Tohoku University, Sendai, Japan<br>19.07-17.12.06<br>Host: Prof. Y. Ando |
| Patricia Martín Pimentel | IMEC, Leuven, Belgium<br>27.11-01.12.06<br>Host: Dr. L. Lagae |
| Patricia Martín Pimentel | IMEC, Leuven, Belgium<br>06.12-08.12.06<br>Host: Dr. L. Lagae |
| Steffen Blomeier | Imperial College, London, United Kingdom<br>18.01-22.01.07<br>Host: Prof. R.P. Coburn |
| Oksana Gaier | Tohoku University, Sendai, Japan<br>01.09-17.12.07<br>Host: Prof. Y. Ando |

## 2.5 Group member photo gallery

Dr. Andreas Beck
Postdoc

Sebastian Becker
Ph.D. student

Dr. Steffen Blomeier
Postdoc

Ulla Böde
Ph.D. student

Dr. Patrizio Candeloro
Postdoc

Dr. Andrii Chumak
Postdoc

Florin Ciubotaru
Ph.D. student

Dr. Andrés Conca Parra
Postdoc

Jörg Elmer
Technician

Oksana Gaier
Ph.D. student

Dr. Jaroslav Hamrle
Senior scientist

Sebastian Hermsdörfer
Ph.D. student


Prof. Dr. Burkard Hillebrands
Group leader


Lisa Kleinen
Ph.D. student


Dr. Abdelghani Laraoui
Postdoc


Dr. Britta Leven
Senior scientist


Maciej Oskar Liedke
Ph.D. student


Patricia Martín Pimentel
Ph.D. student


Dr. Seong-Gi Min
Postdoc


Sibylle Müller
Secretary


Roland Neb
Ph.D. student


Timo Neumann
Ph.D. student


Alexander Paul
Technician


Bernd Pfaff
Technician


Christian Sandweg
Diploma student


Sebastian Schäfer
Ph.D. student


Thomas Schneider
Ph.D. student


Helmut Schultheiss
Ph.D. student


Dr. Alexander Serga
Senior scientist


Dr. Natalia Sergeeva
Postdoc


Ewelina Sieczkowska
Erasmus student


Dieter Weller
Mechanical engineer


Georg Wolf
Diploma student

# Chapter 3: Research Topics

The field of magnetism in films and multilayers is still a strongly developing area in modern solid state physics. This is caused both by the challenging developments in the discovery and understanding of the basic physical phenomena, and by the strong impact into industrial applications in the areas of sensors and information storage technology. New mechanisms like interlayer exchange coupling, the giant magnetoresistance effect, the room-temperature tunneling magnetoresistance effect, and, since very recently, spin current phenomena were discovered all within the last one and a half decade. Applications based on these effects were developed, like the magnetic read head based on the giant magnetoresistance effect found in nearly every hard disk drive sold nowadays. The combination with microelectronics, the so-called field of magneto-electronics is strongly expanding and bridging the gap between conventional magnetism and semiconductor physics in view of potential applications in sensor devices and magnetic random access memories, as well as new fields such as magnetic logic.

Most of our research projects are in this field. A main focus is on spin dynamics. We study the eigen-frequency spectrum of excitations of the magnetization on the frequency scale using the Brillouin light scattering technique, and the temporal evolution by time resolved magneto-optic methods. We investigate high frequency properties like spin waves, time dependent magnetization effects, and fast magnetic switching. Recently, our focus shifted strongly towards transport phenomena using linear and nonlinear spin waves.

A key issue is the fabrication of high-quality epitaxial film and multilayer systems and devices using molecular beam epitaxy as prototype systems to study fundamental problems.

In the field of applications we address problems of fast magnetic switching and the exchange bias effect. We transfer our results into actual devices by working closely together with industrial partners.

Magnetic films are very attractive and versatile nonlinear media. Considering spin waves in films as one example of nonlinear waves we study nonlinear effects which are of a great importance for nonlinear science in general.

As a second working area we develop and investigate carbon films for medical applications in the framework of the Institute for Thin Film Technology in Rheinbreitbach.

## Overview on projects

### 1) Epitaxial magnetic films and multilayers: growth, structure and magnetic properties

The preparation of samples with highest possible structural quality and characterization is very important to be able to study magnetic phenomena with the required precision. We achieve this by using molecular beam epitaxy employing the standard *in-situ* methods for chemical and structural analysis. They comprise Auger spectroscopy for chemical analysis, low and high energy electron diffraction, and *in-situ* scanning tunneling and atomic force microscopy. To characterize the magnetic properties we perform *in-situ* Brillouin light scattering spectroscopy and magneto-optic Kerr effect magnetometry. *Ex-situ*, the samples are investigated using Brillouin light scattering spectroscopy, vector Kerr magnetometry, vibrating sample magnetometry, and more. Scientific subjects are magnetic anisotropies induced at interfaces and by controlled defects, and interlayer coupling effects between magnetic films in multilayers. Special attention is paid to the interplay between the morphology at the interfaces (atomic defects, steps, roughness and interdiffusion) and the magnetic properties.

### 2) Heusler compounds

Studies of ferromagnetic half-metals are a very interesting topic now for their possible applications in spintronic devices as a potential source of a 100 % spin-polarized current. Heusler alloys are promising candidates for these applications due to their high Curie temperature and expected half-metallicity even for partially disordered systems. Our studies of Heusler compounds are made within the Research Unit (Forschergruppe) 559 “New Materials with High Spin Polarization”. Within this network, our main goals are:

- To investigate magnetic properties of Heusler compounds, such as exchange stiffness constant, anisotropy energies, magnetization reversal mechanism as well as magnetic and magneto-optical properties. The main techniques used for those studies are Brillouin light scattering spectroscopy and magneto-optic Kerr effect magnetometry.
- To study the modification of the properties of Heusler compounds using ion irradiation. For this purpose we own a $He^+$ ion irradiation system. Furthermore, we have a fruitful collaboration with the IFOS, Technische Universität Kaiserslautern and with the Forschungszentrum Dresden-Rossendorf, Dresden (Dr. Jürgen Fassbender). In general, ion irradiation is a very powerful tool to modify magnetic properties of ferromagnets as it allows tuning of magnetic properties as anisotropy, exchange etc. in a controlled way. Furthermore, those changes can be applied with high lateral resolution, below 100 nm.

### 3) Surface smoothing

It is very important to fabricate films and multilayers with maximum degree of smoothness. Undesirable roughness, for example, results in a reduced figure of merit in magnetoelectronic devices. We develop a technology to smooth surfaces of films after their preparation. For this purpose we use low-energy beams of argon ions. Mono-energetic, low-energy ions allow for a very controllable smoothing process of the surface without creation of an essential number of defects.

### 4) Dynamic magnetic properties of laterally patterned nanostructures

We investigate the basic magnetic properties of systems patterned on the micrometer to nanometer scale. In particular we focus on the domain structure and the change in the spin wave mode spectrum due to lateral confinement effects. We have developed a Brillouin light scattering setup, operating in a Fourier microscope like mode, to obtain sub-micrometer scale spatial information about the distribution of dynamic excitations in small magnetic objects. We also developed a micro-focus Brillouin light scattering system to investigate single magnetic elements. Using these methods we have observed lateral quantization of spin waves in magnetic stripes and rectangular elements. Main results are the observation of quantized modes and of edge modes existing in areas with a large internal field gradient, and static and dynamic coupling effects between magnetic objects. The experiments are accompanied by numerical simulations. A new area is the spin-wave tunneling effect and applications to spin wave logic.

### 5) Nonlinear properties of high-amplitude spin waves

Spin waves with high precession angles are an interesting object for the investigation of general effects of nonlinear wave propagation in dispersive, anisotropic, and dissipative media. Contrary to nonlinear optical pulses, the spectrum of spin waves can be easily manipulated, by, e.g., changing the orientation and the value of the applied magnetic field. In addition spin waves are much slower than light pulses making their observation easier.

Using the time-resolved Brillouin light scattering technique developed in our lab, we measure the intensity distribution of spin waves propagating in a magnetic film with spatial and temporal resolution. Central problems are: the amplification of spin waves in the linear and nonlinear intensity regimes, the formation of instabilities (e.g. self-focusing), the propagation of nonlinear excitations (solitons, magnetic “bullets”) and excitations in nonlinear media with a nontrivial topology such as rings. An important development of these studies is the investigation of self-generation of solitons and bullets in loops with an electronic feedback, the development of a spin wave soliton “laser”, and the discovery of symmetry-breaking spin wave modes like the “Möbius” solitons.

### 6) Fast magnetic switching

For memory devices it is of special importance how fast and secure magnetic domains can be written and the magnetization of a single magnetic object can be reversed. The corresponding time scale is in the picosecond to nanosecond regime. In order to investigate these phenomena a time-resolved scanning magneto-optic Kerr microscope has been constructed. The time evolution of the magnetization is sensed stroboscopically. The magnetization dynamics, spin wave propagation effects and in particular the switching behavior of thin magnetic films and nanostructures are investigated.

### 7) Magnetic nanopatterning

Ion irradiation is an excellent tool to locally modify magnetic properties on the sub-micrometer scale, without substantially affecting the surface topography. This effect is used to magnetically pattern ultrathin films and multilayers using resist masks patterned by electron beam lithography. The major difference between this technique and conventional lithographic techniques is that the environment of the nanostructures can also be magnetic (paramagnetic, antiferromagnetic). A focus is on coupled magnetic systems, such as exchange bias bilayers and exchange coupled trilayers.

### 8) Exchange bias systems

The investigation of exchange bias systems is of fundamental as well as technological importance. The effect is a shift of the hysteresis loop along the field axis, and it appears in multilayers of coupled ferromagnetic and antiferromagnetic films. In particular we study structurally well characterized epitaxial bilayers. The role of defects and interfacial mixing is investigated using ion irradiation in order to artificially create disorder. Ion irradiation techniques are also applied to modify the magnitude and direction of the exchange bias field. TEM studies are carried out to investigate the structural and magnetic properties as well as their dependency on the irradiation with He$^+$ and Ga$^+$ ions. A picosecond all-optical pump-probe setup was developed to study thermal activated unpinning of the exchange coupling at the FM/AF interface. This is of high technological interest, especially for magnetic sensor and storage applications.

### 9) Biofunctionalized surfaces for medical applications

Amorphous thin carbon films are known to be very biocompatible, and they can be prepared by various deposition techniques to qualify for miscellaneous applications in the biological and medical field. At the Institute for Thin Film Technology we develop in close collaboration with our spin off company NTTF GmbH biocompatible and biofunctionalized surfaces for medical implants, surgical instruments and cellbiological equipment. Currently we are working on carbon coatings for endwelling catheters and cell culture dishes (both made of temperature sensitive polymers) as well as on the development of diffusion barrier coatings on polymers.

# Chapter 4: Equipment

## A) Preparation and characterization of thin films and multilayers

1. multi–chamber molecular beam epitaxy system (Pink GmbH) comprising
    a. deposition chamber
    (electron beam and Knudsen sources, RHEED, LEED, Auger)
    b. scanning tunneling and needle sensor microscopy chamber
    (*in-situ* STM/needle AFM, Omicron)
    c. Brillouin light scattering and Kerr magnetometry chamber
    (magnetic field 1.2 T, temperature range 80 – 400 K)
    d. load lock chamber
    e. preparation chamber
    (optical coating, heating station 2300°C)
    f. transfer chamber
    g. atom beam reactor chamber with *in-situ* four point probe resistance measurement stage
2. two-chamber UHV multideposition system
    a. deposition chamber
    (electron beam and Knudsen sources, LEED, Auger)
    b. ion beam chamber with fine focus noble gas keV ion source (Omicron), ion beam oxidation module and mask system
3. two-magnetron sputtering system for hard coatings
4. atomic force microscope (Solver, NT-MDT)
5. clean room facility with flow box, spin coater, etc.

## B) Magnetic characterization

1. vector Kerr magnetometer
(longitudinal and transverse Kerr effect, magnetic field 1.2 T, temperature range 2 – 350 K, automated sample positioning)
2. time-resolved vector Kerr magnetometer (10 ps time resolution and microwave setup for generation of short field pulses)
3. scanning Kerr microscope with time resolution
4. picosecond all-optical pump-probe setup (adjustable delay up to 6 ns; ps-laser Lumera Lasers GmbH)
5. magnetic force microscope with magnet (NT-MDT)
6. two Brillouin light scattering spectrometers, computer controlled and fully automated (magnetic field 2.2 T) with stages for
    a. low temperature measurements (2 – 350 K)
    b. space-time resolved measurements for spin wave intensity mapping (resolution 50 µm, 0.83 ns)

   c. micro-focus measurements (focus diameter 0.3 µm)
   d. *in-situ* measurements
   e. elastic measurements

7. microwave setup (up to 32 GHz) comprising a network analyzer, microwave amplifiers, modulators, pulse generators, etc.
8. magnetotransport setups (magnetic field 1.5 T, temperature range 20 – 400 K)

### C) Equipment at the Institute for Thin Film Technologies (IDST), Rheinbreitach

1. Preparation of thin films:
   a. chemical vapor deposition (CVD) facility
   b. physical vapor deposition (PVD) facility
   c. plasma enhanced CVD (PECVD) facilities with an inductively coupled rf-plasma beam source and several magnetrons of different sizes
2. Surface and thin film analysis:
   a. profilometer: measurement of coating thickness and roughness determination of intrinsic stress and Young modulus
   b. Ball on Disk: measurement of friction coefficient analysis of surface friction
   c. Revetest: determination of adhesive strength analysis of microcracks
   d. microindention: determination of plastic and elastic microhardness (Vickers)
   e. optical contact angle measurement: determination of solid surface free energy and surface tension evaluation of hydrophobicity and hydrophilicity
   f. reflection- and transmission-spectroscopy (UV-VIS): optical measurements with wavelength range from 185 nm to 915 nm (resolution 1 nm), determination of absorption coefficient and optical gap (Tauc)
   g. (environmental) scanning electron microscopy (ESEM)[1]: comprehensive structural microanalysis of conducting, isolating, anorganic, organic and wet samples
   h. energy dispersive X-ray microanalysis (EDX)[1]: non-destructive fast analysis of elements
   i. neutron activation analysis (NAA)[2]: qualitative und quantitative analysis of main and trace components
   j. elastic recoil detection analysis (ERDA)[2]: analysis of trace elements with depth resolution analysis of hydrogen content
   k. Rutherford Backscattering (RBS)[2]: analysis of trace elements with depth resolution
   l. synchrotron-X-ray-fluorescence (SYXRF)[2]: non-destructive analysis of elements

---

[1] in cooperation with NTTF GmbH, Rheinbreitbach

[2] accelarator enhanced analysis in cooperation with the accelarator laboratories of the Universities of Munich, Bonn and Cologne

# Chapter 5: Transfer of Technology

## 1. Magnetism

With our facilities within the Department of Physics at the University of Kaiserslautern we offer consultance and transfer of technology in the areas of thin film magnetism, magnetic film structures and devices, magnetic sensors, and in corresponding problems of metrology.

We are equipped to perform magnetic, transport, elastic and structural measurements of films and multilayer systems.

This is in detail:

- magnetometry using vibrating sample magnetometry, Kerr magnetometry, Brillouin light scattering spectroscopy
- magnetic anisotropies, optionally with high spatial resolution
- magneto-transport properties
- test of homogeneity of magnetic parameters
- exchange stiffness constants in magnetic films
- elastic constants
- surface topography

## 2. Institut für Dünnschichttechnologie (IDST) - Transferstelle der Technischen Universität Kaiserslautern, Rheinbreitbach

## (Institute for Thin Film Technology - Center for Technology Transfer of the University of Kaiserslautern, Rheinbreitbach)

As part of technology transfer the Institute of Thin Film Technology (IDST) offers among other activities

- consultance in tribological problems
- development of product specific coatings
- optimization of coatings especially for medical applications
- coating of polymers and temperature sensitive materials
- coating of samples and small scale production series
- management for R&D-projects

The institute is located in Rheinbreitbach about 20 km south of Bonn in the Center for Surface Technologies (TZO) to support the economy in the northern part of the Rheinland-Pfalz State.

**Address:**

Institut für Dünnschichttechnologie
Maarweg 30-32
53619 Rheinbreitbach, Germany

**Scientific director:**

| | | |
|---|---|---|
| Prof. Dr. B. Hillebrands | phone: | +49 631 205 4228 |
| | e-mail: | hilleb@physik.uni-kl.de |

**Contact:**

| | | |
|---|---|---|
| Lisa Kleinen | phone: | +49 2224 900 693 |
| | fax: | +49 2224 900 694 |
| | e-mail: | kleinen@physik.uni-kl.de |

Please contact us for more information.

# Chapter 6: Experimental Results

## A. Linear and Nonlinear Spin Waves

### 6.1 Storage and parametrically stimulated recovery of microwave signal using standing spin-wave modes of a magnetic film

*A.A. Serga, A.V. Chumak, and B. Hillebrands*[1]

The problem of microwave information storage and processing using elementary excitations of matter has been intensively studied both theoretically and experimentally. For a long time the search concentrated on different types of echo-based phenomena involving phase conjugation techniques [1]. Several years ago, a new method of signal restoration was proposed and tested in experiments with dipolar spin waves scattered on random impurities and defects of ferrimagnetic media [2]. In this case the frequency-selective parametric amplification of a narrow band of scattered waves with frequencies close to the signal was used. As a result the uniform distribution of the secondary waves in phase space was distorted and a macroscopic noise signal was registered [3]. The noise characteristics of the restored signal are caused by the partial coherence as the signal is formed by many waves, having close but arbitrary shifted phases.

In one of the previous reports [4] we demonstrated the experimental results on the recovery of a microwave signal from the single mode of the discrete spin-wave spectrum, existing due to the spatial confinement of the magnon gas. The storage took place in a magnetically ordered solid, i.e., in a film of ferrimagnetic yttrium-iron-garnet. The trapping and storage of a microwave signal in a magnetic film was achieved through the conversion of the microwave frequency photons, first into propagating dipolar spin waves and then, through reversible transformation, into long-lifetime exchange-dominated standing spin waves that exist in the magnetic film due to its finite thickness. As the restored signal was formed by a single wave mode it had practically a noiseless character. The nature of such a signal restoration is based on complicated collective processes in the magnon gas. Here we give the qualitative explanation of the restoration process and show additional experimental results.

The experimental setup is shown in Fig. 1. The input electromagnetic microwave pulse is converted by the input microstrip transducer into dipolar spin waves that propagate in a long, narrow, 5 µm thick yttrium iron garnet (YIG) film. The other transducer, used to receive the output microwave signals, is situated at a distance of $l = 8\,\mathrm{mm}$ away from the input one. A bias magnetic field of $H_0 = 1706\,\mathrm{Oe}$ is applied in the plane of the YIG film, along its width and perpendicular to the direction of spin wave propagation. Input rectangular electromagnetic pulses with a duration of 100 ns, a carrier frequency of $f_{\mathrm{in}} = 7.039\,\mathrm{GHz}$, and varying power of $0.1\,\mu\mathrm{W} < P_{\mathrm{in}} < 6\,\mathrm{mW}$ are supplied to the input transducer and excite wave packets of magnetostatic surface waves (MSSW). The spin wave packet received by the output transducer is again converted into an electromagnetic pulse. After amplification and detection the output signal is observed with an oscilloscope. In the middle section of the YIG film (see Fig. 1) an open dielectric resonator producing a microwave magnetic field $\mathbf{h}_{\mathrm{p}}$ that is parallel to the static bias magnetic field $\mathbf{H}_0$ is placed. This resonator

---

[1] In collaboration with Prof. A.G. Melkov, Taras Shevchenko National University of Kiev, Kiev, Ukraine.

creates pumping pulses that can interact with the spin waves and oscillations existing in the YIG film. The resonance frequency of the pumping dielectric resonator ($f_r = 14.077\,\text{GHz}$) was chosen to be close to twice the input microwave pulse carrier frequency. Thus, the conditions of so-called parallel parametric pumping [6] were fulfilled.

The experiment starts at the initial moment of time $t = 0$ when a microwave pulse is applied to the input transducer. The excited MSSW packet propagates to the output transducer and excites the output microwave signal with the same duration and delay $t_{\text{prop}} \approx 350\,\text{ns}$, which is determined by the group velocity. During its propagations, the MSSW packet interacts with standing dipole-exchange modes [5] and leaves a “trail” of exited standing waves with much smaller group velocities. These spin waves are excited in the frequency regions near the dipolar gaps in the dipole-exchange spectrum of the film (see Fig. 2). Then, at time $t > t_{\text{prop}}$, a relatively long and powerful pumping pulse with a carrier frequency close to twice the central frequency of one of the dipolar gaps in the spectrum Fig. 2 is switched on. At this time the amplitude of the “gap” (non-propagating) spin wave modes, that naturally decreases with time due to the dissipation, has not yet decreased to the thermal level. The amplitude now starts to increase due to the parametric amplification by pumping. The increase of the amplitude of the “gap” spin waves is eventually limited by such nonlinear processes as direct excitation by pumping of exchange-dominated spin waves from the thermal level [7]. During the time the pumping is switched on the reversal interactions of the standing modes with the propagating MSSW take place. Thus, the amplified “gap” spin waves generate propagating MSSW modes which reach the output antenna and excite the second restored microwave signal [4].

To understand the mechanism governing the observed storage-and-recovery effect let us consider the dipole-exchange spectrum in MSSW geometry with in-plane carrier wave number $k_x$ in a film of thickness $L$. A calculated spectrum is shown in Fig. 2b. It consists of a Damon-Eshbach-type spin wave with a finite slope (non-zero group velocity) crossing several dispersion-less standing spin-wave modes indicated in Fig. 2b by the corresponding mode index $n$. These modes travel perpendicular to the film and, assuming the simple case of unpinned surface spins, the wavevector can be written as $k_\perp = \pi n/L$, where $n = 1, 2, 3 \ldots$. In the crossing regimes a small mode repulsion is obtained, and so-called “dipole-exchange gaps” in the spin-wave spectrum are formed [5]. Under the experimental conditions used the frequency separation between the discrete spin-wave modes of the film is $10-20\,\text{MHz}$, depending on the mode number $n$.

Since the frequency spectrum of a short (duration 100 ns) propagating spin-wave packet is several times wider than the frequency separation between two neighboring discrete standing spin-wave

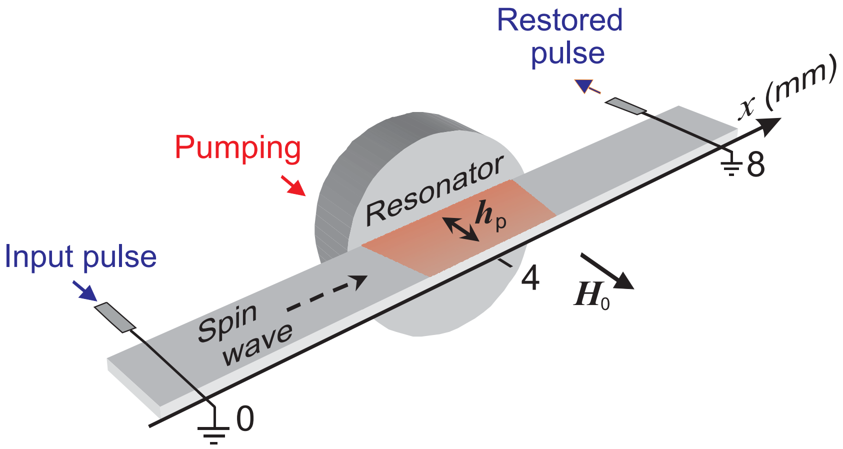

Fig. 1: Experimental setup.

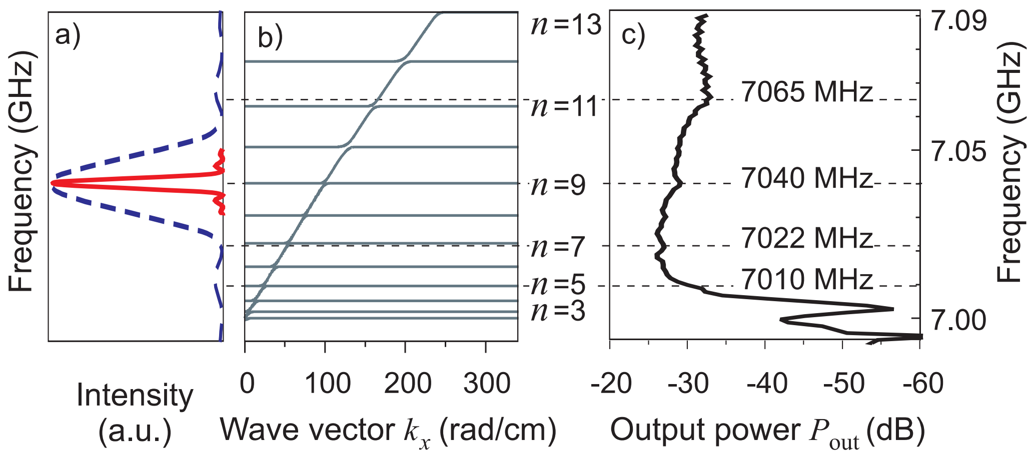

Fig. 2: a) Frequency spectra of the input pulse (dotted line) and pumping pulse (transferred to the half of the carrier pumping frequency) (solid line); b) Calculated dipole-exchange spectrum of travelling spin waves in the experimental YIG film ($n$ is the index number of a corresponding thickness mode); c) Transmission-loss characteristics of the experimental section. The horizontal dashed lines mark the frequencies at which the recovered microwave pulse was observed when the double-frequency pumping was applied.

modes, this packet can excite standing modes during its course of propagation. Due to their nearly zero group velocity these modes do not propagate away from the point where they are excited. Instead they form a “trail” of the MSSW pulse which exists for several microseconds. In contrast, a long pumping pulse (duration of a few microseconds), which has a relatively narrow frequency spectrum, will amplify only one of the excited standing modes. The parametrically amplified standing mode re-emits a travelling MSSW packet in exactly the same manner, as this mode was previously excited by the signal MSSW. Thus, the process of generation of the recovered pulse can be understood as a restoration of the initial signal that was dynamically stored in the magnetic film in the form of a discrete standing spin wave.

It is necessary to note, that although the parametrically recovered pulse is directly related to the input spin-wave packet and never appears without previous application of the input signal, its characteristics, such as peak power, duration, and delay time, are mainly determined by the process of parametric interaction with pumping. This fact is illustrated by Fig. 3, where the profiles of the restored pulses are presented for different values of the pumping power. Experimental dependencies of the peak power $P_r$, recovery time $t_r$, and duration $\Delta t_r$ of the restored pulse on the pumping power $P_p$ are shown in Fig. 4 by the symbols. It is evident that an increase of the pumping power $P_p$ leads to a decrease of $t_r$ and $\Delta t_r$, and to an increase of $P_r$.

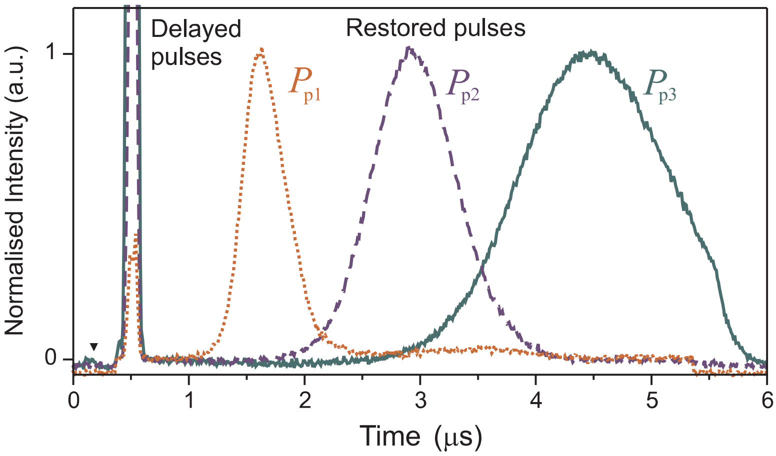

Fig. 3: Waveforms of the delayed and recovered pulses for different values of the pumping power $P_p$: $P_{p1} = 1.28\,\mathrm{W}$, $P_{p2} = 0.52\,\mathrm{W}$, $P_{p3} = 0.34\,\mathrm{W}$. Waveforms are normalized by the maximum intensity of each of the recovered pulses. The carrier frequency and power of the input pulse are 7040 MHz and $P_{in} = 10\,\mu\mathrm{W}$ (see Fig. 2). The low pedestal under the delayed and recovered pulses corresponds to the pumping pulse.

In order to understand the experimental dependencies of the temporal and amplitude characteristics of the recovered microwave pulse on the pumping power, we use the general theory of parametric interaction of spin waves (so-called “S-theory”) [8]. According to this theory, two concurrent processes may take place simultaneously: i) amplification of the signal spin wave, and ii) amplification of spin-wave modes from the thermal floor. Pumping with a sufficiently large amplitude $h_{\mathrm{p}} > h_{\mathrm{th}} = \Gamma_k / V_k$ (where $\Gamma_k$ is the relaxation frequency of a spin wave with wave number $k$, and $V_k$ is the coefficient of parametric coupling between this wave and the pumping field $h_{\mathrm{p}}$) will parametrically generate spin waves from the thermal floor whose amplitudes will increase with time $t$ as $\exp(h_{\mathrm{p}} V_k - \Gamma_k)\,t$ (see e.g. [6]). Moreover, it follows from [8], that even in the case of the pumping amplitude exceeding the threshold of parametric generation for several different spin-wave groups of spin-wave modes, only modes in one of these groups, having the maximum gain factor of parametric amplification $h_{\mathrm{p}} V_k - \Gamma_k$, will be excited. In our experimental geometry this dominating group is formed by short exchange-dominated spin waves having wave numbers $k \simeq 10^5\,\mathrm{rad/cm}$ and propagating in the film plane perpendicularly to the direction of magnetization of the sample. All other spin waves experience the combined and competing influence of the external pumping field and of an additional internal pumping field created by the above mentioned dominating spin-wave group. The internal (“spin-wave”) pumping process almost compensates the influence of the external pumping on the other spin waves in the sample, and their amplitudes remain close to the thermal level. As a result, no amplification of standing spin waves in dipole-exchange gaps is obtained if no input signal is applied.

In contrast, when an input signal is applied, it leaves behind a trail of linearly excited standing spin-wave modes existing near the dipole-exchange gaps in the spectrum of the film (see Fig. 2) and having amplitudes $A_{\mathrm{s}0}$ significantly exceeding the thermal level. Thus, when the pumping signal is applied, it starts to amplify both the high-amplitude standing spin waves in the spectral gaps and the short-wavelength exchange spin waves from the dominating group, whose amplitudes arise from the thermal level $A_{\mathrm{T}} \ll A_{\mathrm{s}0}$. It is obvious that the amplitude of the recovered microwave pulse, formed from the amplified standing waves, will reach the maximum value $A_{\mathrm{s\,max}}$ at the time $t_{\mathrm{max}}$ when the amplitude of the dominating spin-wave group reaches a certain critical value $A_{k\,\mathrm{cr}}$ which is sufficient to stop the parametric amplification of the standing modes:

$$t_{\mathrm{max}} = \frac{1}{h_{\mathrm{p}} V_k - \Gamma_k} \ln\left(\frac{A_{k\,\mathrm{cr}}}{A_{\mathrm{T}}}\right) \quad . \tag{1}$$

Thus, in the stationary regime, $t > t_{\mathrm{max}}$, standing spin waves will be suppressed, and the maximum amplitude of these waves at $t = t_{\mathrm{max}}$ can be written as

$$A_{\mathrm{s\,max}} = A_{\mathrm{s}0} e^{(h_{\mathrm{p}} V_{\mathrm{s}} - \Gamma_{\mathrm{s}}) t_{\mathrm{max}}} = A_{\mathrm{s}0} \left(\frac{A_{k\,\mathrm{cr}}}{A_{\mathrm{T}}}\right)^{\frac{h_{\mathrm{p}} V_{\mathrm{s}} - \Gamma_{\mathrm{s}}}{h_{\mathrm{p}} V_k - \Gamma_k}} \quad , \tag{2}$$

where $\Gamma_{\mathrm{s}}$ and $V_{\mathrm{s}}$ are the relaxation frequency of the standing modes and their coefficient of parametric coupling with pumping, respectively. The solid lines in Fig. 4 were calculated using Eqs. (1) and (2) assuming that $P_{\mathrm{r}} = A^2_{\mathrm{s\,max}}$. In this calculation we assumed that $\ln(A_{k\,\mathrm{cr}}/A_{\mathrm{T}}) = 10.25$, and that the widths of the resonant curves of dominating spin-wave group and the standing modes were $\Delta H_k = 2\Gamma_k/\gamma = 0.42\,\mathrm{Oe}$ and $\Delta H_{\mathrm{s}} = 2\Gamma_{\mathrm{s}}/\gamma = 0.485\,\mathrm{Oe}$, respectively, using a gyromagnetic ratio of $\gamma = 2.8\,\mathrm{MHz/Oe}$. Also we assumed that coupling the coefficient $V_k = V_{\mathrm{s}}$ is the same for the both waves groups. The pumping power was taken considering that $h_{\mathrm{p}} V_{\mathrm{s}} = \sqrt{P_{\mathrm{p}}}/K_{\mathrm{p}}$, where $K_{\mathrm{p}} = 9.4 \cdot 10^{-8}\,\mathrm{W}^{1/2}\mathrm{s}$.

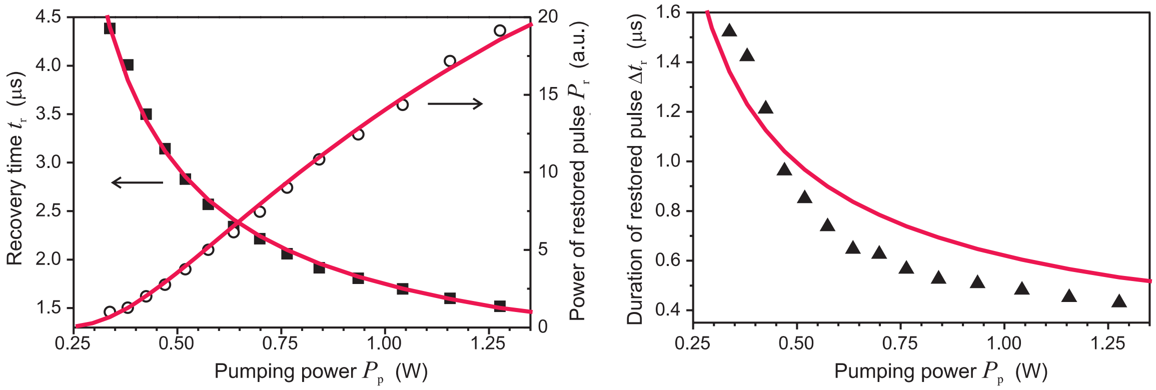

Fig. 4: Delay time (squares), peak power (open circles), and duration (triangles) of the restored pulse as functions of the pumping power. Solid lines: results of calculation using Eqs. (1), (2), and (3), respectively.

The proposed theoretical model can be easily presented in the form of the diagram in Fig. 5. The $x$-axis shows the time, $t = 0$ ns corresponds to the application of the input pulse. At time $t = 280$ ns the pumping signal is switched on. The $y$-axis shows the powers ($P \sim A^2$) of dominating group waves (dashed line) and standing "signal" waves (solid line) in logarithmic scale. The figure presents the evolution of the signal powers for different values of the pumping power $P_\mathrm{p}$: $P_\mathrm{p1} = 1.28$ W, $P_\mathrm{p2} = 0.52$ W, $P_\mathrm{p3} = 0.34$ W. It is clear from the picture that standing waves are excited some time after application the input signal (open circle) and its power decreases with time and with the speed determined by the relaxation factor $\Delta H_\mathrm{S}$. When using parametric pumping the amplitudes of these waves start to increase with different speeds determined by the pumping power. When the pumping is switched on, the dominating group starts to increase too. The initial amplitude of this group is determined by the thermal level $A_\mathrm{T}$ and is smaller than initial "signal" wave amplitude ($ln(A_\mathrm{s0}/A_\mathrm{T}) = 0.35$). At different times (for different pumping powers) the powers of dominating group waves reach the critical value $P_\mathrm{max}$; the corresponding times (vertical dashed lines) determine the maxima of the restored signals. In Fig. 5 the dotted line shows the calculated dependence of the power of the restored pulse on the time, the squares shows the corresponding experimental data.

The duration of the recovered pulse (see Fig. 4) can be theoretically estimated by taking into account the frequency selective character of the parametric amplification process. Due to this selectivity the frequency bandwidth of the parametrically amplified spin waves (and, therefore, the duration of the restored pulse formed by these spin waves) is determined by the intensity and duration of the pumping pulse. In the approximation of strong pumping the restored pulse has a Gaussian profile with a duration $\Delta T_\mathrm{r}$ at half the maximum level [7]:

$$\Delta T_\mathrm{r} = 2\sqrt{\frac{t_\mathrm{max}\ln 2}{h_\mathrm{p}V_k}} = 2\sqrt{\frac{\ln(A_{k\,\mathrm{cr}}/A_\mathrm{T})\ln 2}{(h_\mathrm{p}V_k - \Gamma_k)h_\mathrm{p}V_k}} \quad . \tag{3}$$

We assume here that the duration of the parametric amplification process for the standing modes is limited by the influence of the dominating group of exchange spin-waves, and, therefore, the effective pumping duration can be estimated as $t_\mathrm{max}$. From Fig. 4 one can see that Eq. (3) gives a good description of the experimental data. We believe that an even better description of the experimental results could be achieved if experimental parameters such as the finite duration of the input signal, realistic widths of the dipole-exchange gaps, and nonlinear properties of the standing spin-wave modes were accounted for in the theory.

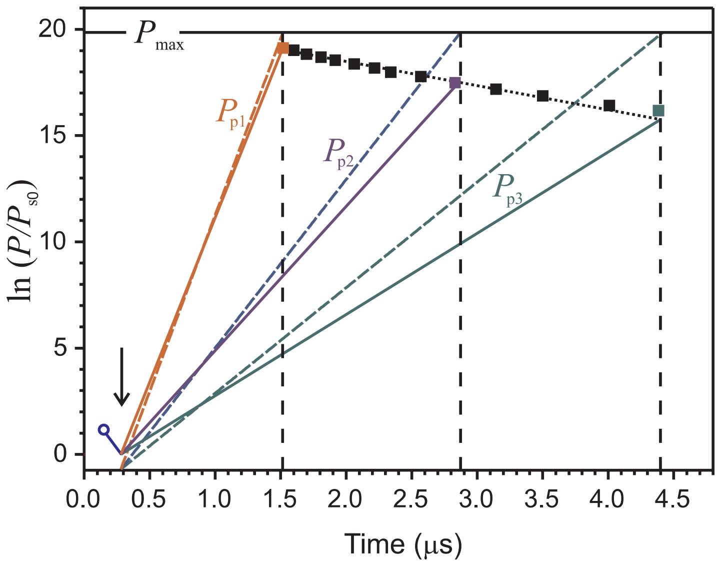

Fig. 5: Temporal development of parametric amplification of a dipole-exchange standing spin wave (solid oblique lines) as well as a thermal spin wave (dashed oblique lines) calculated for different pumping powers $P_p$: $P_{p1} = 1.28\,W$, $P_{p2} = 0.52\,W$, $P_{p3} = 0.34\,W$. Zero time corresponds to the time of application of the input pulse. The open circle marks the moment of excitation of the standing spin wave mode by the packet of traveling MSSW packets. The vertical arrow indicates the time when pumping is switched on. The vertical dashed lines mark the times when the intensity of the parametrically amplified thermal wave reaches the critical value $P_{max}$ (horizontal solid line) and freezes the amplification of standing spin wave. The solid squares show the measured intensity of the restored pulse as a function of the recovery time, and the dotted line indicates the results of calculations.

In conclusion, we observed the effect of coherent storage and recovery of a microwave signal in a ferrite film. The signal is stored in the film in the form of standing spin waves excited by the input microwave pulse in the frequency intervals near the dipole-exchange gaps i.e., near the points of hybridization between the lowest (dipole-dominated) spin-wave mode of the film and the higher-order (exchange-dominated) spin-wave modes. The signal is recovered by a long and powerful pumping pulse with a carrier frequency close to twice the central frequency of one of the spectral gaps. The proposed simple quasi-linear theory of parametric amplification by non-stationary (pulsed) pumping provides a good qualitative explanation of the experimental results presented in Figs. 3 and 4. These results might pave the way to new approaches of signal processing using combined microwave/spin-wave devices.

This work was partially supported by the Deutsche Forschungsgemeinschaft (SFB/TRR 49 and DE 639/6), by the Ukrainian Fund for Fundamental Research (25.2/009), by the MURI grant W911NF-04-1-0247 from the U.S. Army Research Office, and by the Oakland University Foundation.

## References

[1] A. Korpel and M. Chatterjee, Proc. IEEE **69**, 1539 (1981).
[2] G.A. Melkov, Yu.V. Kobljanskyj, A.A. Serga, A.N. Slavin, V.S. Tiberkevich, Phys. Rev. Lett. **86**, 4918 (2001).
[3] Yu.V. Kobljanskyj, V.S. Tiberkevich, A.V. Chumak, V.I. Vasyuchka, G.A. Melkov, A.N. Slavin, J. Magn. Magn. Mater. **272**, 991 (2004).
[4] A.A Serga, A. André, S.O. Demokritov, B. Hillebrands, AG Magnetismus Annual Report, 38 (2004).
[5] B.A. Kalinikos, A.N. Slavin, J. Phys. C **19**,7013 (1986).
[6] A.G. Gurevich and G.A. Melkov, *Magnetization oscillations and waves* (CRC Press, New York, 1996).
[7] G.A. Melkov, A.A. Serga, V.S. Tiberkevich, A.N. Oliynyk, A.V. Bagada, and A.N. Slavin, J. Exp. Theor. Phys. (JETP) **89**, 1189 (1999).
[8] V.S. L'vov, *Wave Turbulence under Parametric Excitations. Applications to Magnetics.* (Springer-Verlag, 1994).

## 6.2 Non-resonant parametric restoration of microwave spin-wave signals in YIG film

*S. Schäfer, A.V. Chumak, A.A. Serga, and B. Hillebrands*

During our recent studies of parametric interaction of electromagnetic radiation with the discrete spectrum of a magnon gas we found the possibility of long-time storage and parametrically stimulated recovery of microwave signals using standing spin-wave modes of a thin magnetic film (see Section 6.1 within this Annual Report). For these experiments, parametrical interaction was performed by applying a microwave pumping signal with a frequency $\omega_\mathrm{p} = 2 \cdot \omega_\mathrm{s}$ which is twice the carrier frequency $\omega_\mathrm{s}$ of the input microwave signal. This ratio between the frequencies corresponds to the pure case of parametric resonance of the first order. Here we report on the non-resonant case of parametric restoration with $\omega_\mathrm{p} \neq 2 \cdot \omega_\mathrm{s}$. This technique enables access to the spectral characteristics of the processes that underly both the storage and the restoration phenomena. Therefore these studies are relevant for the basic understanding of interactions between different groups of magnons as well as for technical applications, using the ability to store, retrieve and process spectral information of microwave signals.

The experimental setup includes a long and narrow ($30 \times 1\,\mathrm{mm}^2$) spin-wave waveguide cut out of a thin ($5.94\,\mu\mathrm{m}$) single crystal yttrium iron garnet (YIG) film which is placed upon both input and output microstripe antennae. The signal microwave pulse excites a packet of spin waves which propagates along the waveguide from the input to the output antenna. The signal picked up by the output antenna is observed with an oscilloscope after amplification and detection. The long axis of the YIG film waveguide and therefore the propagation direction of the spin wave is perpendicular to the static magnetic field of $H_0 = 1780.5\,\mathrm{Oe}$ applied in the film plane. Thus the experimental geometry generally corresponds to the case of dipolar-dominated magnetostatic surface spin waves (MSSW) [1]. However, due to the finite thickness of the magnetic medium, discrete exchange-dominated standing spin-wave modes perpendicular to the film's surface exist [3]. That leads to a modified dispersion spectrum as can be seen in Fig. 2 in Section 6.1. In the regions where perpendicular standing spin-wave modes (PSSW) and the MSSW dispersion are crossing, a hybridization occurs. This hybridization is a manifestation of an interaction between those magnon groups and allows for an exchange of magnons and energy, respectively, from one magnon group to another. Thus, an excitation of PSSW modes by a bypassing MSSW packet occurs. Due to the almost negligible group velocity of PSSW modes, energy and information contained within the traveling wave are conserved in the localized film area and therefore can be retrieved by means of parametric amplification of the PSSW significantly after the traveling spin-wave pulse left the film. For deeper insight into the process of storage and restoration, please refer to Section 6.1.

In order to amplify the PSSW modes we used the method of parallel pumping [2]. The pumping magnetic field, which is parallel to the bias magnetic field, is created by the dielectric resonator attached to the waveguide in the middle between the antennae (see Fig. 1 in Section 6.1). The resonator is excited by a microwave pulse at a fixed carrier frequency of $\nu_\mathrm{p} = 14.258\,\mathrm{GHz}$. This frequency was chosen to coincide with twice the frequency of one PSSW mode in order to obtain the maximal efficiency of its parametric amplification. The pumping pulse is only applied after the traveling spin-wave packet is detected at the output antenna and therefore left the area of parametric interaction. In the experiments reported, the pumping pulse with a power of $4\,\mathrm{W}$ had a duration of $7\,\mu\mathrm{s}$ and was delayed by $400\,\mathrm{ns}$ with respect to the signal pulse.

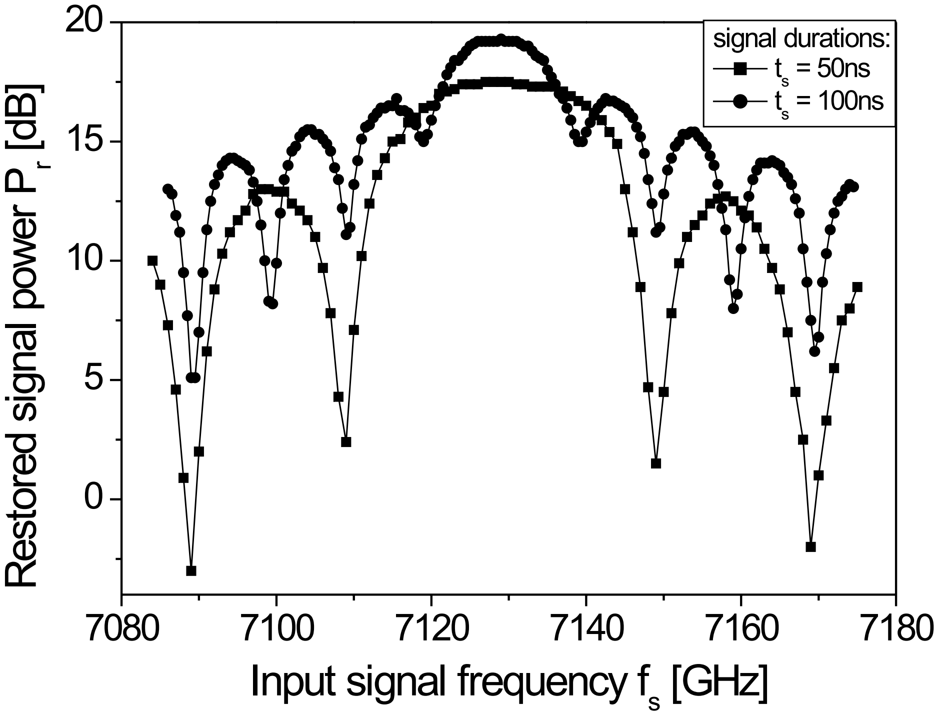

Fig. 1: Experimental results. Power of the restored pulse is depicted against the carrier frequency $\nu_{\mathrm{signal}}$ of the input signal pulse. The dots represent the further discussed measurement with signal pulse length of $\tau_s = 100\,\mathrm{ns}$. In comparison, the squares show the results for a pulse duration of $\tau_s = 50\,\mathrm{ns}$, revealing a broader spectral distribution as is expected from Eq. (1).

In Fig. 1 our experimental results for the input microwave pulses of duration $\tau_s = 50\,\mathrm{ns}$ and $\tau_s = 100\,\mathrm{ns}$ are presented. The results were obtained by keeping the output voltage from the microwave detector constant while varying the attenuation of the signal before it enters the low noise microwave amplifier and semiconductor detector. This was done in order to operate all relevant microwave components and the detector in a linear regime of operation and exclude all possible nonlinear influences of the experimental setup. One can see the dependence of the restored pulse intensity on the carrier frequency of the input signal pulse. The global maximum at $\nu_{s,0} = 7.129\,\mathrm{GHz}$ corresponds to half the pumping frequency as expected for the pure resonant case. The positions of other maxima (as well as minima) are directly correlated with the Fourier spectra of the input signals. For example the doubling of the frequency width for a pulse with half the duration is clearly visible. This correlation clearly manifests the dependence of the intensity of the restored pulse on the intensity of the PSSW mode, which is linearly excited by the spectral components of the input signal in a narrow frequency band of 1 MHz width.

In order to understand the experimental results in detail we concentrate now on the data obtained with a pulse duration of $\tau_s = 100\,\mathrm{ns}$. In Fig. 2 the experimental values (circular dots) are presented together with the normalized Fourier spectrum (dashed line)

$$P_s \propto \left( \frac{\sin\left((\omega_s - \frac{\omega_p}{2}) \cdot \tau_s/2\right)}{(\omega_s - \frac{\omega_p}{2}) \cdot \tau_s/2} \right)^2 \tag{1}$$

corresponding to a linear dependency of the output pulse power on the signal pulse power, normalized with respect to the experimental values. In spite of similarities between these spectra one can

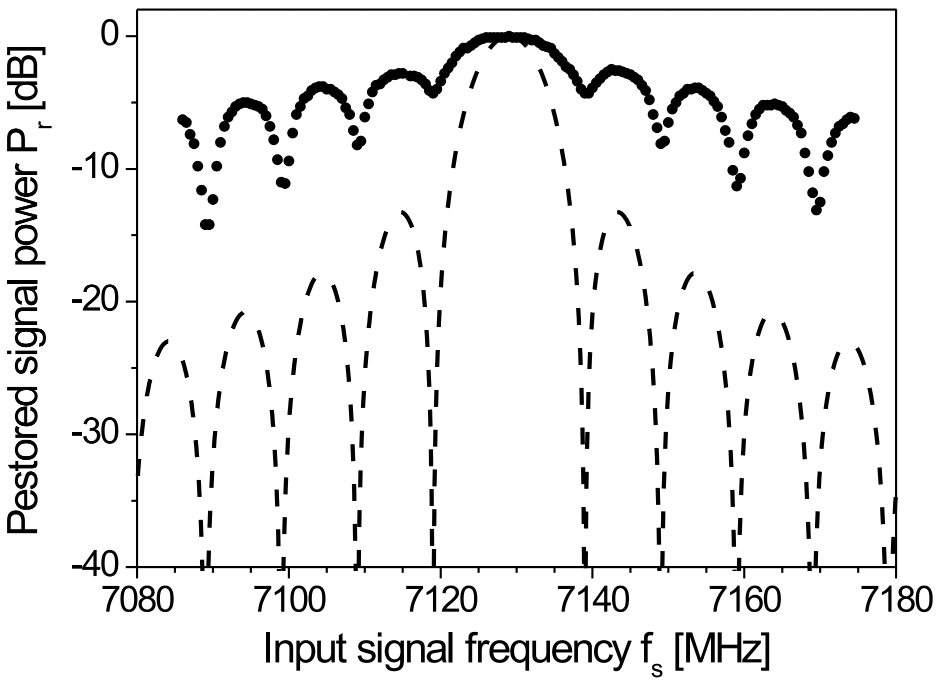

Fig. 2: Arrangement of experimental results for a pulse duration of $\tau_s = 100\,\text{ns}$ from Fig.e 1 (dots) and theoretical curve according to Eq. (1) (dashed line) for the input pulse signal power against the signal frequency.

see that the relative intensities of the spectral components of the restored pulse are significantly different from the frequency spectra of the input pulse. Thus no linear connection between the intensities of the restored and input signals exists.

We interpret this deviation using a simple model discussed in more detail in Section 6.1 and basing upon a general theory of parametric interaction of spin waves [4]. Assuming that the maximum amplitude of a parametrically amplified PSSW is limited by the influence of simultaneously amplified thermal spin waves one can describe the maximum amplitude of the PSSW by

$$A_{\mathrm{s,max}} = A_{\mathrm{s,0}} \cdot \left(\frac{A_{\mathrm{k,cr}}}{A_{\mathrm{T}}}\right)^{\delta} \quad , \tag{2}$$

where $A_{\mathrm{k,cr}}$ is a critical amplitude of the thermal magnons leading to increased damping and $\delta$ is a parameter defined by

$$\delta = \frac{V_{\mathrm{P}} - \Gamma_{\mathrm{S}}}{V_{\mathrm{P}} - \Gamma_{\mathrm{k}}} \quad . \tag{3}$$

The parameters $V_{\mathrm{P}}$, $\Gamma_{\mathrm{S}}$ and $\Gamma_{\mathrm{k}}$ denote the coefficient of parametric coupling with pumping and the relaxation frequencies for the signal frequency and the thermal magnons, respectively.

This relation describes a saturation behavior for amplified magnons due to the presence of thermal magnons. However, the signal pulse irradiated by the input antenna is capable of increasing the level of thermal spin waves due to two-magnon scattering processes. Therefore we can assume that the initial level of the thermal magnons is increased by the signal pulse according to

$$A_{\mathrm{T}} = A_{\mathrm{T,0}} + \beta \cdot A_{\mathrm{s,0}} \approx \beta \cdot A_{\mathrm{s,0}} \tag{4}$$

assuming $\beta \cdot A_{s,0} \gg A_{T,0}$. The coefficient β describes here the influence of the signal spin wave on the thermal magnon gas. Since $A_{s,0} = \sqrt{P_{s,0}}$, the power of the restored pulse can be depicted as

$$P_r = c \cdot P_{s,0}^{1-\delta} \quad , \tag{5}$$

with the constant $c = \left(\frac{A_{cr}}{\beta}\right)^{\delta}$. Shown in Fig. 3 are the experimental data extracted from Fig. 1 against values for the input signal power expected from Eq. (1) normalized with respect to the maximum power of the restored signal.

Given the slope of 0.23 in Fig. 3, the parameter δ in Eq. (1) is quantified as $\delta = 0.77$. A look at the continuous line in Fig. 2, representing the input power (dashed line) multiplied with $\alpha = 1 - \delta = 0.23$ reveals the excellent agreement between the experimental data and our model, which predicts the linear dependency between input and restored signal intensities on a logarithmic scale. The remarkable feature is the drastic increase in dynamic range of a device based upon the presented effects. The accessible range of microwave power detectable will be increased by the coefficient α using the logarithmic dB-scale. Considering the limits of the presented phenomenological model, it is important to point out that the assumption of linear excitation for the traveling signal spin-wave pulse was an essential premise.

In conclusion, the restoration of microwave signals with means of non resonant parametric pumping was observed, basing on the storage of spin-wave information in the hybridized spin-wave spectra of a thin YIG film. This is the first step of a deeper understanding of the process of

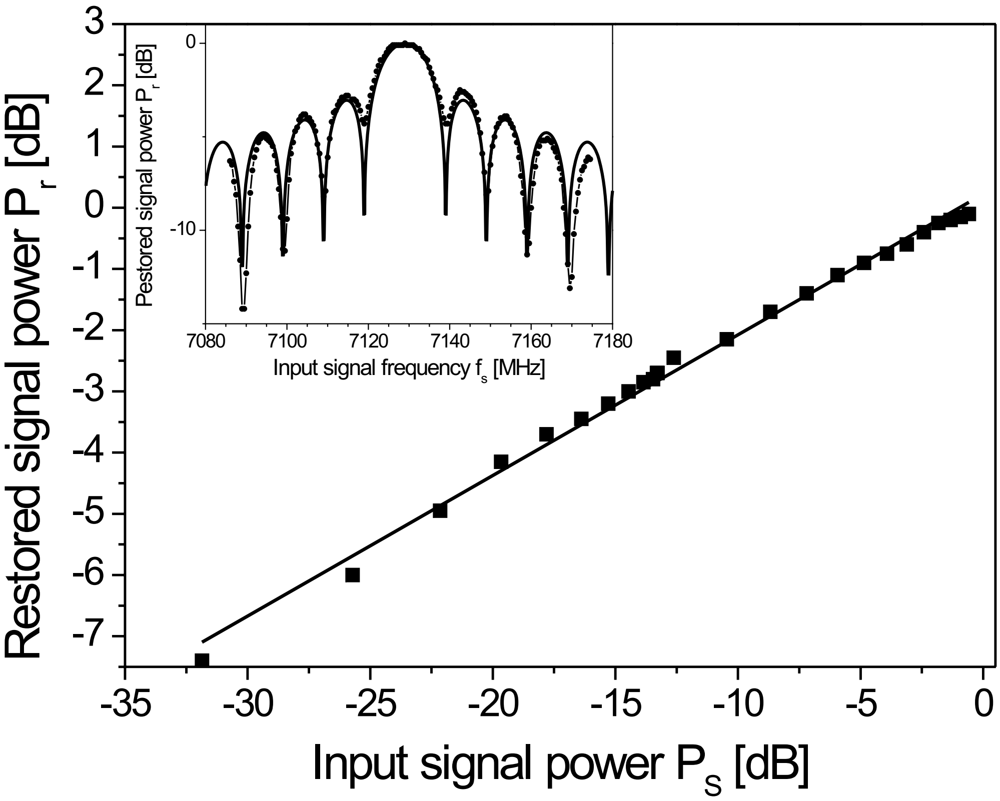

Fig. 3: Power of the restored pulse against the power of the input signal pulse. The data is taken fromFig.e 2 and a linear regression (continuous line) yields a value of $1 - \delta = 0.23$. This parameter describes the interaction between the input signal and the thermal magnons. If the input signal would have no influence on the thermal level of magnons, one could expect a slope equal to one. The inset shows the experimental data from Fig. 1 (dots) together with the continuous line corresponding to our model.

restoration of spin-wave pulses by parametric interaction and a simple phenomenological theoretical model was proposed describes the experimental results very well. Furthermore, we proposed the possibility of usage of the described process for a spectrum analyzer, taking advantage of the fact that the range of the output power is compressed by $P_\mathrm{r} = c \cdot P_{\mathrm{s},0}^{\alpha}$ and thus increasing the accessible dynamic range since this is usually limited by the restricted range of the analyzers' detecting component.

Financial Support by the DFG within the SFB/TRR 49 is gratefully acknowledged.

## References

[1] R.W. Damon, J.R. Eshbach, J. Appl. Phys. **31**, 104 (1960).
[2] A.G. Gurevich, G.A. Melkov, CRC Press, New York (1996).
[3] B.A. Kailinikos, A.N. Slavin, J. Phys. C **19**, 7013 (1986).
[4] V.S. L'vov, *Wave turbulence under parametric excitation*, in: *Applications to magnetics*, Springer, (1994).

## 6.3 Excitation phase of backward volume and surface magnetostatic waves

*T. Schneider, A.A. Serga, T.M. Neumann, B. Hillebrands*[1]

It is well known, that the amplitude symmetry of two spin-wave pulses with antiparallel wavevectors excited by the same microwave pulse depends on the used geometry. In the case of the so called Backward Volume Magnetostatic Spin Waves (BVMSW, magnetic bias field parallel to the propagation direction) the two spin waves propagate with an identical amplitude while for the Magnetostatic Surface Spin Waves (MSSW, magnetic bias field perpendicular to the propagation direction) the propagation in one direction is strongly suppressed [1]. Up to now no experimental data was available on the phase symmetry for these two cases. The recent development of the phase resolved Brillouin light scattering spectroscopy [2] now makes it possible to observe the change of phase with propagation distance (the so called phase accumulation [3]). This allows us to measure the phase difference between the two counterpropagating waves, which we will refer to as "excitation" phase. Here we present our measurements of this excitation phase as well as a theoretical model explaining the observed effect.

Figure 1a shows a picture of the used experimental setup. Spin waves were excited using a 50 µm wide microstrip antenna situated on a 5 µm thick yttrium iron garnet (YIG) spin-wave waveguide. Spin waves excited using a microwave pulse (pulse length 50 ns, carrier frequency 7.132 GHz) applied to the antenna can propagate freely in both directions, as demonstrated in Fig. 1b of the figure for BVMSSW geometry.

To investigate the excitation phase we performed a phase accumulation measurement. A typical example of the obtained results is shown in Fig. 2 (bias magnetic field 1835 Oe parallel to the propagation direction, carrier frequency 7.132 GHz). One can clearly see the linear behaviour of the phase on both sides of the antenna. As we have used a linear, quasi monochromatic spin wave this behaviour can be described as wavevector $k$ times the propagation distance $z$. Using a microscopic picture of the microstrip antenna and the substrate holder (shown in the inset of Fig. 2) one can identify the position of the antenna in respect to the measured data. The extrapolation of the linear fit of the phase accumulation up to the edges of the antenna allows us to then determine the excitation phase of the spin wave under investigation as $(1.1 \pm 0.4)\pi$ in the shown example. Other measurements performed for different bias magnetic fields (and thus different wavevectors) confirm a value of $\pi$ for the excitation phase of BVMSW within the error margins.

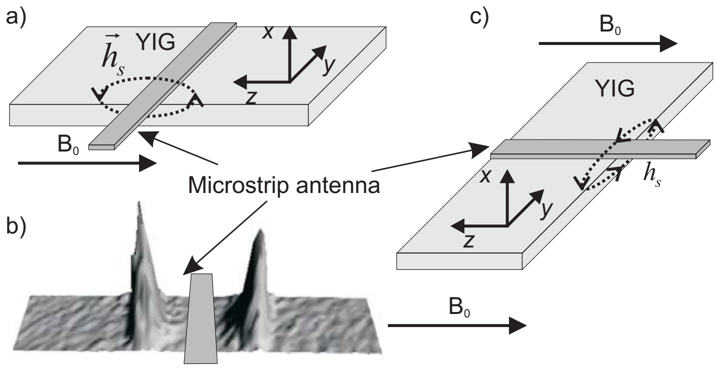

Fig. 1: a) Experimental setup for BVMSW geometry. Spin waves were excited using a microstrip antenna. b) Space resolved BLS measurement of two counterpropagating spin waves in the BVMSW geometry approximately 50 ns after there excitation. c) Experimental setup for MSSW geometry.

---

[1] In collaboration with M.P. Kostylev, School of Physics, University of Western Australia, Crawley, Australia.

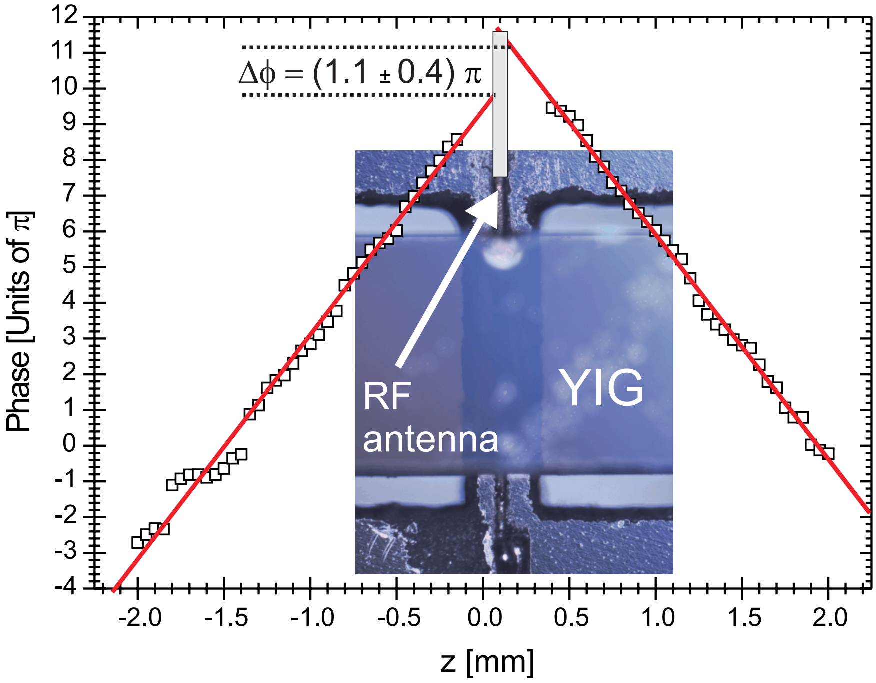

Fig. 2: Phase accumulation for BVMSW geometry. The excitation phase of $(1.1 \pm 0.4)\pi$. The applied bias magnetic field was 1835 Oe. Spin wave carrier frequency and absolute wavevector value was 7.132 GHz and $(198 \pm 1)\,\mathrm{cm}^{-1}$, respectively.

This result can be understood if one takes into account the exact geometry of the problem. Using the coordinate system defined in Fig. 1a the dynamic magnetization $\mathbf{m}$ lays in the $x$–$y$–plane, while the microwave field created by the antenna, $\mathbf{h}_\mathrm{s}$, as well as the dipolar field, $\mathbf{h}_\mathrm{d}$, only have components in $x$– and $z$–direction. The relation between the fields and the dynamic magnetization is given by the microwave susceptibility $\hat{\chi}$ as

$$\mathbf{m} = \hat{\chi} \cdot (\mathbf{h}_\mathrm{d} + \mathbf{h}_\mathrm{s}) \quad . \tag{1}$$

For the backward volume geometry there is no intermixing between the diagonal and off-diagonal components of $\hat{\chi}$. This results in the symmetrical excitation of the amplitudes of both spin waves. To understand the difference in phase one has to note that only the out-of-plane ($x$) component of $\mathbf{h}_\mathrm{s}$ can couple to $\mathbf{m}$. This component has an antisymmetric profile along the $z$–axis with a node in the middle of the antenna, which translates to an antisymmetric profile of the dynamic magnetization $\mathbf{m}$ and thus to an excitation phase of $\pi$ as confirmed in our measurements.

For the MSSW geometry the situation changes drastically. As demonstrated in Fig. 1c, both fields $\mathbf{h}_\mathrm{d}$ and $\mathbf{h}_\mathrm{s}$ as well as the dynamic magnetization $\mathbf{m}$ lay in the $x$–$y$–plane, the diagonal and off-diagonal components of $\hat{\chi}$ intermix in Eq. (1). This leads to the effect of the drastically assymmetrical amplitude for the two waves with antiparallel wavevectors and, in addition, and contrary to the BVMSW mode, to an identical phase.

Figure 3 shows a typical example of the measurements for MSSW geometry (bias magnetic field 1825 Oe perpendicular to the propagation direction, carrier frequency 7.132 GHz). As in the BVMSW case the phase accumulation on both sides is linear (but this time with a positive wavevector), but the excitation phase is determined as $(-0.1 \pm 0.2)\pi$. Additional measurements for different bias magnetic fields confirm an excitation phase of 0 within the error margins.

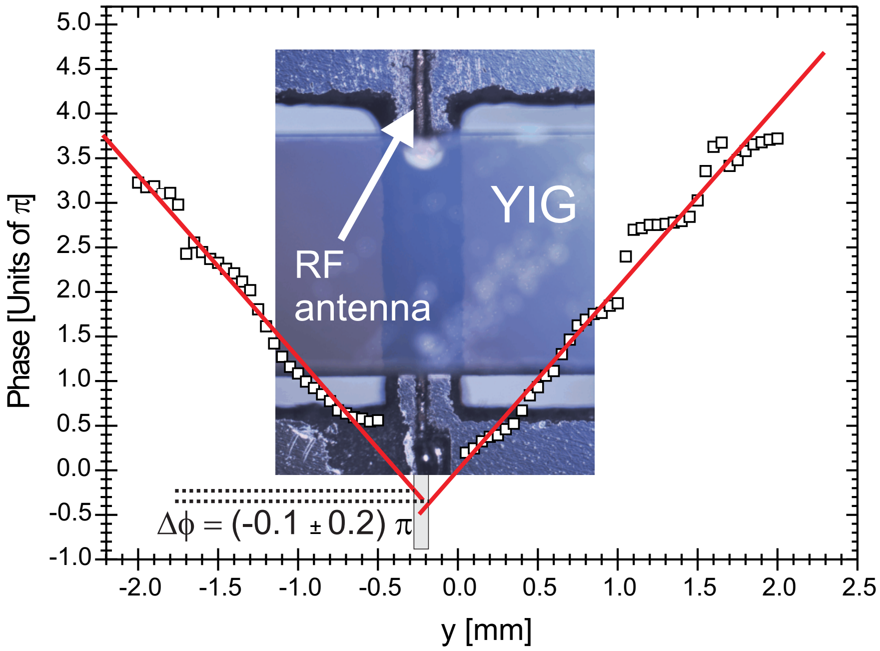

Fig. 3: Phase accumulation for MSSW geometry. The excitation phase is $(-0.1 \pm 0.2)\pi$. The applied bias magnetic field was 1835 Oe. Spin wave carrier frequency and absolute wavevector value was 7.132 GHz and $(64.21 \pm 0.04)\,\mathrm{cm}^{-1}$, respectively.

Figure 4 shows a summary of the performed experiments. The previously described behaviour is clearly visible for all wavevectors. The notable different excitation phase for the measurements with the lowest absolute value for the wavevector can be understood by taking into account that a spin-wave pulse propagating close to the ferromagnetic resonance frequency becomes strongly distorted. This distortion also influences the phase and thus the measured values for the excitation phase.

In conclusion we demonstrated that backward volume waves which are excited symmetrically in amplitude show an excitation phase of π while the surface waves which are unsymmetrical in amplitude have no such excitation phase.

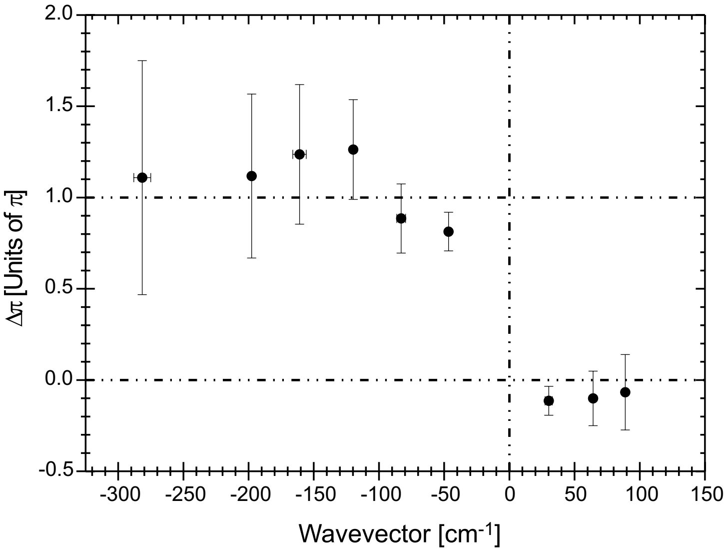

Fig. 4: Summary of the performed measurements. The expected behaviour is clearly visible. The different excitation phase values for the lowest absolute values of the wavevectors can be understood by the distortion due to the propagation close to the ferromagnetic resonance frequency.

Financial Support by the DFG within the Graduiertenkolleg 792 and the project SE 1771/1-1 and the Australian Research Council and technical support by the Nano + Bio Center, TU Kaiserslautern is acknowledged.

### References

[1] R.W. Damon, J.R. Eshbach, J. Phys. Chem. Solids **19**, 308 (1961).
[2] A.A. Serga, T. Schneider, B. Hillebrands, S.O. Demokritov, M.P. Kostylev, Appl. Phys. Lett. **89**, 063506 (2006).
[3] T. Schneider, A.A. Serga, B. Hillebrands, M.P. Kostylev, Europhys. Lett. **77**, 57002 (2007).

## 6.4 Resonant scattering of spin waves from a region of inhomogeneous magnetic field in a ferromagnetic film

*T.M. Neumann, A.A. Serga, T. Schneider, B. Leven, and B. Hillebrands*[1]

The term *magnonic crystal* generally describes magnetic structures exhibiting a periodic variation of their magnetic properties in either one, two or three dimensions [1]. Currently, magnonic crystals are studied intensively because of their possible applications in fundamental and applied physics. It has been shown that magnonic crystals can possess full band gaps where spin waves are not allowed to propagate. Therefore, they are widely considered as a prospective means for the effective localization and guidance of spin waves.

A possible realization for magnonic crystals, which can be dynamically controlled, consists of placing a set of wires on the surface of a magnetic material (see for instance [2]). By changing the current through these wires the local magnetic field - and by this the spin wave propagation - is influenced.

In order to understand how the localized magnetic inhomogeneity created by the Oerstedt field of a single such wire influences the spin wave propagation, we have studied, in detail, the transmission of dipole-dominated backward volume spin waves in a ferrite film with the help of microwave techniques.

Figure 1a shows a sketch of the experimental microwave setup. The output of a microwave generator is sent to a switch which transforms the cw-signal into a short microwave pulse. This pulse is amplified and sent to a 50 µm wide strip-line transducer placed on the surface of a 5 µm thick yttrium iron garnet (YIG) film on a gallium gadolinium garnet (GGG) substrate.

In the film the microwave signal excites dipole-dominated spin waves of backward volume type, whose *k*-vector is aligned in the direction of the applied bias magnetic field. For the used microwave frequencies and bias magnetic fields this *k*-vector is typically in the 100 $\mathrm{cm}^{-1}$ to 1000 $\mathrm{cm}^{-1}$ range. The spin waves propagate through the film and are picked up by a second identical antenna situated approximately 8 mm away. By amplifying and detecting the resulting microwave signal we can observe the pulse shape in real time on an oscilloscope.

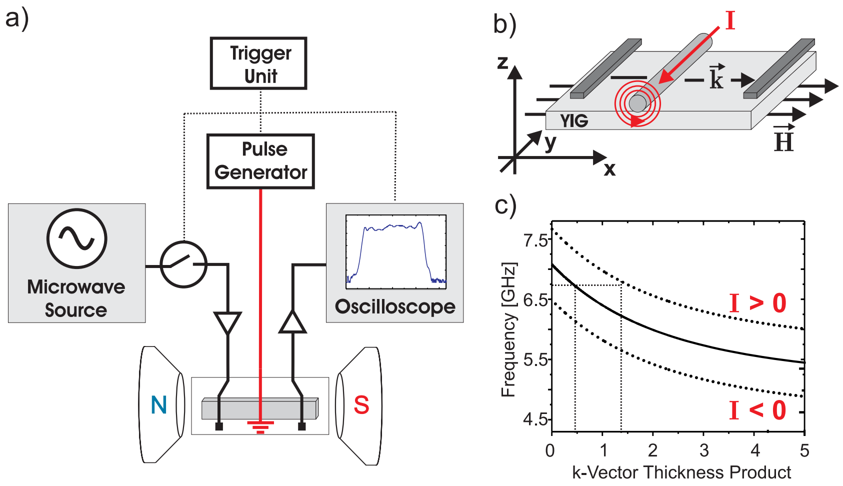

Fig. 1: Sketch of the experimental microwave setup a) and of the section layout b). The influence of the dc-current on the dispersion relation is shown in c).

---

[1] In collaboration with M. Kostylev and R.L. Stamps at the School of Physics, University of Western Australia, Crawley, Australia.

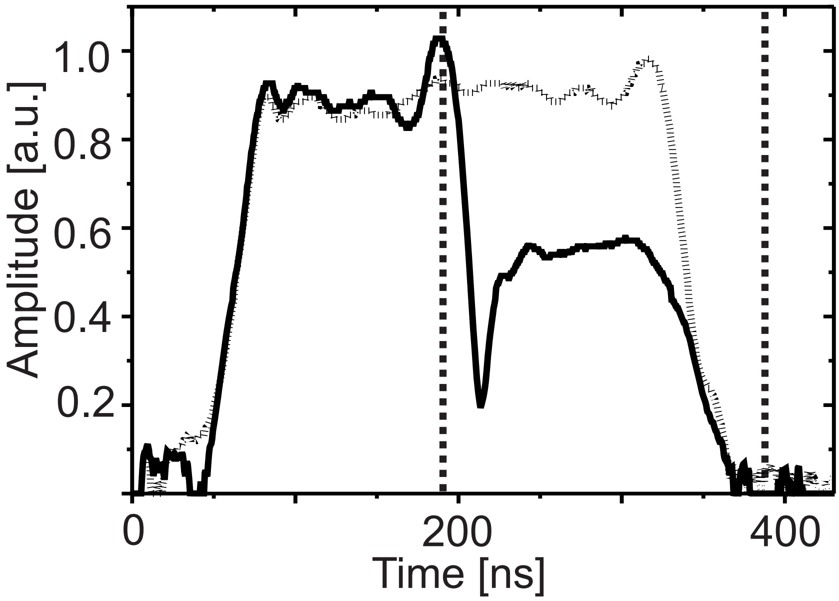

Fig. 2: Signal pulse as seen on the oscilloscope without applied dc-current (slashed) and with applied dc-current of $+0.5\,\mathrm{A}$ (bold) for a bias magnetic field of $H = 1800\,\mathrm{Oe}$ and a microwave frequency $\omega = 2\pi \cdot 7.16\,\mathrm{GHz}$. The vertical dashed lines indicate the dc-pulse duration.

Such an oscilloscope picture is shown as a dotted line in Fig. 2. For the experiment we chose a pulse length of 300 ns, which corresponds to the propagation time of the investigated spin waves in the film. With this pulse length, we can avoid interference between the electromagnetic signal transmitted directly from the input to the output antenna and the signal from the spin wave pulse.

A $50\,\mu\mathrm{m}$ thick wire placed on the film surface halfway between the input and output antenna is used to create a highly localized magnetic inhomogeneity. Figure 1b shows this schematically.

Depending on the direction of the dc-current applied to the wire, the Oerstedt field either locally increases the magnetic field (in our case for positive currents) or decreases it (negative currents). This in turn leads to a shift of the spin wave dispersion relation as it is depicted in Fig. 1c. We note that for any reasonable positive current there always exists a suitable $k$ for the predefined value of $\omega$ while this is not the case for negative currents. In other words, the magnetic inhomogeneity formed by a negative current creates - by locally decreasing the magnetic field - a *barrier* where the propagation of the investigated spin waves is prohibited. A positive current, on the contrary, creates a *well*.

In the experiments currents between $+2\,\mathrm{A}$ and $-2\,\mathrm{A}$ were available, which corresponds to a maximal change of the bias magnetic field of about $\pm 200\,\mathrm{Oe}$. In order not to overheat the sample, firstly, the dc-current was applied in short pulses of 200 ns. Secondly, a low overall repetition rate of 1 ms was chosen.

The dc-current pulse was delayed with respect to the microwave pulse so that it only disturbed the second half of the spin wave pulse (see bold line in Fig. 2). This ensured that there was no interference with parasitically excited spin waves created by the electromagnetic radiation from the input antenna in the current carrying wire. Additionally, the undisturbed front part of the pulse was used as a reference point: it allowed us to verify that the external conditions, such as magnetic field and temperature, remained constant during the experiment.

The results presented in the following were obtained for a bias magnetic field of $H = 1800\,\mathrm{Oe}$.

In the left panel of Fig. 3 the transmitted signal amplitude for different currents and fixed frequency $\omega = 2\pi \cdot 7.16\,\mathrm{GHz}$ is presented.

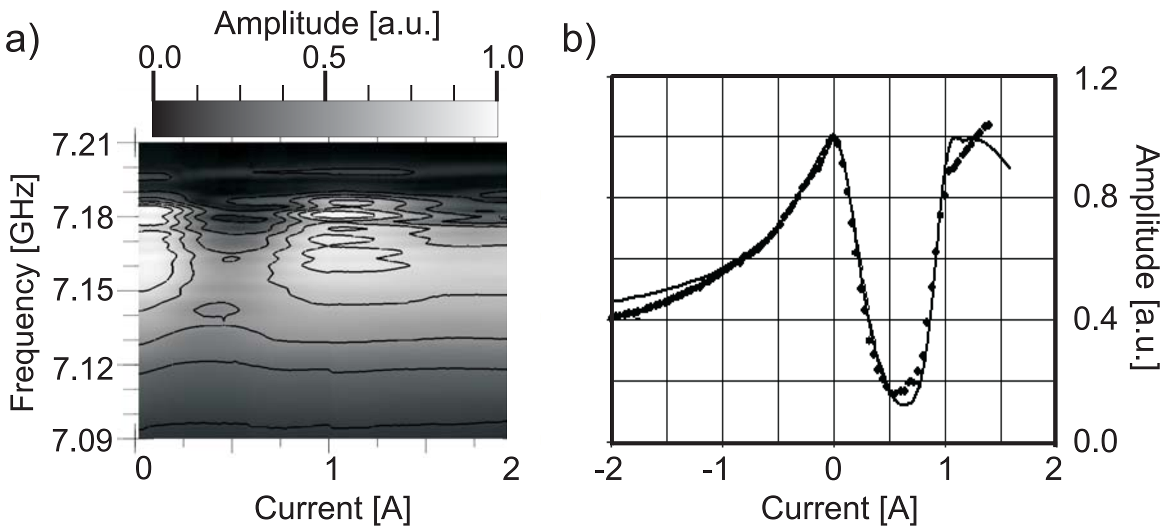

Fig. 3: Data obtained for $H = 1800\,\mathrm{Oe}$; a) amplitude graph for different dc-currents and frequencies of the transmitted signal; b) Experimental (dots) and calculated data (line) for a fixed frequency from [4]

We clearly see that in the case of barrier formation (negative current) the amplitude of the transmitted signal monotonically decreases with increasing absolute value of the dc-current. This can be understood as resulting from the increase of the zone in which the spin wave propagation is prohibited. It has been explained in terms of spin wave tunneling in [3].

The focus of this report is on the other case: For positive currents (well) a non-monotonic behavior of the transmission amplitude is observed with a minimum for a current $I \approx 0.5\,\mathrm{A}$ and a maximum for $I \approx 1.0\,\mathrm{A}$, where the original signal amplitude is almost restored. By varying the frequency, we observed that the transmitted amplitude in the minimum is lower the closer the frequency is to the frequency of ferromagnetic resonance. It can decrease to less than 20% of the undisturbed signal amplitude.

We reported this non-monotonicity in [4], where the minimum was discussed for the first time. Moreover, in [4] a theoretical model was developed and successfully applied to numerically simulate the minimum in transmission.

The extrema can be understood as scattering resonances from the region of the inhomogeneous magnetic field. As for a quantum mechanical well, based on the size of the inhomogeneity, transmission or reflection can be observed depending on whether the waves reflected from the field inhomogeneity interfere with the propagating wave constructively or destructively. However, due to the long-range dipole interaction, the theoretical calculations are more involved in this case.

To derive an equation we first assume a harmonic oscillatory motion for the magnetization and the dynamic magnetic field. Taking the linearized Landau-Lifshitz equation we can specify the effective magnetic fields as the sum of the spin wave dipole fields and the external microwave field exciting the magnetic oscillations. The dipole field of precessing magnetization in the film is then written with the help of a 1D-Green's function representation.

Due to the geometry of the used section we can reduce the dimensionality of the problem and arrive at

$$\chi(x,\omega)^{-1} m_z(x) - \int_{-\infty}^{\infty} 4\pi G_{zz}(x,x') m_z(x') dx' = A\delta(x - x_0) \tag{1}$$

where

$$4\pi G_{zz}(x,x') = \frac{2}{L} ln \frac{(x-x')^2}{L^2+(x-x')^2}$$

with the film thickness $L$ and $\chi(z,\omega)$ denotes the diagonal element of the magnetic susceptibility.

Equation (1) can then be solved numerically or alternatively studied with the help of analytical methods. Some results of these calculations are shown in the right panel of Fig. 3.

To complete the picture in Fig. 4 the measured transmission characteristics for several distinct currents are displayed. No sharp resonances are visible. This is not surprising, since the coupling with the environment is rather strong which leads to high losses. Any resonance line would therefore be expected to be wide and shallow.

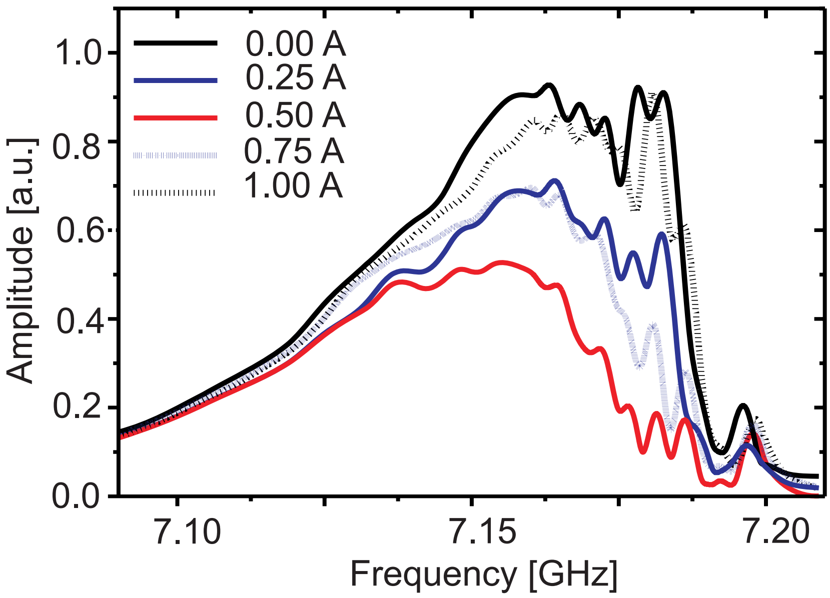

Fig. 4: Transmission characteristics for different applied dc-currents and a bias magnetic field of $H = 1800\,\mathrm{Oe}$

In conclusion, we note that the localized inhomogeneity created by the Oerstedt field of a thin, dc-current carrying wire strongly influences the transmission of dipole-dominated backward volume spin waves. The character of this influence crucially depends on the direction of the current. For negative currents forming a barrier for spin waves the transmission decreases monotonically with increasing absolute current value. For positive currents we observed resonant scattering. These results have to be taken into account when designing magnonic crystals using dc-current carrying wires.

This work has been financially supported by *MATCOR Graduate School of Excellence* and the DFG within the project SE 1771/1-1 “Linear and nonlinear magnonic crystals”.

## References

[1] H. Puszkarski, M. Krawczyk, Solid State Phenomena **94**, 125 (2003).

[2] Y.K. Fetisov, J. Communications Technology and Electronics, **10**, 1171 (2004).

[3] S.O. Demokritov, A.A. Serga, A. Andre, V.E. Demidov, M.P. Kostylev, B. Hillebrands, Phys. Rev. Lett. **93**, 047201 (2004).

[4] M.P. Kostylev, A.A. Serga, T. Schneider, T. Neumann, T.B. Leven, B. Hillebrands, R.L. Stamps, Phys. Rev. B. in press.

## 6.5 Anomalies in microwave assisted switching in $Ni_{81}Fe_{19}$ confined elements

*S.J. Hermsdörfer, H.T. Nembach*[1]*, P. Martín Pimentel, P. Candeloro*[2]*, P.A. Beck, B. Leven, and B. Hillebrands*

Manipulation of the magnetic switching behavior is a fundamental key issue for magnetic data storage in devices like magnetic random access memory (MRAM) or hard disks. For increasing the reliability and switching velocity of small magnetic elements, a number of new techniques like thermally assisted switching have been proposed and developed [1]. Another switching mechanism is the so called microwave assisted switching where the coercive field (i.e., switching field) of a particle is lowered by microwave application [2].

A systematic study of microwave stimulated magnetization switching of $Ni_{81}Fe_{19}$ ellipsoids has been presented by our group recently [3, 4]. Furthermore, the mechanism has been described to work in a magnetic tunnel junction [5] and theoretical studies have been performed for a deeper understanding [6, 7]. The most recent publications use magnetic force microscopy for studying the microwave-assisted magnetization reversal in small magnetic elements [8].
Here we report on anomalies in the hysteresis curves of micron-sized $Ni_{81}Fe_{19}$ elements measured using time resolved magneto-optic Kerr effect magnetometry and an applied transversal field. These anomalies depend strongly on the microwave output power (and therefore on the microwave frequency Oersted field) and the microwave frequency applied. The hysteresis curves presented in other publications [5, 6] show similar effects but up to now no solid explanation has been provided to explain such "cusps" how this phenomenon has been named by [6] or "dips" how they are referred to by [5]. In our opinion, the dips can be attributed to a big oscillation angle of the magnetization due to ferromagnetic resonance.

The quasistatic switching behavior of a 160 µm × 80 µm $Ni_{81}Fe_{19}$ ellipsoid under the influence of a transversal microwave field characterized by magneto-optic Kerr effect magnetometry in longitudinal geometry has been studied. The sample itself has been placed on top of a 430 µm wide microwave antenna. Details of the experimental setup have been reported elsewhere [3, 4]. Hysteresis curves have been measured under the influence of a transversal microwave field, i.e., the field is applied in the plane perpendicular to the quasistatic magnetic field. The frequency of the microwave field was varied in the range from 0.5 GHz to 2.0 GHz in steps of 0.1 GHz and the microwave power was 5 dBm (3.2 mW) to 35 dBm (3.2 W) for each frequency.

The measured hysteresis curves exemplarily presented in Fig. 1 do not only show the reduction of the coercive field reported earlier [3], but exhibit dips at certain magnetic fields. The curves displayed in the first row of Fig. 1 correspond to a fixed microwave frequency of 1.1 GHz and a power range between 5 dBm (3.2 mW) and 35 dBm (3.2 W). Below a power of 10 dBm (10 mW), the hysteresis curves do not show any irregularities, neither a dip nor a reduced coercive field, whereas above this power the dips become clearly evident and the depth (i. e., Kerr signal amplitude) of these anomalies increases up to the maximum applied power of 35 dBm (3.2 W). Also the frequency dependence of the phenomenon has to be noted: the second row in Fig. 1 shows hysteresis loops for a constant microwave power of 30 dBm (1 W) but variable frequencies. As can be

---

[1] Present address: NIST, Electromagnetics Division (m/s 818.01), 325 Broadway, Boulder, CO 80305-3328, USA.

[2] Present address: BioNEM Laboratory, Experimental Medicine Department, University "Magna Graecia" of Catanzaro, v.le Europa - loc. Germaneto, 88100 Catanzaro, Italy.

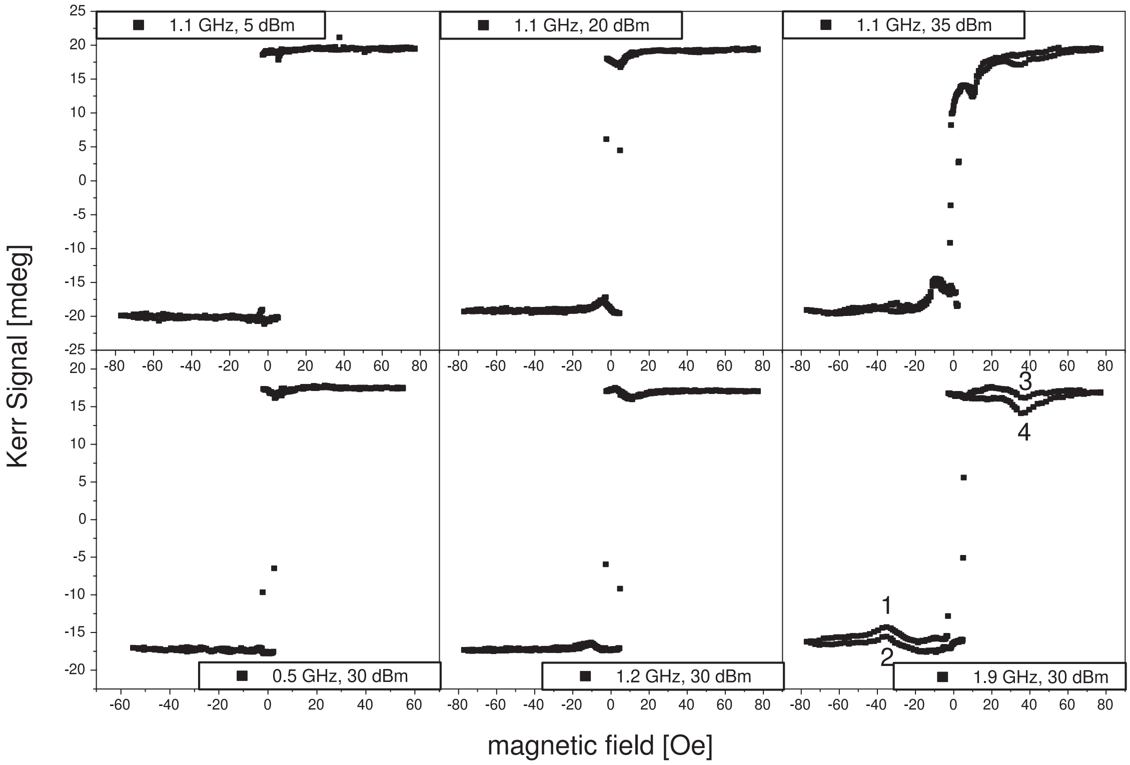

Fig. 1: Hysteresis curves at a fixed frequency of 1.1 GHz (first row) and output powers of 5 dBm (3.2 mW), 20 dBm (100 mW), and 35 dBm (3.2 W) (first row). The dip in the signal can clearly be observed for the microwave output power of 20 dBm and 35 dBm. The second row shows hysteresis curves for a constant output power of 30 dBm (1 W) and a variable frequencies of 0.5 GHz, 1.2 GHz, and 1.9 GHz respectively. The dip position (i. e., Oersted field) moves depending on the frequency to the right as can be seen from the comparison of 1.2 GHz and 1.9 GHz. The numbers shown in the last graph give the dip numbers starting with 1 for the dip at negative field values and 2 at positive field values at the first branch of the hysteresis loop. The number 3 is at positive field values for the back returning branch and number 4 at negative field values, respectively.

seen from the figure, the position of the dip moves towards higher magnetic fields with increasing frequency.

Figure 2 summarizes all data. The grayscale displays the position of the dip at a given value of frequency and power. Figure 2 shows the dependence of the anomalies in the hysteresis curve on the microwave frequency. The reduction of the coercive field appears in the frequency range between 0.8 GHz and 1 GHz whereas the dips can mainly be observed for slightly higher frequencies near 1.1 GHz. For higher frequencies closer to 2 GHz, the appearance of the dips is not that pronounced anymore.

Similar results have been obtained theoretically by Lee et al. [6] (in their paper called “cusps”) as well as in the measurements on magnetic tunnel junctions performed by Moriyama et al. [5].

In our experiments, the magnetic field and the plane of incidence of the laser are parallel to the easy axis of the ellipsoid, whereas the magnetic field created by the microwaves is perpendicular to them. The measured magnetization is the projection of the total magnetization into the plane of incidence. A reduction of the detected magnetization can therefore be due to an increased precession angle of the magnetization which lowers the projection. Hence, the explanation of the observed effect, i.e., a decreased magnetization at certain field values, is the ferromagnetic resonance (FMR).

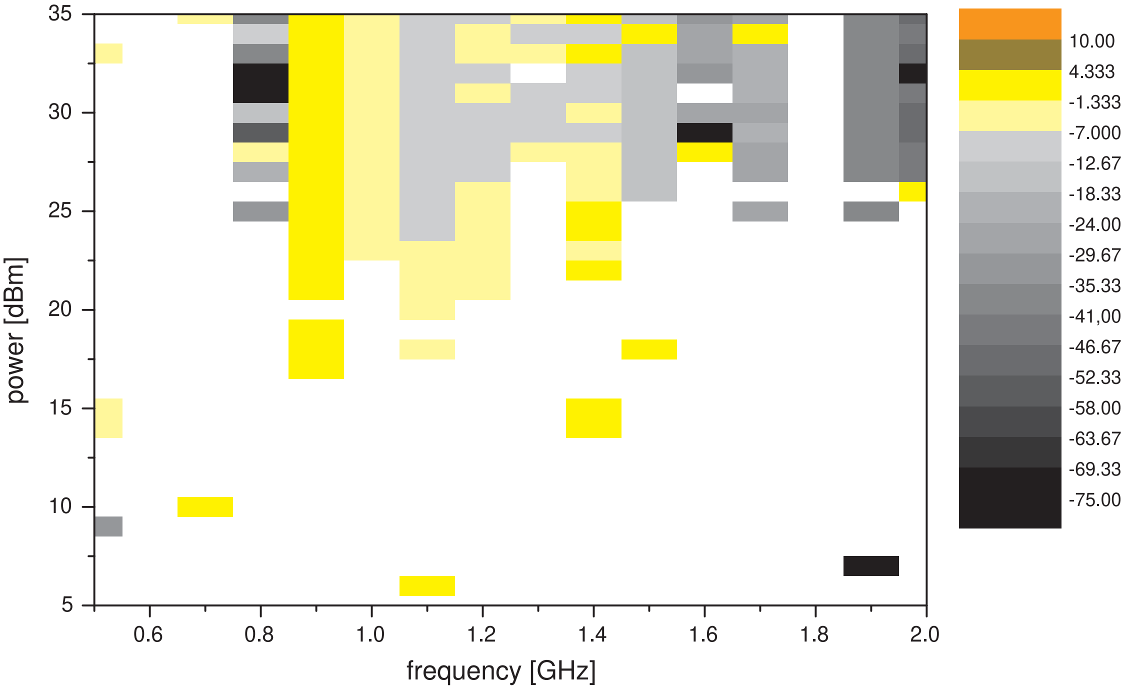

Fig. 2: Each point in this diagram represents a specific value of microwave frequency and output power, the grayscale corresponds to the dip position (i. e., Oersted field) of dip 1 measured at these microwave values. White means that no dip could be found in the hysteresis loops. The dip appears only in a certain range of output powers and only for a specific range of frequencies.

Whenever the resonance conditions obtained from the Kittel equation are fulfilled, more energy is going into the precession and thus the detected magnetization is reduced due to the bigger oscillation angle. Therefore, a smaller projection of the magnetization into the plane of incidence occurs. The precession angle becomes larger the more energy is pumped into this mode, i.e., the more microwave power is applied to the ellipsoid. This explains the increase of the depth of the dip with increasing microwave power. Figure 3 shows the observed dip positions plotted against the expected values for the ferromagnetic resonance obtained by the Kittel equation. The overall behavior of the dips follows the Kittel equation, which proofs that the observed effect is related to the magnetization precession.

The power dependence of the dip position can be explained by the change in the shape of the hysteresis loop at higher power values. In this regime, the hysteresis loops lose their rectangular shape and become rounder as can be seen from the last graph in the first row in Fig. 2. If the dip position is now in the area close to the switching field, i.e., in the part of the loop where the rounding already starts, the dip is overlapped by the decreasing magnetization due to the high microwave power. In this case, the dip position does not change in comparison to lower microwave powers but seems to move due to the changed shape of the loop. This fits with the observation that the dip position is not affected by increasing microwave power if its position is far away from the switching field.

The anomalous behavior of the magnetization during application of microwaves presented in this report can be explained by the fulfillment of resonance conditions at these field and frequency values. It appears in a wide range and can be understood as an increase in the precession angle which lowers the projection of the magnetization in the sample plane and therefore the measured signal.

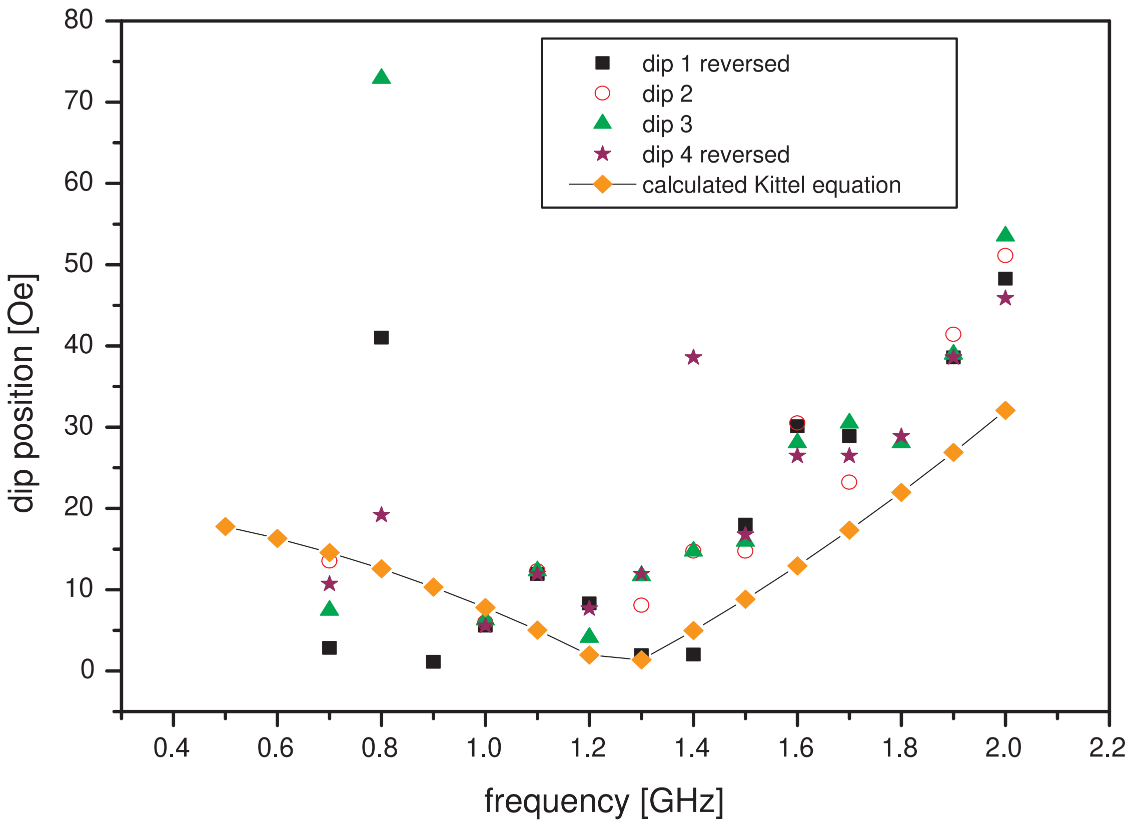

Fig. 3: Position of the dips plotted in comparison to the Kittel equation. The dip names refer to their position in the hysteresis loop, dip 1 and 4 indicate the two dips at negative magnetic field values, dip 2 and 3 at positive values (see Fig. 2). For a better comparison, the absolute field values have been taken. The dip position moves in agreement with the Kittel equation to higher field values at higher frequencies. For the calculation a gyromagnetic ratio of $0.0176\,\mathrm{ns}^{-1}\mathrm{Oe}^{-1}$, a saturation magnetization of 9650 Gauss and an uniaxial anisotropy of 7.7 Oe have been assumed. The latter two values have been obtained from FMR measurements at the sample.

The authors would like to thank the Nano+Bio Center of the Technische Universität Kaiserslautern for technical support. Financial support by the European Commission within the EU-RTN ULTRASWITCH (HPRN-CT-2002-00318) and the DFG within the SPP1133 is gratefully acknowledged. Furthermore, the work and results reported in this publication were obtained with research funding from the European Community under the Sixth Framework Programme Contract Number 510993:MAGLOG.

## References

[1] H.F. Hamann, Y.C. Martin, H.K. Wickramasinghe, Appl. Phys. Lett. **84**, 810 (2004)
[2] C. Thirion, W. Wernsdorfer, D. Mailly, Nature Mat. **2**, 524 (2003)
[3] H.T. Nembach, P. Martín Pimentel, S.J. Hermsdörfer, B. Leven, B. Hillebrands, Appl. Phys. Lett. **90**, 062503 (2007).
[4] P. Martín Pimentel, H. Grimm, B. Leven, B. Hillebrands, J. Appl. Phys. **102**, 063913 (2007).
[5] T. Moriyama, R. Cao, John Q. Xiao, J. Lu, X. R. Wang, Q. Wen, H. W. Zhang, Appl. Phys. Lett. **90**, 152503 (2007).
[6] H. K. Lee and Z. Yuan, J. Appl. Phys. **101**, 033903 (2007).
[7] Y. Nozaki, K. Tateishi, S. Taharazako, M. Ohta, S. Yoshimura, K. Matsuyama, Appl. Phys. Lett. **91**, 122505 (2007).
[8] Y. Nozaki, M. Ohta, S. Taharazako, K. Tateishi, S. Yoshimura, K. Matsuyama, Appl. Phys. Lett. **91**, 082510 (2007).

# B. Magnetic Films of Heusler Compounds

## 6.6 Exchange stiffness constant in $Co_2MnSi$ and $Co_2Cr_{0.6}Fe_{0.4}Al$ Heusler compounds

*J. Hamrle, O. Gaier, H. Schultheiss, Seong-Gi Min, and B. Hillebrands*[1]

The exchange constant describes the strength of the exchange interaction inside a ferromagnetic system. It is therefore an important parameter from both fundamental and application points of view, such as *ab-initio* and micromagnetic calculations. Here, we are determining the exchange constant of $Co_2Cr_{0.6}Fe_{0.4}Al$ (CCFA) and $Co_2MnSi$ using Brillouin light scattering spectroscopy (BLS).

The CCFA structure under investigation was an Al(2.5 nm)/CCFA(80 nm)/Cr(8 nm)/MgO(100) epitaxial structure [1, 2] grown at the University of Mainz. The Cr buffer layer was deposited by electron beam evaporation onto a single-crystalline MgO(001) substrate, while the epitaxial B2-ordered CCFA film was subsequently deposited by direct-current magnetron sputtering. The investigated $Co_2MnSi$ samples consist of an epitaxial Al(1.3 nm)/$Co_2MnSi$(t)/Cr(40 nm)/MgO(100) structure fabricated at the Tohoku University, Japan by means of inductively coupled plasma-assisted magnetron sputtering. The thickness of the $Co_2MnSi$ layer was chosen as $t = 20$, 30, 40 and 60 nm. All the studied $Co_2MnSi$ films exhibited $L2_1$ order which was obtained by annealing the samples at $T_a = 500°C$ after deposition [3].

All BLS measurements presented in this report were performed using a laser with a wavelength of 532 nm at an incidence angle of 45°. The corresponding transferred wave vector of detected magnons was $q_{||} = 1.73 \cdot 10^5 cm^{-1}$. The external magnetic field was applied in so-called magnetostatic surface mode geometry, i.e., $\mathbf{H}$ parallel to the film and perpendicular to the plane of light incidence (i.e., $\mathbf{H} \perp \mathbf{q}_{||}$) Typical BLS spectra measured on the investigated CCFA film are presented in Fig. 1 for several values of the external magnetic field. Four peaks corresponding to the Damon-Eshbach (DE) mode and to the perpendicular standing spin-wave (PSSW) modes are clearly resolved. As is later shown in this report, the second observed peak in the BLS spectra

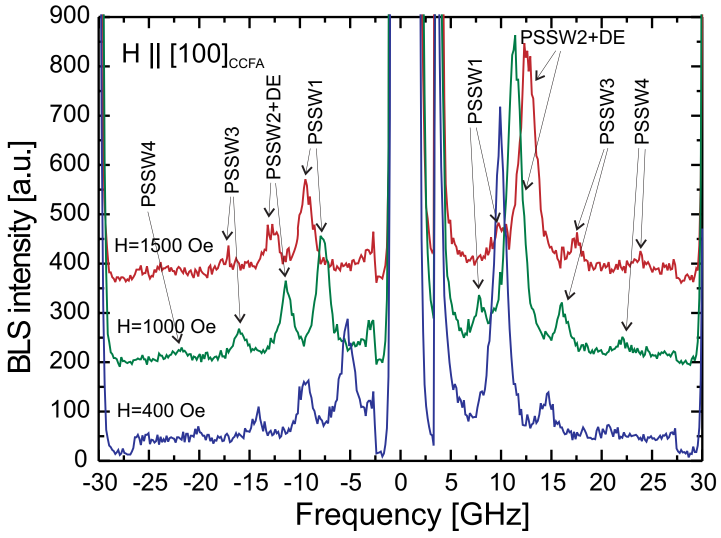

Fig. 1: Example of BLS spectra measured on the CCFA(80nm) film in an external magnetic field of $H = 400$, 1000 and 1500 Oe. Negative frequencies are related to Stokes processes (creation of magnons), whereas positive frequencies are related to anti-Stokes processes (annihilation of magnons).

---

[1] In collaboration with M. Jourdan, Johannes-Gutenberg-Universität Mainz, Germany, Y. Sakuraba, M. Oogane, Y. Ando, Tohoku University, Japan.

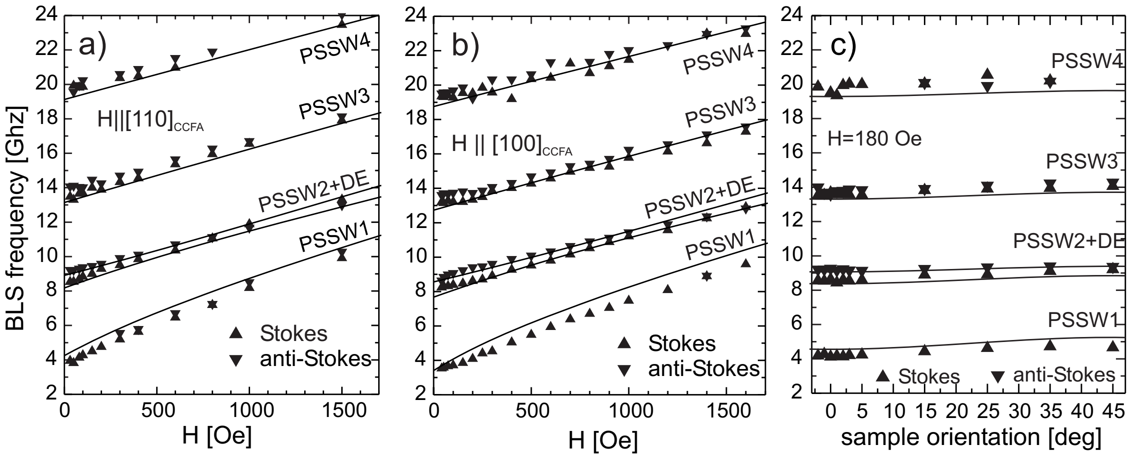

Fig. 2: (symbols) a)b) Dependence of the experimental BLS frequencies on the external magnetic field for $H$ applied along a) $[110]_{\mathrm{CCFA}}$ b) $[100]_{\mathrm{CCFA}}$ axis. c) Dependence of the BLS frequencies on the sample orientation, i.e., angle between $[100]_{\mathrm{CCFA}}$ axis and in-plane applied magnetic field. Triangles-up (down) refer to Stokes (anti-Stokes) frequencies of BLS spectra. (solid lines) calculated spin-wave frequencies in CCFA(80 nm) using exchange constant $A = 0.48\,\mu\mathrm{erg/cm}$, saturation magnetization $M_\mathrm{s} = 520\,\mathrm{emu/cm}^3$, Landau $g$-factor $g = 1.9$, transferred $k$-vector $q_{||} = 1.73 \cdot 10^5\mathrm{cm}^{-1}$ and cubic volume anisotropy $K_1 = -2.0 \cdot 10^4\,\mathrm{erg/cm}^3$.

results from the hybridization of the DE and the second PSSW mode, whereas the other observed peaks are pure PSSW modes.

Figures 2a and 2b visualize the dependence of the observed spin wave frequencies on the value of the external magnetic field which was applied along (Fig. 2a) the [110] and (Fig. 2b) the [100] axis of the CCFA film. The field dependences are nearly identical for both orientations of the external magnetic field. However, the observed spin wave frequencies are about 1 GHz smaller for the case of **H** aligned parallel to the $[100]_{\mathrm{CCFA}}$ direction. This demonstrates that the $[100]_{\mathrm{CCFA}}$ is a magnetically hard axis, in agreement with MOKE investigations [2]. The dependence of the observed spin-wave frequencies on the sample orientation is presented in Fig. 2c. The full lines in Fig. 2a, 2b and 2c are a fit to the experimental data which was obtained by using a theoretical model described in Ref. [4] and the following fitting parameters: exchange constant $A = 0.48 \pm 0.02\,\mu\mathrm{erg/cm}$, saturation magnetization $M_\mathrm{s} = 520 \pm 20\,\mathrm{emu/cm}^3$, Landau $g$-factor $g = 1.9 \pm 0.1$ and cubic volume anisotropy $K_1 = (-2 \pm 1) \cdot 10^4\,\mathrm{erg/cm}^3$. The value of the Landau g-factor was determined from the slope of the $f(H)$ curves presented in Figures 2a and 2b. The saturation magnetization was obtained from the frequencies of the DE mode and agrees with the value of $M_\mathrm{s} = 480\,\mathrm{emu/cm}^3$

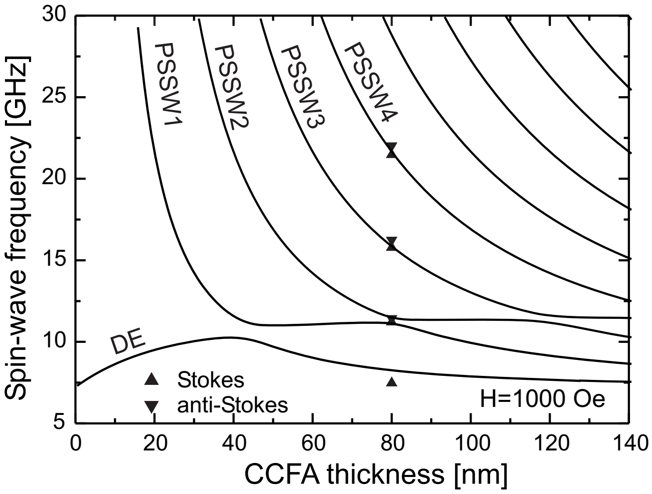

Fig. 3: Calculated dependence of spin-wave frequencies on the thickness of the CCFA film for $H = 1000\,\mathrm{Oe}$, $H \parallel [100]_{\mathrm{CCFA}}$. Symbols represent experimental data. The parameters used in simulations are the same as in Fig. 2.

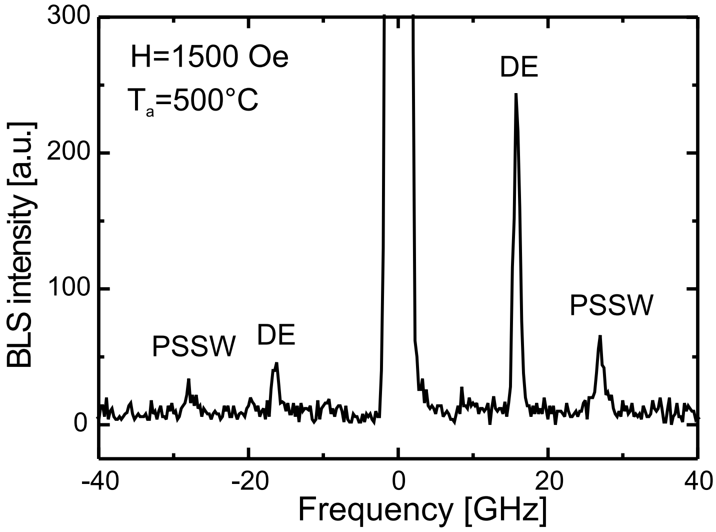

Fig. 4: Example of BLS spectra in a $Co_2MnSi$(30 nm) film recorded in an external magnetic field of $H = 1500\,\mathrm{Oe}$.

determined by SQUID [1]. As the DE and PSSW2 modes are hybridized, the determination of $M_s$ has a rather large error bar in this particular case. Finally, $A$ and $K_1$ were determined from the frequencies of the PSSW modes and from the dependence of BLS frequencies on the sample orientation (Fig. 2c), respectively.

For small values of the external field in the range of 100–200 Oe, we observe a large (about 1 GHz) splitting between the Stokes (▲, creation of magnons, negative frequencies in BLS spectra) and the anti-Stokes (▼, annihilation of magnons, positive frequencies in BLS spectra) frequencies of the PSSW2+DE mode (Figs. 2a and 2b). Moreover, the slope df/dH is slightly different for Stokes and anti-Stokes frequencies. Such an asymmetry is rather surprising, because both processes are related to the same spin-wave mode which in most cases results in symmetric values for the Stokes and the anti-Stokes frequencies. In our particular case, the observed asymmetry is probably related to a combination of the CCFA film thickness of 80 nm and transferred wave vector $q_{||} = 1.73 \cdot 10^5\,\mathrm{cm}^{-1}$ giving rise to the hybridization of the DE and the PSSW2 modes. The hybridization provides mode splitting (also called mode repulsion), creating two very close energetic levels for magnons. The hybridization is presented in Fig. 3, where the calculated dependence of spin-wave frequencies on the CCFA film thickness is shown for the external magnetic field of $H = 1000\,\mathrm{Oe}$ applied along the $[100]_{\mathrm{CCFA}}$ axis. We can see that for $t_{\mathrm{CCFA}} = 80\,\mathrm{nm}$, the DE and PSSW2 modes are crossing each other, creating a gap of about 0.3 GHz. Another origin of the observed asymmetry between Stokes and anti-Stokes frequencies may be the gradient in the internal field perpendicular to the film. It may be caused either by gradient in the magnetization or by gradient in the magnetic anisotropy.

Furthermore, we have investigated $Co_2MnSi$ films with different thicknesses using the BLS technique. Typical BLS spectra measured on a 30 nm thick $Co_2MnSi$ film are shown in Fig. 4. BLS frequencies as a function of the sample thickness are presented in Fig. 5 by square symbols (■) for $H = 1500\,\mathrm{Oe}$. Solid lines in this figure represent model calculations for which the saturation magnetization of $M_s$=1013 emu/cm$^3$ determined by Vibrating Sample Magnetometry (VSM) [3] was used. The calculations were performed for two different values of the exchange constant $A$ which are 2.5 μerg/cm and 0.6 μerg/cm. The corresponding calculated dependencies of the BLS frequencies on the film thickness are shown in Fig. 5a and 5b, respectively . From these figures we can see that both values of $A$ give a good agreement between the observed and the calculated spin-wave frequencies. In case 5b, however, only even PSSW modes are experimentally detected which makes this case rather improbable. On the other hand, the value of the exchange constant $A = 2.5\,\mu\mathrm{erg/cm}$ found in case 5a is very high, it is nearly as high as the value of hcp Co and

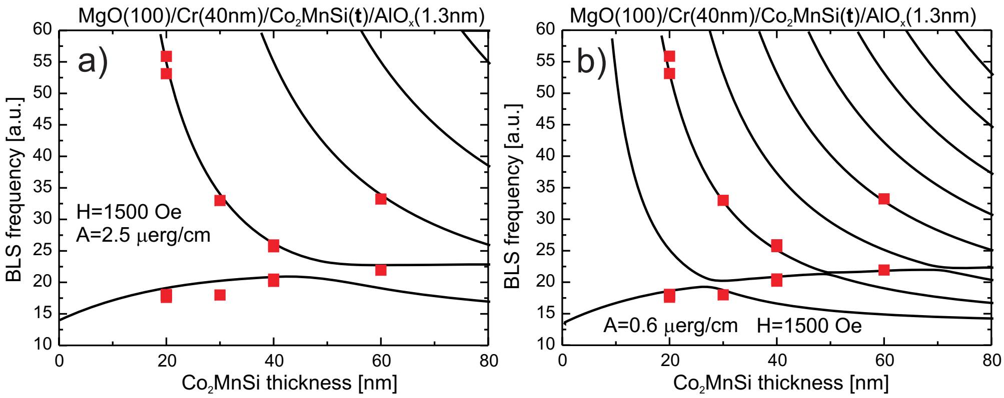

Fig. 5: (symbols) Experimental BLS frequencies for $Co_2MnSi$ films with different thicknesses at an external field of $H = 1500\,\mathrm{Oe}$. (solid lines) Calculated spin-wave frequencies in $Co_2MnSi$ using saturation magnetization $M_s$=1013 emu/cm$^3$, Landau $g$-factor $g = 2.05$, transferred $k$-vector $q_{\|} = 1.73 \cdot 10^5 \mathrm{cm}^{-1}$ and exchange constant a) $A = 2.5\,\mu\mathrm{erg/cm}$ or b) $A = 0.6\,\mu\mathrm{erg/cm}$. Magnetic anisotropies are neglected [3].

even higher than the corresponding value of bcc Co (see Table 1). This seems to be astonishing for the $Co_2MnSi$ compound, because bulk Mn and Si is a paramagnet and a diamagnet at room temperature, respectively. More measurements are required to clarify this issue.

Table 1 gives an overview of the exchange constant $A$, the saturation magnetization $M_s$ and the exchange stiffness $D = 2A/M_s$ for various materials. Note that the values of the exchange constant of CCFA and $Co_2MnSi$ determined within the frame of this work do not correspond with those found in Refs. [5, 6] (shown in parenthesis in Tab. 1). This discrepancy is probably related to the fact that in Ref. [5], the exchange constant $A$ of $Co_2MnSi$ was estimated using the dependence of the saturation magnetization on the sample temperature, which is just an estimate. In Ref. [6], the exchange constant in CCFA and $Co_2MnSi$ was determined by FMR, assuming asymmetrical pinning conditions (i.e., spins at one surface are unpinned, whereas those at the second surface are strongly pinned). However, if those pinning conditions would take place, then the Stokes and anti-Stokes frequencies in DE mode would be different, which we have not observed.

The project was financially supported by the Research Unit 559 *“New materials with high spin*

| | Exchange constant $A$ [μerg/cm] | Saturation magnetization $M_s$ [emu/cm$^3$] | Exchange stiffness $D = 2A/M_s$ [nOe/cm$^2$] |
|---|---|---|---|
| CCFA | $0.48 \pm 0.04^*$<br>(0.255 [6]) | $520 \pm 20^*$<br>(480 [1]) | $1.8^*$ |
| $Co_2MnSi$ | $2.5 \pm 0.1^*$ or<br>$0.60 \pm 0.05^*$<br>(0.95 [5, 6]) | $1013^*$ [3] | $4.9^*$ or<br>$1.18^*$ |
| Fe(bcc) | 2.0 | 1752 | 2.28 |
| Co(hcp) | 2.87 [7] | 1420 [7] | 4.04 |
| Co(bcc) | 1.6 [7] | 1230 [7] | 2.6 |

Table 1: Comparison of exchange constant $A$, saturation magnetization $M_s$ and exchange stiffness $D$ for various Heusler compounds and d-metals. The asterix denotes values determined within this work.

*polarization"* funded by the Deutsche Forschungsgemeinschaft, by the NEDO International Joint Research Grant Programm 2004/T093 and and by the Stiftung Rheinland-Pfalz für Innovation.

## References

[1] A. Conca, M. Jourdan, C. Herbort, H. Adrian, J. Cryst. Growth **299**, 299 (2007).

[2] J. Hamrle, S. Blomeier, O. Gaier, B. Hillebrands, R. Schäfer, M. Jourdan, J. Appl. Phys. **100**, 103904 (2006).

[3] O. Gaier, J. Hamrle, S.J. Hermsdörfer, H. Schultheiss, B. Hillebrands, Y. Sakuraba, M. Oogane, Y. Ando, submitted to J. Appl. Phys. (2007), arXiv:0708.3303v1, see also Sect. 6.7.

[4] B. Hillebrands, Phys. Rev. B **41**, 530 (1990).

[5] L. Ritchie, G. Xiao, Y. Ji, T.Y. Chen, C.L. Chien, M. Zhang, J. Chen, Z. Liu, G. Wu, X.X. Zhang, Phys. Rev. B **68**, 104430 (2003).

[6] B. Rameev, F. Yildiz, S. Kazan, B. Aktas, A. Gupta, L.R. Tagirov, D. Rata, D. Buergler, P. Grünberg, C.M. Schneider, S. Kämmerer, G. Reiss, A. Hütten, Phys. Stat. Sol. (a) **203**, 1503 (2006).

[7] J.M. Karanikas, R. Sooryakumar, G.A. Prinz, B.T. Jonker, J. Appl. Phys. **69**, 6120 (1991).

## 6.7 Dependence of $L2_1$ ordering on magnetic properties in $Co_2MnSi$ Heusler compound

*O. Gaier, J. Hamrle, S. Hermsdörfer, H. Schultheiss, and B. Hillebrands*[1]

In this Section we report on the dependence of magnetic properties on the degree of the $L2_1$ order in $Co_2MnSi$ Heusler films. In recent years, the $Co_2MnSi$ Heusler compound has been subject to extensive research work due to its half-metallic property predicted by *ab initio* calculations [1]. However, 100 % spin polarisation of a $Co_2MnSi$ Heusler compound has never been observed experimentally. One of the main reasons for this is believed to be a strong dependence of the half-metallicity on the disorder in the crystal lattice [2].

To investigate the influence of the ordering degree on the magnetic properties of the $Co_2MnSi$ Heusler compound, 30 nm thin epitaxial films with different fractions of the $L2_1$ phase were grown in the group of Prof. Ando, Sendai, Japan by means of inductively coupled plasma-assisted magnetron sputtering. Different degrees of the $L2_1$ order were achieved by annealing the samples at different temperatures $T_a$ after their deposition. $T_a$ was varied in the range between 350 °C and 500 °C. For the analysis of the crystallographic properties of the investigated $Co_2MnSi$ films, X-ray diffraction (XRD) measurements using Cu-$K_\alpha$ radiation, were also carried out in Sendai. In order to quantify the $L2_1$ ordering degree in our samples, the long-range order parameter $S_{L2_1}$ was calculated from the intensities of the (111) superstructure and the (220) fundamental reflections:

$$S^2_{L2_1} = \frac{I_{obs}(111)/I_{obs}(220)}{I_{cal}(111)/I_{cal}(220)} \qquad (1)$$

In this equation, $I_{obs}$ and $I_{cal}$ are the peak intensities obtained experimentally and from numerical simulations, respectively. The calculated values of the $S_{L2_1}$ parameter presented in Fig. 1 show that the $L2_1$ ordering degree of the investigated $Co_2MnSi$ films increases with increasing $T_a$. While the $Co_2MnSi$ film annealed at $T_a = 350\,°C$ is less than 60 % $L2_1$ ordered, the corresponding value is nearly 90 % for $T_a = 500\,°C$. In the following we first describe how the coercivity of $Co_2MnSi$ is influenced by the degree of $L2_1$ order. Then we report on the dependence between $S_{L2_1}$ and both the exchange and anisotropy constants of the investigated $Co_2MnSi$ films.

In order to study the influence of the $L2_1$ order on the coercive field $H_C$ of the $Co_2MnSi$ Heusler films, we performed hysteresis loop measurements by means of a standard magneto-optical Kerr

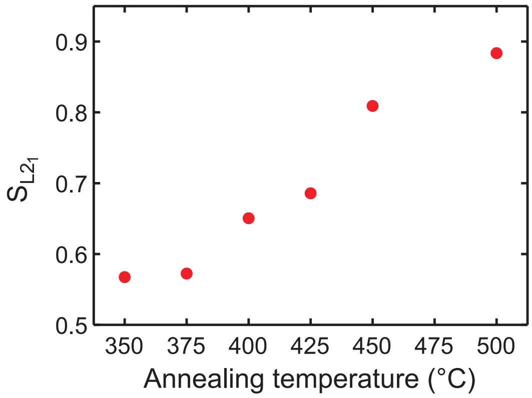

Fig. 1: Long-range order parameter $S_{L2_1}$ for $Co_2MnSi$ films annealed at different temperatures after the deposition. The values of $S_{L2_1}$ were obtained from a detailed analysis of the (111) and (220) reflections measured by XRD.

---

[1] In collaboration with Y. Ando, Y. Sakuraba, M. Oogane, Tohoku University, Sendai, Japan.

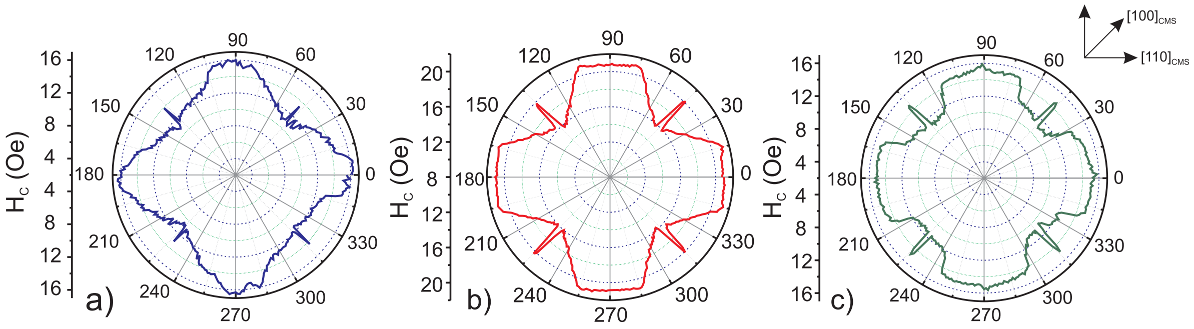

Fig. 2: Dependence of $H_C$ on sample orientation α for $Co_2MnSi$ films annealed at a) 350 °C, b) 425 °C and c) 500 °C. α denotes the angle between the external magnetic field $H$ and the [110] crystallographic direction of the $Co_2MnSi$ films.

effect (MOKE) set-up in the longitudinal geometry. The sample position was varied in steps of 1° from $\alpha = 0°$ to 360° with α being the angle between the in-plane [110] direction of the $Co_2MnSi$ film and the direction of the applied magnetic field $H$.

The dependence between $H_C$ values determined from the MOKE loops and α is shown in Fig. 2 for the $Co_2MnSi$ films annealed at $T_a = 350\,°C$, 425 °C and 500 °C. The rotational scans of all the investigated films exhibit a four-fold anisotropy which is in agreement with the cubic symmetry of the crystal structure. Narrow peaks in $H_C$ at $\alpha = 45° + n \cdot 90°$, $n = 0 \ldots 3$ (i.e. in hard axis direction) clearly visible in Fig. 2 are related to magnetization frustration during the magnetization reversal process in hard axis orientations, accompanied by formation of a particular domain pattern. This reversal process has thoroughly been studied for $Co_2Cr_{0.6}Fe_{0.4}Al$ Heusler films and will not be further discussed here [3].

Figure 3 visualizes the dependence of $H_C$ on the annealing temperature $T_a$ for $\alpha = 0°$, 42° and 45°. The values of $H_C$ exhibit a maximum for the $Co_2MnSi$ film annealed at 425° independently from the sample orientation α. This feature is probably related to an enhanced number of pinning centers which might originate from the diffusion of Cr atoms into the $Co_2MnSi$ film from the buffer layer used for the film deposition.

Furthermore, we studied the spin wave exitations in the $Co_2MnSi$ with different degrees of the $L2_1$ order by means of the Brillouin light scattering (BLS) technique. Figure 4a shows a representative BLS spectrum recorded at an external magnetic field of 1500 Oe and a transferred wave vector

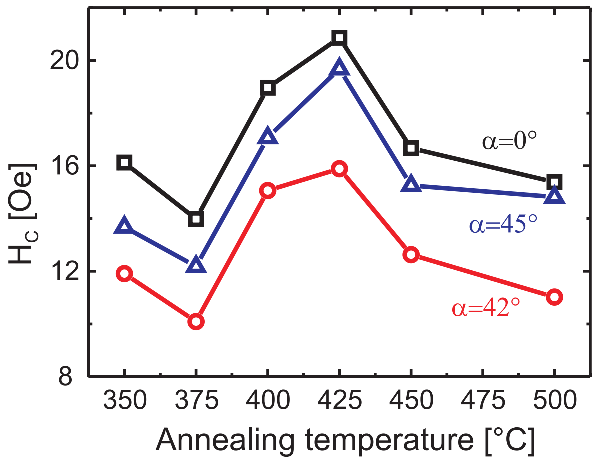

Fig. 3: Dependence of $H_C$ on the annealing temperature $T_a$ for sample orientations $\alpha = 0°$, 42° and 45°. Maximum of $H_C$ at $T_a = 425\,°C$ are indicative for an enhanced number of pinning centers.

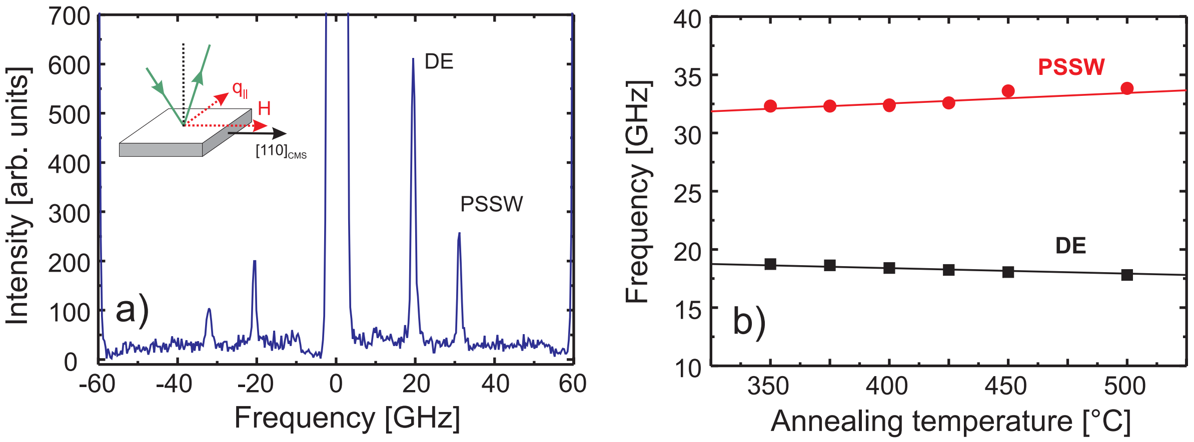

Fig. 4: a) BLS spectrum recorded at an external magnetic field of 1500 Oe and at a transferred wave vector of $q_{\parallel} = 1.67 \cdot 10^5\,\mathrm{cm}^{-1}$ from the $Co_2MnSi$ film annealed at 400 °C. In the inset the measuring geometry is shown. b) Dependence of spin wave frequencies on the annealing temperature of the $Co_2MnSi$ films. The frequencies were determined from BLS spectra measured at an applied magnetic field of $H = 2000\,\mathrm{Oe}$ and a transferred wave vector of $q_{\parallel} = 1.18 \cdot 10^5\,\mathrm{cm}^{-1}$.

of $q_{\parallel} = 1.67 \cdot 10^5\,\mathrm{cm}^{-1}$ from the $Co_2MnSi$ film annealed at 400 °C. The peak at around 20 GHz can be attributed to the dipole dominated Damon-Esbach mode (DE), while the peak appearing at approximately 32 GHz results from the excitation of the exchange dominated perpendicular standing spin wave (PSSW).

The characteristic shape of the BLS spectrum remains unmodified for all the investigated samples. A closer analysis of the spectral peak positions, however, reveals that the frequency of the DE mode decreases by about 1 GHz when $T_a$ is changed from 350 °C to 500 °C while the frequency of the PSSW mode increases by about 1.5 GHz (Fig. 4b). For fixed experimental conditions, it can be shown that in the case of week exchange contribution and negligible anisotropies the frequency of the DE mode only depends on the saturation magnetization $M_s$ [4]. The frequencies of the PSSW modes, however, exhibit an inverse dependence on $M_s$ and, in addition, are a function of the exchange stiffness constant $A$. Therefore, the observed frequency shift of the DE mode is related to a reduction of $M_s$, while the changes of the PSSW mode frequencies might additionally be caused by an increase of $A$. From numerical simulations based on a theoretical model described in Ref. [5] we could estimate that in the $Co_2MnSi$ film with the smallest degree of $L2_1$ order the $M_s$ value is about 9 % higher and $A$ value is about by 8 % lower than the corresponding values for the $Co_2MnSi$ sample with the highest amount of the $L2_1$ phase. Unfortunately, the absolute values of $A$ could not be determined, because only a single PSSW mode was present in the BLS spectra. However, the exchange constant $A$ for $Co_2MnSi$ is determined in Section 6.6, using different thicknesses of $Co_2MnSi$ films.

In addition to the BLS studies described above, we also investigated the dependence of the DE mode frequencies on the in-plane sample orientation for $Co_2MnSi$ films annealed at $T_a = 350$ °C, 375 °C, 400 °C, 550 °C and 500 °C. From these measurements, the cubic volume anisotropy constant $K_1$ and its correlation with the degree of the $L2_1$ order in the $Co_2MnSi$ samples could be extracted.

For example, Fig. 5a shows the dependence of the DE mode frequency on the sample orientation with respect to the external magnetic field $H$ for the $Co_2MnSi$ film annealed at $T_a = 375$ °C. A four-fold anisotropy is clearly visible in this figure which is in agreement with the results obtained from

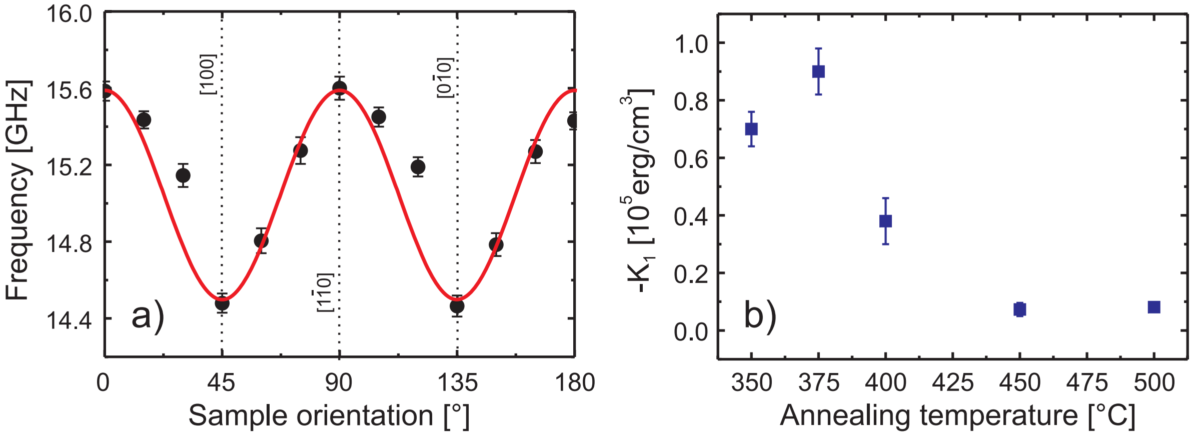

Fig. 5: a) Frequency of the DE mode as function of the angle between the external magnetic field $H = 300\,\mathrm{Oe}$ and the [110] easy axis direction for the $Co_2MnSi$ film annealed at 375 °C. b) Dependence of the volume anisotropy constant $K_1$ on the annealing temperature $T_a$.

MOKE studies. Minima of DE mode frequencies appear at hard axis directions, whereas maxima of the DE frequencies indicate easy axis directions. For the determination of the $K_1$ values, the experimental data were fitted using a theoretical model described in Ref. [5]. The corresponding fit for the $Co_2MnSi$ film with $T_a = 375\,°\mathrm{C}$ is visualized in Fig. 5a as well. The dependence of $K_1$ values on $T_a$ is presented in Fig. 5b, which shows a drop of $K_1$ by a factor of 10. This behavior might be related to the improvement of the $L2_1$ structure with the increasing $T_a$. However, it might also be influenced by the diffusion of Cr as previously mentioned.

The project was financially supported by the Research Unit 559 *"New materials with high spin polarization"* funded by the Deutsche Forschungsgemeinschaft, by the NEDO International Joint Research Grant Programm 2004/T093 and by the Stiftung Rheinland-Pfalz für Innovation.

## References

[1] I. Galanakis, P.H. Dederichs, N. Papanikolaou, Phys. Rev. B **66**, 174429 (2002).
[2] S. Picozzi, A. Continenza, A.J. Freeman, Phys. Rev. B **69**, 094423 (2004).
[3] J. Hamrle, S. Blomeier, O. Gaier, B. Hillebrands, R. Schäfer, M. Jourdan, J. Appl. Phys. **100**, 103904 (2006).
[4] S.O. Demokritov, B. Hillebrands, A.N. Slavin, Physics Reports **348**, 441 (2001).
[5] B. Hillebrands, Phys. Rev. B **41**, 530 (1990).

## 6.8 $Co_2MnAl_xSi_{1-x}$ Heusler compound investigated by Brillouin light spectroscopy and magneto-optical Kerr effect magnetometry

*T. Kubota*[1]*, J. Hamrle, O. Gaier, and B. Hillebrands* [2]

In the field of spintronics 100 % spin-polarized materials, so called half-metals, are of a large interest. One of the promising candidate is the $Co_2$-based full-Heusler compound $Co_2MnSi$ due to the theoretically predicted high spin-polarization [1], which was consequently experimentally confirmed by an extremely large tunnel magnetoresistance (TMR) effect in magnetic tunnel junctions with $Co_2MnSi$ electrodes [2].

Here, we report on the investigation of the magnetic properties of the $Co_2MnAl_xSi_{1-x}$ (CMAS) Heusler compound by use of Brillouin light scattering spectroscopy (BLS) and magneto-optical Kerr effect (MOKE) magnetometry. The investigated magnetic properties within this report are the exchange constant, the magnetic anisotropy, the saturation magnetization, the magnetization reversal, and the coercive field.

The CMAS structures under investigations MgO(001)/Cr(40 nm)/CMAS(30 nm)/Ta(2 nm) with nominal Al composition $x$ ranging from 0 to 1.0 were prepared at Tohoku University. All layers were deposited by magnetron sputtering onto a single-crystalline MgO(001) substrate at room temperature. After the deposition of Cr and CMAS films, *in-situ* annealing was performed at temperatures of 700 °C and 500 °C, respectively. A Ta layer of 2 nm thickness was deposited as a protection layer.

The analysis of the crystal structure of the prepared CMAS samples by x-ray diffraction (XRD) was also carried out at Tohoku University. For CMAS films with nominal Al content in a range from $x = 0$ to 0.2 as well as for a value $x = 1.0$, clear (002) and (004) peaks were observed in $\theta$-$2\theta$-profiles (Fig. 1a) confirming the B2 structure of these films. Unfortunately, the corresponding $\theta$-$2\theta$-profiles are missing for the samples with $x = 0.3$ and 0.4 investigated within the frame of this work. In our previous studies, however, we have found a random occurrence of the B2 structure in the CMAS films at this particular composition. Figure 1a also shows that the diffraction peaks of CMAS gradually shift towards those of $Co_2MnAl$ when the Al content $x$ is increased in the range between 0 to 0.2. This shift is related to an increase of the lattice constant of CMAS in this particular range of $x$, as presented in Fig. 1b. It also correlates with a monotonic decrease of the full width at half maxima (FWHM) which we observe for the rocking curves of the CMAS (004) peaks (Fig. 1c). Note that for further increase of Al content $x$, the lattice constant of B2 ordered CMAS does not suit the linear dependence (Vegard's law) found in the range between 0 and 0.2. Furthermore, the FWHM of the (004) rocking curve increases for $x = 0.3$ and 0.4 in contrast to the monotonic decrease observed in the range between 0 and 0.2. A phase separation between CMAS and $Co_2MnSi$ (or $Co_2MnAl$) at $x$ values above 0.2 might be a possible reason for these experimental findings.

To study the dependence of spin-wave excitations in the CMAS films on the Al content $x$, we performed BLS measurements using a laser with a wavelength of 532 nm at an incidence angle of

---

[1] T. Kubota is a Ph.D. student in the group of Y. Ando, Tohoku University, Sendai, Japan. He has spend an one month research stay at the University of Kaiserslautern. This report provides a summary of the accomplished work during his stay.

[2] In collaboration with Y. Sakuraba, M. Oogane, Y. Ando, Tohoku University, Sendai, Japan

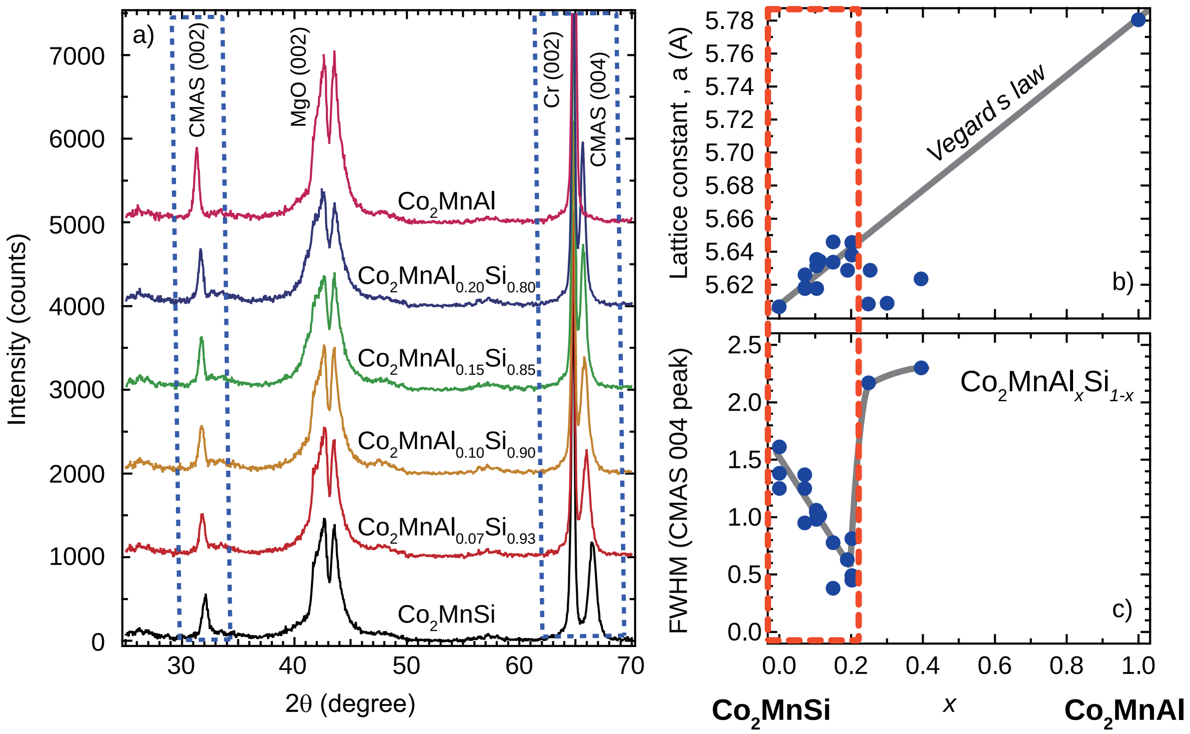

Fig. 1: a) XRD profiles of (001)-epitaxial $Co_2MnAl_xSi_{1-x}$ (CMAS) films, b) estimated lattice constant of CMAS and c) full width at half maxima (FWHM) of the (004) peak. At the nominal composition $x$, ranging from 0 to 0.2, the lattice constant linearly increases towards the value of $Co_2MnAl$ and the FWHM monotonically decreases. For $x$ values above 0.2, the lattice constant is suddenly decreased and the FWHM is increased.

45 °, which provides the transferred wave vector of detected magnons to be $q_{\|} = 1.67 \cdot 10^5\,\mathrm{cm}^{-1}$. Typical BLS spectra recorded on CMAS ($x = 0.4$) at several values of the external magnetic field are presented in Fig. 2a. Two spin-wave peaks originating from the Damon-Eshbach (DE) and perpendicular standing spin-wave (PSSW) modes are visible in this Figure. The dependence of the BLS spectra on the composition of the CMAS films is shown in Fig. 2b. The characteristic shape of the BLS spectra does not change upon the variation of the nominal Al content $x$, i.e. only two spin-wave peaks are detected for all values of $x$. The peak frequencies, however, exhibit clear shifts with change of the CMAS composition. The PSSW mode frequencies, which values are dominantly determined by the exchange constant $A$ [3], decrease with increasing $x$. On the other hand, the DE mode frequencies, determined dominantly by the saturation magnetization $4\pi M_s$, increase up to $x = 0.2$ and subsequently decrease for $x = 0.3$ and 0.4. Furthermore, the frequency of the DE mode exhibits an oscillating dependence on the sample orientation as demonstrated in Fig. 3. The frequency variation reflects the change of magnetic anisotropy energy for different magnetization directions. Hence, for example, the frequency maxima correspond to an easy axis direction, being here the $\langle 110 \rangle$ CMAS directions. The observed four-fold symmetry of the curve reflects the cubic symmetry of the CMAS structure.

By fitting the BLS frequencies in Figs. 2b as well as angular dependencies of DE mode frequencies with a theoretical model described in Ref. [3], we determined the numerical values of the saturation magnetization $4\pi M_s$, the exchange constant $A$ and the cubic anisotropy constant $K_1$ for the $Co_2MnAl_xSi_{1-x}$ Heusler compound with varying Al content $x$. The results are summarized in Fig. 4. The values of the saturation magnetization $4\pi M_s$ decrease when $x$ is changed from 0 to 1.0 (Fig. 4a). Moreover, at $x = 0.2$, we observe a dip-like dependence of $4\pi M_s$ on the Al content

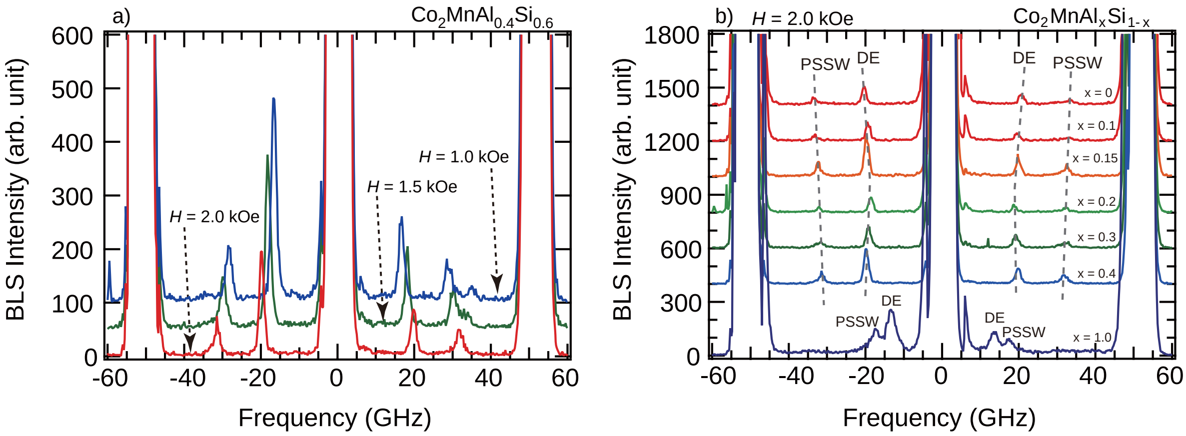

Fig. 2: a) Brillouin light scattering (BLS) spectra for $Co_2MnAl_{0.4}Si_{0.6}$ as a function of the external magnetic field. Two peaks corresponding to the excitation of spin waves are clearly visible. b) BLS spectra for CMAS with varying nominal Al composition $x$ measured at $H = 2.0\,\mathrm{kOe}$. Both DE and PSSW peaks shift upon the variation of the CMAS film composition.

which corresponds to the dependencies found for the lattice constant and the FWHM of the (004) rocking curves (Figs. 1b and c). For comparison, $4\pi M_s$ values of $Co_2MnSi$ ($x = 0$) and $Co_2MnAl$ ($x = 1.0$) measured by superconducting quantum interface device (SQUID) are shown in (Fig. 4a) as well. The SQUID values are about 10% higher than the corresponding values determined by BLS spectroscopy.

The exchange constant $A$ exhibits a less complex dependence on the composition of the CMAS film as it decreases monotonically with increase $x$ (Fig. 4b). However, we observe a surprisingly large drop by a factor of 4 in the absolute values of $A$ between $Co_2MnSi$ ($x = 0$) and $Co_2MnAl$ ($x = 1.0$). Figure 4c shows the values of the cubic anisotropy constant $K_1$ as a function of the nominal Al content $x$. Like in the case of $4\pi M_s$, we find a dip in $K_1$ near $x = 0.3$ where $K_1$ is 0 within the experimental error. It is probably related to the phase separation between CMAS and $Co_2MnSi$ (or $Co_2MnAl$) as we have mentioned above in this report.

In order to study the dependence between the coercive field $H_C$ of the CMAS samples and the composition, we performed MOKE measurements using a standard MOKE setup in longitudinal geometry. The samples were investigated by s-polarized laser light with a wavelength of $\lambda = 670\,\mathrm{nm}$ and an angle of incidence of 45°. MOKE hysteresis loops were measured at different sample orientations $\alpha$ varied from 0° to 360° in steps of 1° with $\alpha$ being the angle between

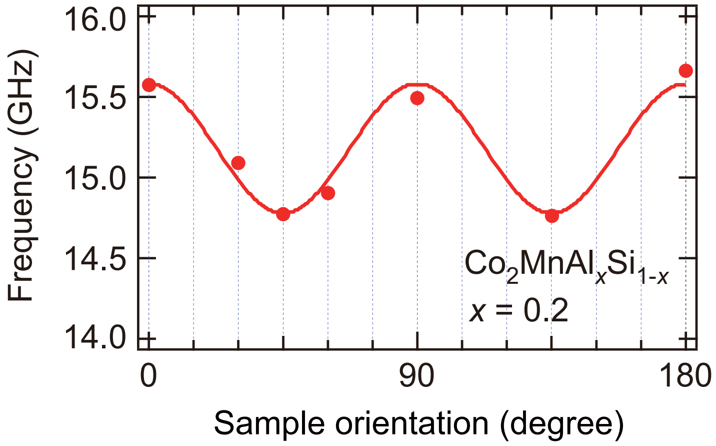

Fig. 3: Dependence of DE mode frequency on the sample orientation with respect to the external magnetic field for the CMAS film with $x = 0.2$. The sample orientation 0 corresponds to the [011] crystallographic direction of the CMAS film. The solid line is a fit to the experimental data obtained with a theoretical model described in Ref. [3]. From these measurements, the cubic anisotropy constant $K_1$ is determined.

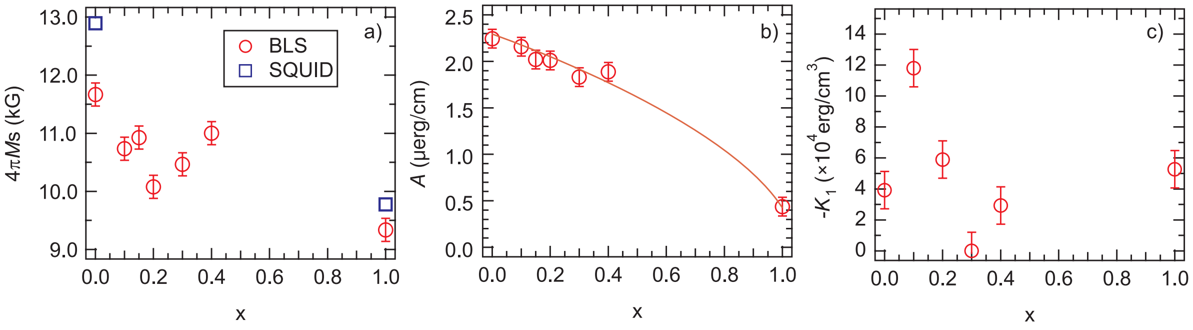

Fig. 4: Dependence of a) the saturation magnetization $4\pi M_s$, b) the exchange constant $A$ and c) the cubic anisotropy constant $K_1$ on the nominal composition $x$ of the CMAS films. In Fig. 4a, $4\pi M_s$ values measured by SQUID are shown as well for $Co_2MnSi$ ($x = 0$) and $Co_2MnAl$ ($x = 1.0$).

the in-plane [110] direction of the CMAS films and the plane of incidence. An example of the measured hysteresis loops is shown in Fig. 5 for $Co_2MnSi$ ($x = 0$) and $Co_2MnAl$ ($x = 1.0$) films for sample orientations of $\alpha = 0°$, $42°$ and $45°$. The loops are asymmetric as they consist of two additive contributions: a longitudinal MOKE contribution, which is an odd function of the external magnetic field, and a quadratic MOKE contribution, which is an even function of the external field [4].

From the MOKE loops we determined the values of $H_C$ as a function of the sample orientation $\alpha$. Figure 6 shows those dependencies for four different values of the Al content $x$. For all measured CMAS samples except $x = 0.3$ we find a clear four-fold magnetic anisotropy reflecting the cubic symmetry of the crystal structure. Sharp peaks, which appear in $H_C$ in hard axis directions, originate from a checkerboard domain pattern occuring during the hard axis magnetization reversal process [5]. The four-fold variation of $H_C$ observed for $Co_2MnSi$ persists up to the nominal Al content of 0.2; corresponding polar plots are shown only for $x = 0$ in Fig. 6a, as for $x = 0.1$

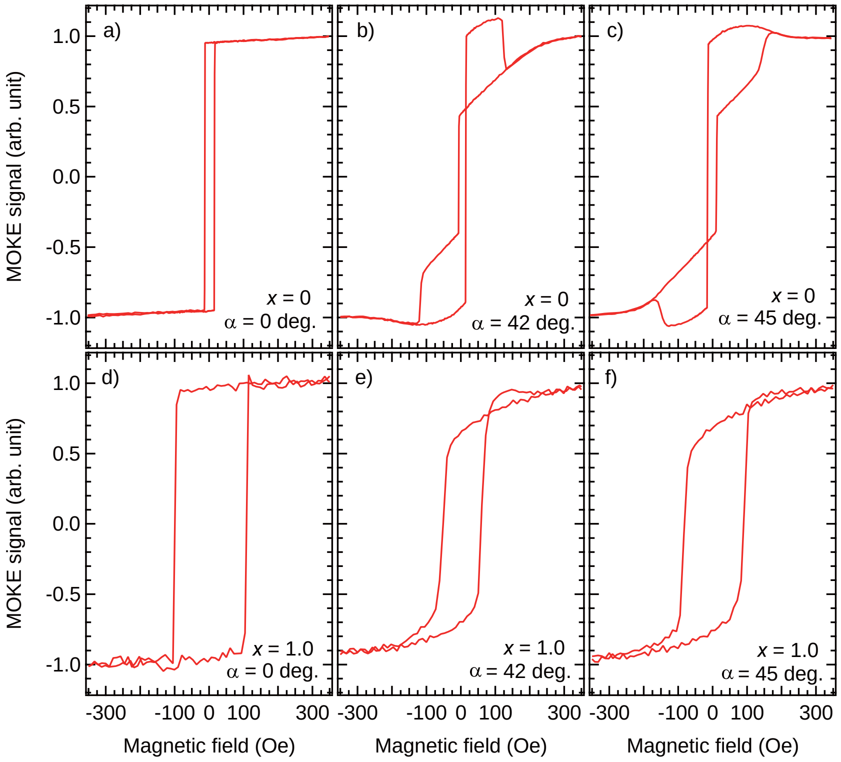

Fig. 5: Hysteresis loops measured by magneto-optical Kerr effect (MOKE) magnetometry for $Co_2MnSi$ (a–c)) and for $Co_2MnAl$ (d–f) at sample orientations $\alpha = 0°$, $42°$ and $45°$.

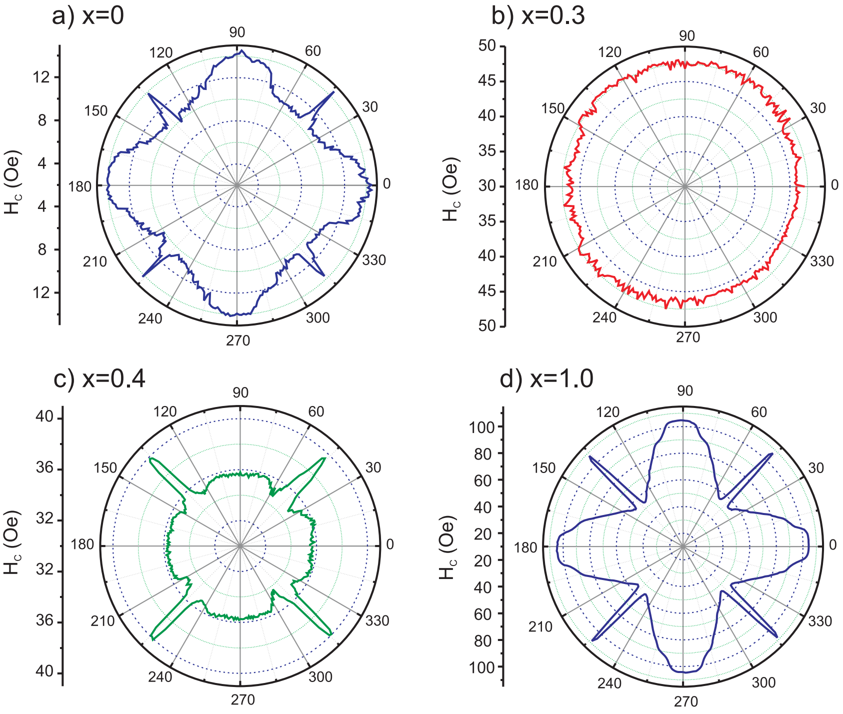

Fig. 6: Dependence of the coercive field $H_C$ on the sample orientation α for CMAS films with nominal compositions of a) $x = 0$, b) 0.3, c) 0.4 and d) 1.0. A clear four-fold symmetry of $H_C$ is observed for all samples except for the CMAS sample with $x = 0.3$. The sample orientation α is defined as the angle between the external magnetic field and the [011] crystallographic in-plane direction of the CMAS films. Note different axes limits for each plot.

and $x = 0.2$, they look very similar. However, the CMAS film with $x = 0.3$ exhibits an isotropic dependence of $H_C$ on the sample orientation α (Fig. 6b), in agreement with $K_1 = 0\,\mathrm{erg/cm^3}$ determined from the BLS measurements. The isotropic behavior of the CMAS sample with $x = 0.3$ might be related to the phase separation between CMAS and $Co_2MnSi$ (or $Co_2MnAl$) as already mentioned. For $x = 0.4$ (Fig. 6c), we again observe a four-fold anisotropy of $H_C$. Here the peaks are surprisingly very high, as for the samples studied up to now, the $H_C$ on top of the peak was about the same value as $H_C$ in easy axis direction. Finally, a $H_C$ plot for $x = 1$ is presented in Figure 6d. Here, remarkable is an unusually large difference between $H_C$ at the orientation $\alpha = 0$ (105 Oe) and $\alpha = 42°$(55 Oe).

Figure 7 summarizes the dependence of $H_C$ on the composition of the investigated CMAS films for three different sample orientations $\alpha = 0°$, 42° and 45°. The values of $H_C$ increase substantially with the increase of $x$, as, for example for $\alpha = 0$, $x = 0$, the coercivity is $H_C = 12.5\,\mathrm{Oe}$ whereas for $\alpha = 0$, $x = 1$, the coercivity is $H_C = 105\,\mathrm{Oe}$. Furthermore, the dependence of $H_C$ on $x$ exhibits a peak-like behavior near $x = 0.3$ for all three sample orientations. This peak correlates with the

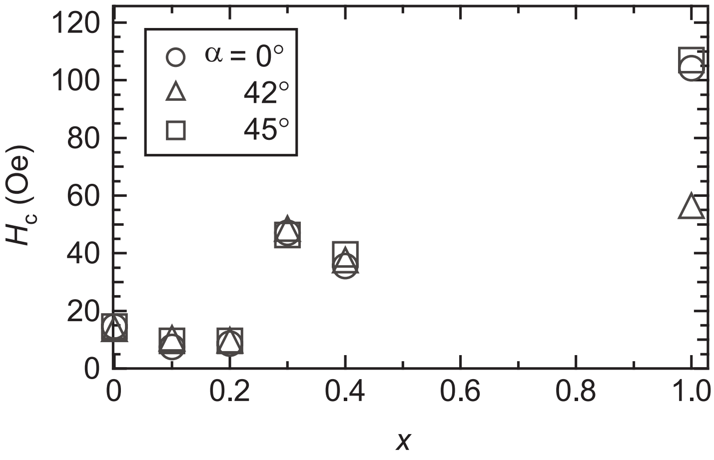

Fig. 7: Coercive field $H_C$ for CMAS films with varying nominal composition $x$ at sample orientations $\alpha = 0°$, 42° and 45°. $H_C$ increases with the increase of $x$ for all values of α. A peak near $x = 0.3$ is a fingerprint of an increased number of pinning centers at this particular film composition.

dip-like behavior found for the FWHM of the (004) rocking curves and is probably an indication of an increased number of pinning centers at this particular film composition due to the appearance of phase separation between CMAS and $Co_2$MnSi (or $Co_2$MnAl).

The project was financially supported by the NEDO International Joint Research Grant Programm 2004/T093, by the Research Unit 559 *"New materials with high spin polarization"* funded by the Deutsche Forschungsgemeinschaft and by the Stiftung Rheinland-Pfalz für Innovation.

## References

[1] I. Galanakis, P.H. Dederichs, N. Papanikolaou, Phys. Rev. B **66**, 174429 (2002).
[2] Y. Sakuraba, M. Hattori, M. Oogane, H. Kubota, Y. Ando, A. Sakuma, T. Miyazaki, J. Phys. D: Appl. Phys. **40**, 1221 (2007).
[3] B. Hillebrands, Phys. Rev. B **41**, 530 (1990).
[4] J. Hamrle, S. Blomeier, O. Gaier, B. Hillebrands, H. Schneider, G. Jakob, K. Postava, C. Felser, J. Phys. D: Appl. Phys. **40**, 1563 (2007)
[5] J. Hamrle, S. Blomeier, O. Gaier, B. Hillebrands, R. Schäfer, M. Jourdan, J. Appl. Phys. **100**, 103904 (2006).

## 6.9 Structural and magnetic properties of $Co_2FeSi$ tuned by $He^+$ irradiation

*O. Gaier, J. Hamrle, and B. Hillebrands*[1]

We report on the dependence of structural and magnetic properties on irradiation with 30 keV $He^+$ ions in thin films consisting of a $L2_1$ ordered $Co_2FeSi$ Heusler compound. Being a half-metallic ferromagnet with the highest Curie temperature among the Heusler compounds, $Co_2FeSi$ is considered to be one of the most promising materials for spintronic applications. However, theoretical calculations suggest that the spin polarisation in this alloy (like in $Co_2MnSi$ on which we reported in the previous Section) is very sensitive to the degree of $L2_1$ order [1, 2]. Usually, the transition from the disordered to the $L2_1$ ordered phase in $Co_2FeSi$ is achieved by an annealing step after film deposition. This procedure, however, is not suitable if local modifications of crystallographic properties are required. In such a case irradiation with keV ions might be a convenient tool as reported for FePd(Pt) films [3].

The $Co_2FeSi$ films of 38 nm thickness investigated within the framework of this project were epitaxially grown on MgO(100) substrates at the Johannes-Gutenberg-Universität, Mainz by means of RF magnetron sputtering. Details of the sample preparation can be found in Ref. [4]. The $L2_1$ structure of the deposited films was confirmed by X-ray diffraction (XRD) measurements, which were also carried out in Mainz using Cu-$K_\alpha$ radiation. The subsequent irradiation of the $Co_2FeSi$ films with 30 keV $He^+$ ions was performed in close collaboration with the Forschungszentrum Dresden-Rossendorf where fluences of $1 \cdot 10^{14}$, $5 \cdot 10^{14}$, $1 \cdot 10^{15}$, $5 \cdot 10^{14}$ and $1 \cdot 10^{16}$ ions/cm$^2$ were applied. In the following, we first report on the dependence of the structural properties of the $Co_2FeSi$ films on the irradiation with $He^+$ ions and then discuss the modification of their magnetic properties induced by the ion bombardment.

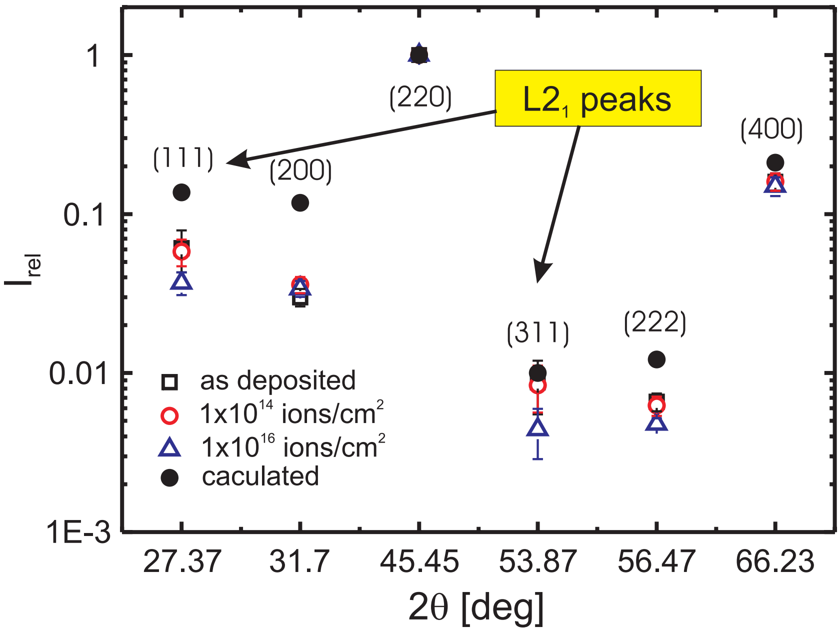

Fig. 1: Intensities of the X-ray diffraction peaks normalized by the intensity of the (220) fundamental reflection for the unirradiated $Co_2FeSi$ sample (□) and for the samples with the smallest (•) and highest (△) fluences applied. Full circles represent the peak intensities obtained from powder pattern simulations.

---

[1] In collaboration with H. Schneider, G. Jakob, Johannes-Gutenberg-Universität, Mainz and J. Fassbender, Forschungszentrum Dresden-Rossendorf, Dresden.

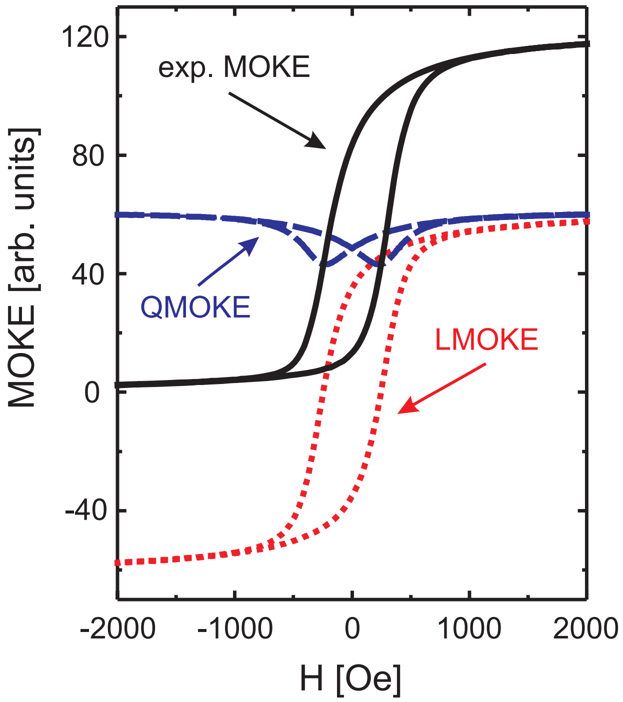

Fig. 2: Hysteresis curve for the $Co_2FeSi$ film irradiated at a fluence of $1 \cdot 10^{14}$ ions/cm$^2$ of 30 keV $He^+$ ions measured at $\alpha = 22°$ (solid line) as well as LMOKE (dotted line) and QMOKE (dashed line) contributions determined from symmetrization and antisymmetrization of the experimental MOKE loop.

The influence of the $He^+$ ion irradiation on the structural properties of the $Co_2FeSi$ films is summarized in Fig. 1. The Figure exhibits the normalized intensities of the peaks observed in the XRD measurements for the nonirradiated sample and for the samples with the smallest and highest fluences applied. For comparison, the corresponding intensities obtained from powder pattern simulations are also presented in Fig. 1. At a small fluence of $1 \cdot 10^{14}$ ions/cm$^2$ the intensities of the (111) and (311) reflections, which are characteristic for the $L2_1$ phase, remain nearly unchanged with respect to the corresponding values of the as prepared sample. However, the intensities of these peaks remarkably decrease when a dose of $1 \cdot 10^{16}$ ions/cm$^2$ is applied. These results indicate that in the low fluence range the $L2_1$ order of the $Co_2FeSi$ films is preserved after the ion bombardment while it is reduced for higher fluences. From a more detailed analysis of the characteristic diffraction peaks using Eq. (1) in the previous section 6.7, an $L2_1$ ordering degree of 80 % and 60 % could be estimated in the as deposited sample and in the sample exposed to a fluence of $1 \cdot 10^{16}$ ions/cm$^2$, respectively. An icreasing of the ion fluence by the order of two correlates with a reduction of the $L2_1$ order by approximately 20 % in the investigated $Co_2FeSi$ samples.

In order to investigate the influence of 30 keV $He^+$ irradiation on magnetic and magneto-optical properties of the $Co_2FeSi$ films a standard magneto-optical Kerr effect (MOKE) set-up in the longitudinal geometry was used. The hysteresis loops of all investigated $Co_2FeSi$ films acquired from MOKE measurements reveal an asymmetric shape [5]. For example, Fig. 2 shows the hysteresis curve obtained at a sample orientation of $\alpha = 22°$ from the $Co_2FeSi$ film irradiated with $He^+$ ions at a fluence of $1 \cdot 10^{14}$ ions/cm$^2$. The observed asymmetry originates from a superposition of two MOKE contributions: the longitudinal MOKE (LMOKE) signal, which is odd in $H$ and the quadratic MOKE (QMOKE), which is even in $H$. By symmetrization and antisymmetrization of experimental loops it is possible to separate LMOKE and QMOKE contributions [5].

The LMOKE loops were used for the determination of the coercive field $H_C$ of the investigated $Co_2FeSi$ films. For example, Fig. 3a shows the dependence of $H_C$ on the sample orientation with respect to the direction of the applied magnetic field for the $Co_2FeSi$ sample irradiated at a fluence of $5 \cdot 10^{15}$ ions/cm$^2$. In this figure a constant character of the coercivity is clearly visible which

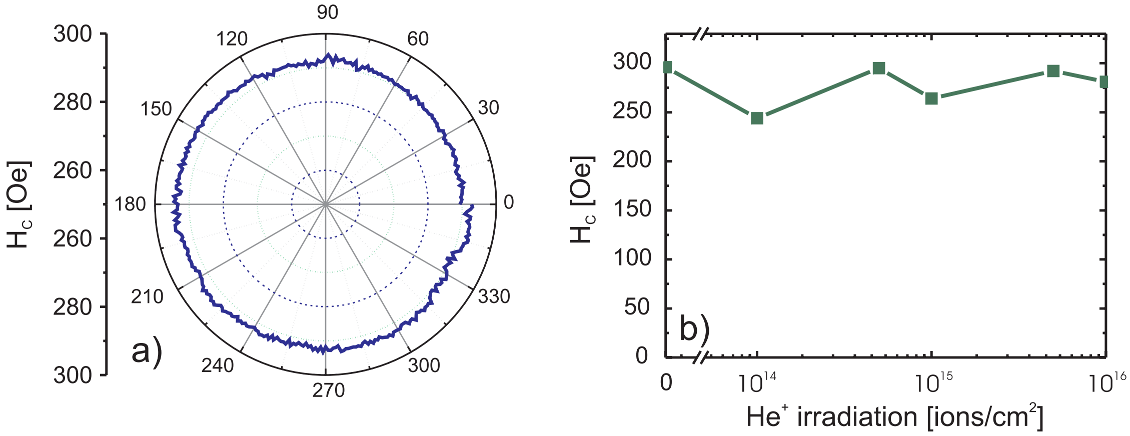

Fig. 3: a) Dependence of $H_C$ on sample orientation α for the $Co_2FeSi$ film irradiated with $He^+$ ions at a fluence of $5 \cdot 10^{14}$ ions/cm$^2$. b) Dependence of $H_C$ on the applied $He^+$ ion dose.

is surprising for an $L2_1$ ordered epitaxial structure having a cubic symmetry. Furthermore, the constant dependence between $H_C$ and the sample orientation is preserved after the irradiation with $He^+$ ions (the corresponding rotational scans are not shown here). The reasons for this isotropic behavior are not well understood and require further investigations. A comparison of $H_C$ values for $Co_2FeSi$ films exposed to different fluences makes evident that the coercivity remains nearly unchanged upon the ion irradiation (Fig. 3b).

Figure 4 shows the dependence of the LMOKE and the QMOKE amplitude on $He^+$ irradiation. In the case of the LMOKE signal, its value is approximately 58 mdeg for all the applied fluences. As LMOKE originates from first order spin-orbit (SO) coupling [5], we may conclude, together with the structural investigations desribed above, that the remarkable reductions of the $L2_1$ order in $Co_2FeSi$ does not reduce the spin-orbit (SO) coupling of the first order. The QMOKE, however, exhibits a completely different behavior upon irradiation with $He^+$ ions (Fig. 4). An increase of the ion fluence up to $1 \cdot 10^{16}$ ions/cm$^2$ leads to a reduction of the detected QMOKE amplitude by a factor of 2. As QMOKE originates from SO coupling of the second order, these results suggest that in $Co_2FeSi$ films the SO coupling of the second order is much more sensitive to the degree of the $L2_1$ order than the first order SO coupling. However, a strong QMOKE contribution in

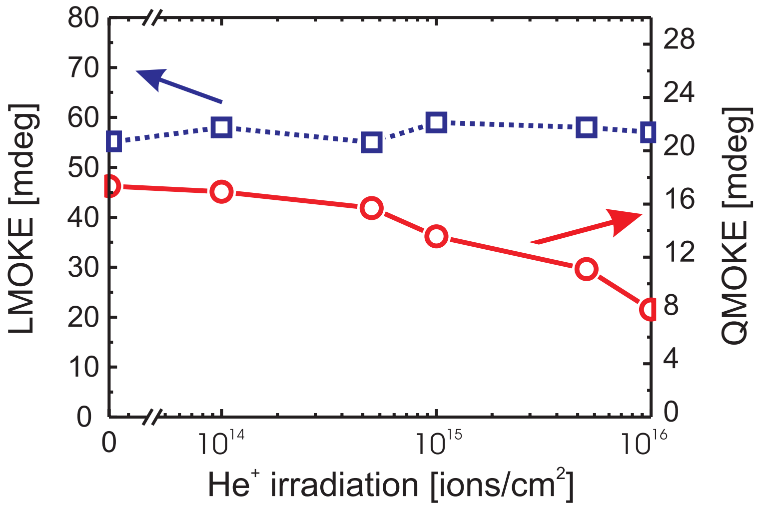

Fig. 4: LMOKE and QMOKE signal as a function of the applied fluence of the 30 keV $He^+$ ions.

the investigated $Co_2FeSi$ samples might also be indirectly caused by magnetostriction. Therefore, the observed reduction of the QMOKE signal might be indicative for the releasing of strain in the crystal lattice after the $He^+$ ion irradiation.

The project was financially supported by the Research Unit 559 *“New materials with high spin polarization”* funded by the Deutsche Forschungsgemeinschaft, by the NEDO International Joint Research Grant Programm 2004/T093 and by the Stiftung Rheinland-Pfalz für Innovation.

## References

[1] S. Picozzi, A. Continenza, A.J. Freeman, Phys. Rev. B **69**, 094423 (2004).
[2] Z. Gercsi, K. Hono, J. Phys.: Condens. Matter **19**, 326216 (2007).
[3] H. Bernas, J.-Ph. Attané, K.-H. Heinig, D. Halley, D. Ravelosona, A. Marty, P. Auric, C. Chappert, Y. Samson, Phys. Rev. Lett. **91**, 0772031 (2003).
[4] H. Schneider, G. Jakob, M. Kallmayer, H.J. Elmers, M. Cinchetti, B. Balke, C. Felser, M. Aeschlimann, H. Adrian, Phys. Rev. B **74**, 174426 (2006).
[5] J. Hamrle, S. Blomeier, O. Gaier, B. Hillebrands, H. Schneider, G. Jakob, K. Postava, C. Felser, J. Phys. D: Appl. Phys. **40**, 1563 (2007).

# C. Patterned Magnetic Structures

## 6.10 Field dependence of quantized spin waves in nano-scaled magnetic ring structures

*H. Schultheiss, S. Schäfer, P. Candeloro, B. Leven, and B. Hillebrands*

Small magnetic ring structures have attracted great interest in the last five years concerning their static and dynamic properties [1–4]. Rings exhibit a richness of possible domain patterns depending on their diameter and width. The probably most famous ones are the so called vortex state and the onion state. In the vortex state the magnetization is aligned along the ring and a flux closure state is formed. Therefore no magnetic stray fields are present. This fact makes ring structures an attractive candidate for high density magnetic random access memory devices since the dipolar interaction between neighboring storage cells is minimized.

Here we report on microfocus Brillouin light scattering spectroscopy [5] on a single magnetic ring structure. The magnetization reversal of a single ring during a magnetic field loop is studied using spin waves as a probe for the local magnetization configuration. Furthermore we investigate the influence of an externally applied field on the spin dynamics of the vortex state when the rotational symmetry is broken, and we compare the experimental results with dynamic micromagnetic simulations.

The magnetization configurations of the vortex and onion state for a ring with diameter 2 μm and width 400 nm are calculated with OOMMF [6]. The corresponding equilibrium states are shown in Fig. 1. For preparing the onion state an external magnetic field of 400 Oe is applied. The material is $Ni_{81}Fe_{19}$ with a thickness of 15 nm. Both magnetization configurations are remanent, i.e., for preparing the vortex state a minor loop has to be performed.

The structures were prepared by electron beam lithography and lift-off technique. The $Ni_{81}Fe_{19}$ film with a thickness of $t = 15$ nm was grown by e-beam deposition in an ultra high vacuum system.

We now discuss the dynamic properties of those ring structures, focussing on the field dependence of the dynamics in the vortex state as well as the transition between the vortex and the onion state.

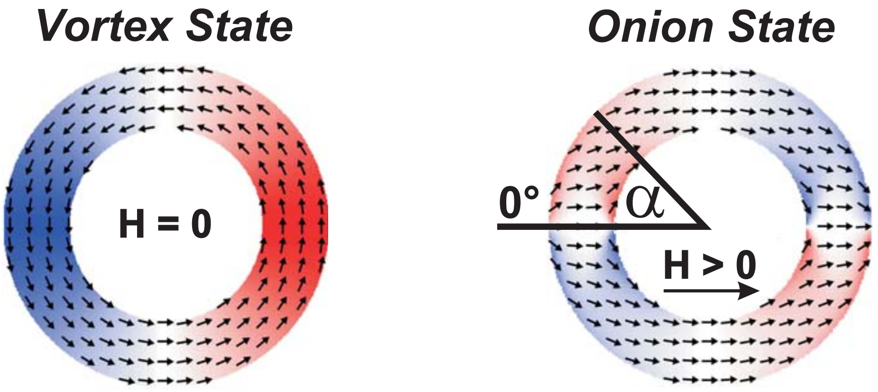

Fig. 1: (Color online) Magnetization configurations for ferromagnetic ring structures. Shown is the so-called vortex state at remanence with a flux closure alignment of the magnetic moments and a rotational symmetry and the so-called onion state where the rotational symmetry is broken due to an inplane magnetic field of 400 Oe. The angle α defines the azimuthal position on the ring structure. As the starting point of α the pole region of the onion state was chosen.

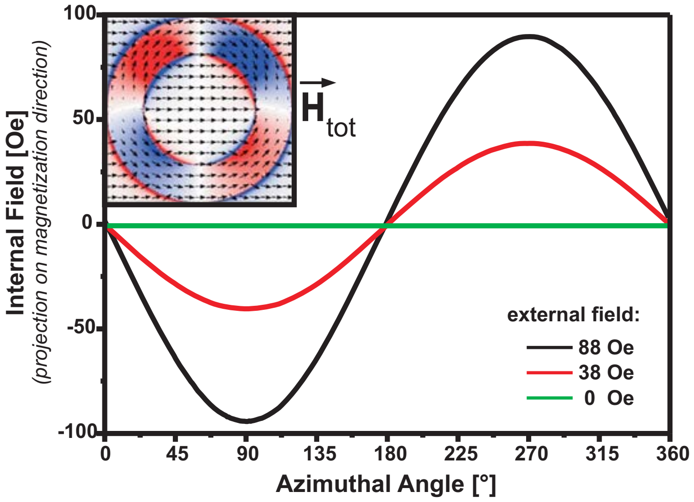

Fig. 2: (Color online) The OOMMF code was used to calculate the internal magnetic field distribution of a ring magnetized in the vortex state for different externally applied fields. The inset shows the 2D distribution of the internal magnetic field, in the line-graphs the value of the projection of the internal field onto the local magnetization vector is shown. Negative values of the internal magnetic field correspond to an anti-parallel alignment to the magnetization.

The equatorial regions at $\alpha = 90^\circ$ and $270^\circ$ (see Fig. 1 for the definition of $\alpha$) are well suited for studying the spin dynamics as a function of an externally applied field because of the either parallel or anti-parallel alignment of the magnetization and the externally applied magnetic field. For the following discussion we define $\alpha = 90^\circ$ as position 1 and $\alpha = 270^\circ$ as position 2. In the onion state both positions are equivalent since the magnetization is pointing in the same direction and parallel to the externally applied field. However, in the vortex state the magnetization is now pointing anti-parallel to the externally applied magnetic field either at position 1 or at position 2 depending on the chirality of the vortex state. As can be seen in Fig. 2 the magnetization is not only anti-parallel to the external magnetic field but also anti-parallel to the total internal magnetic field. Hence, a strong difference of the spin-wave frequencies at position 1 and 2 is expected for the vortex state when the rotational symmetry is broken due to an externally applied field. A magnetic field of $-1500\,\mathrm{Oe}$ was applied along the horizontal direction as shown in Fig. 1 in order to saturate the ring structure and to define a clear magnetic history. A field cycle is started at $-200\,\mathrm{Oe}$ and the field is increased to $200\,\mathrm{Oe}$ before decreasing it again to the initial value. For each magnetic field a BLS-spectra was acquired at position 1 and position 2. Figure 3a displays the measured BLS-spectra in a grayscale code (color online) for all field values alway alternating between position 1 and 2.

The measured spin-wave spectra as a function of the externally applied magnetic field at position 1 and 2 are shown in Fig. 3. In the first part of the magnetic field cycle between $-200\,\mathrm{Oe}$ and $80\,\mathrm{Oe}$ a clear resonance is observed with decreasing frequency. When the field is increased above $80\,\mathrm{Oe}$ a mode splitting of the spin-wave frequency is observed. One mode is still following the decrease in frequency whereas another mode appears and is increasing in frequency. When comparing Fig. 3c and 3d, where the BLS-spectra are displayed separately for position 1 and 2, it is clear, that the decrease of the spin wave frequency is occuring when the magnetization is aligned anti-parallel to the externally applied field and the frequency is increasing when the magnetization is parallel to the applied magnetic field. As soon as the externally applied field exceeds $100\,\mathrm{Oe}$ the magnetization configuration is switching to the reversed onion state and the frequencies are merging to a single resonance again. In the second half of the field cycle the reversed process can be observed but now for a different switching field, indicating that the switching field distribution of a ring structure is wide spread. A closer look to Fig. 3c and d shows that on the second part of the field cycle the chirality of the vortex state was inverted.

For studying the spin dynamics in the vortex state of a magnetic ring structure with an applied field the flux closure magnetization distribution has to be prepared in a minor loop since also the onion

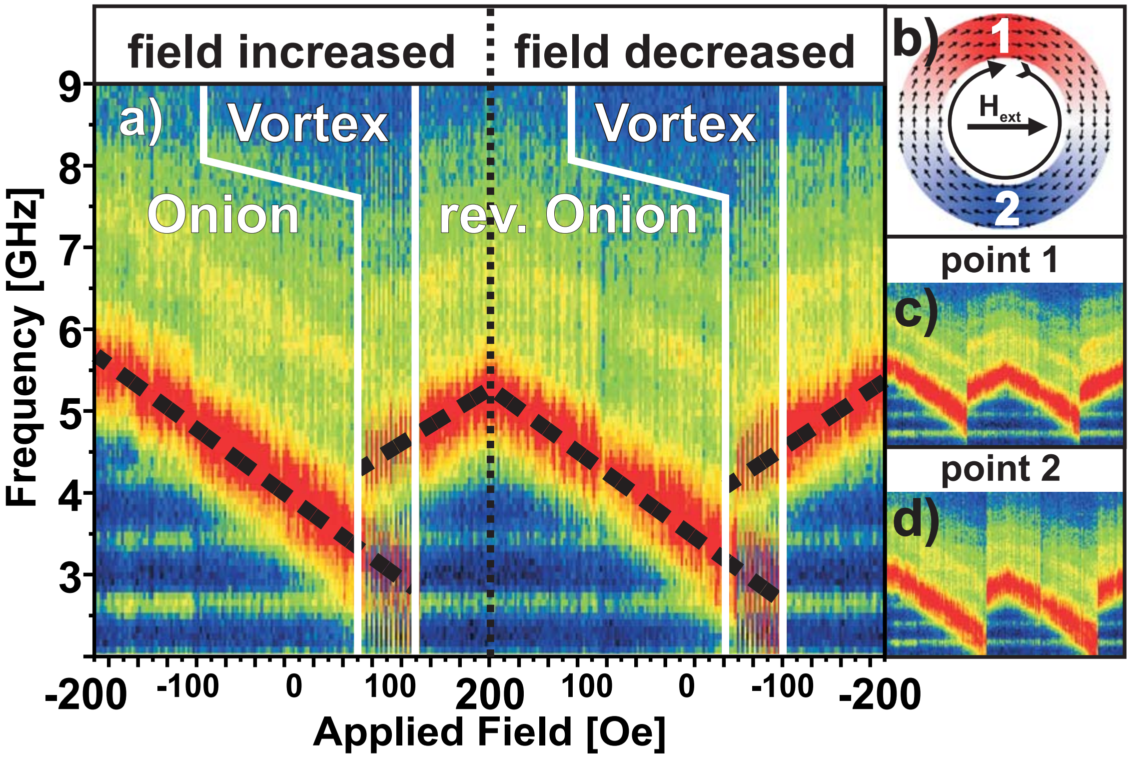

Fig. 3: (Color online) Field dependence of spin-waves in a ring with 2 µm diameter and 400 nm width measured at $\alpha = 90^\circ$ and $270^\circ$, called position 1 and 2. a) For each field value the BLS spectra measured at position 1 and 2 are shown together in order to demonstrate the splitting of the spin-wave frequencies when the ring is switching from the onion state to the vortex state. The bold dashed lines are guide to the eye for the main resonance, i.e. the first standing spin wave across the ring width. b) Definition of point 1 and 2 in the equatorial regions of the ring structure. c) and d) Data for position 1 and 2 are displayed separately to check the relative alignment of the magnetization in respect to the direction of the externally applied field. The chirality of the vortex state can be extracted out of this data.

state can exist at remanence. The corresponding field scan is shown in Fig. 4a. The sample was saturated at −1500 Oe before sweeping the external magnetic field. This time the field direction was reversed before the reversed onion state was achieved. At a field of 0 Oe the mode frequencies of positions 1 and 2 coincide again and the vortex state at remanence is prepared. For three different values of the externally applied field spatially resolved measurements are performed. The laser spot is placed at the middle of the ring structure and scanned as a function of the azimuthal angle $\alpha$. The results for 0 Oe, 38 Oe and 88 Oe are shown in Fig. 5. For the spatially resolved scan at 0 Oe the measured spin wave frequencies are constant except for a narrow region around the pole position at $180^\circ$. The constant frequency lines are interrupted and new modes with different frequencies are arising. Micro-magnetic simulations show that in the process of the magnetization reversal a $360^\circ$ domain wall can be created in the pole region of a ring structure, and the modes with frequencies of 2.5 GHz, 4.5 GHz and 6.6 GHz are the spin-wave excitations within this domain wall. This is also supported by the fact, that these frequencies are measured only at one pole of the ring structure where both $180^\circ$ domain walls of the onion state meet after the magnetization reversal process.

When the rotational symmetry of the vortex state is broken due to an externally applied field the observed spin-wave mode profiles show characteristic changes. In the part of the ring structure where the magnetization is parallel to the applied magnetic field, the spin wave frequencies are increasing. For an anti-parallel alignment of magnetization and external field, where also the total

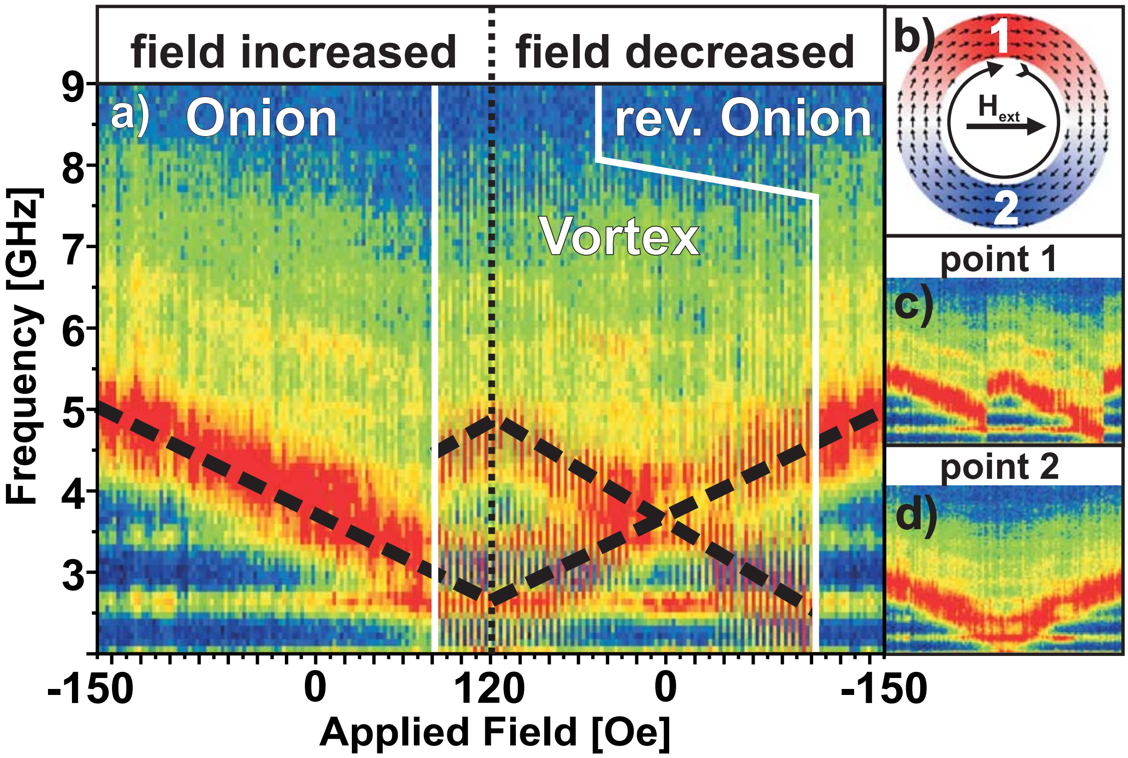

Fig. 4: (Color online) Shown is the field dependence of spin waves quantized over the width of a ring structure when a minor loop is driven. The existence of the vortex state at remanence can be seen when the previously splitted modes are merging again in frequency.

internal field is anti-parallel to the magnetization as shown in Fig. 2, the spin wave frequencies are decreasing and follow the distribution of the total internal field. All the spatial developments of the spin wave frequencies described above are also true for the higher spin-wave modes quantized in radial direction. Note that the observed spin-waves are not constant anymore as a function of position when the symmetry of the vortex state ist broken. This continous development of the spin-wave frequencies as a function of the azimuthal angle α is in agreement with the recently reported partial decoherence of thermally excited spin waves indicating that the coherence length of the spin waves does not allow a coherent propagation about the entire ring. The measured spin wave frequency adapts to the average value of the internal field it senses during its lifetime. A creation

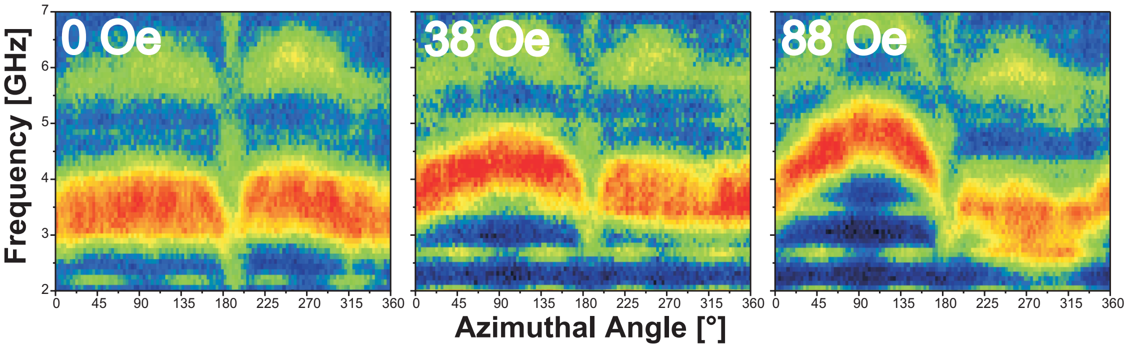

Fig. 5: (Color online) Spatially resolved BLS measurements along a path in the middle of a ring structure. Space coordinate is the azimuthal angle α as defined in Fig. 1. The BLS scans were taken for three different externally applied magnetic fields: 0 Oe, 38 Oe and 88 Oe. In the pole position at 180° a disturbation of the spin-wave frequencies is visible due to the presence of a 360° domain wall.

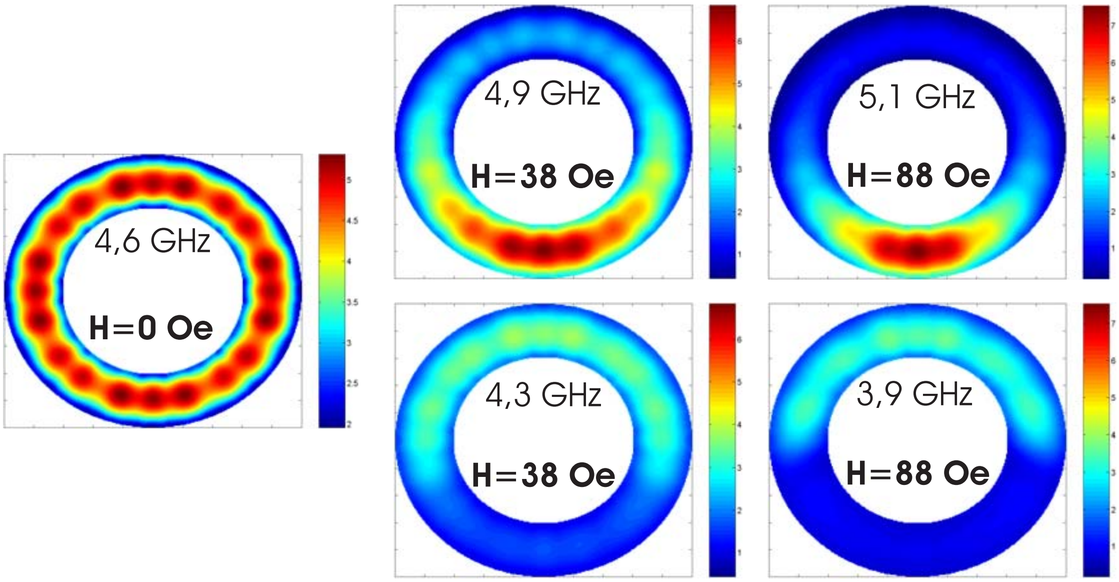

Fig. 6: (Color online) Dynamic micro-magnetic simulation for a vortex state with different static magnetic fields oriented in the sample plane. For 38 Oe and 88 Oe the spatial profile of the splitted modes are shown.

of a global eigenmode system over the ring structure is not possible and therefore a quantization in azimuthal direction cannot be observed. However, the coherence length of the spin waves is still sufficient for creating standing spin waves in radial direction.

The experimental results are in excellent agreement with micromagnetic simulations. In Fig. 6 the results of dynamic micro-magnetic simulations carried out with the free OOMMF code are displayed. For the investigated magnetic fields the equilibrium state was calculated before applying a short magnetic field pulse out of plane perpendicular to the direction of the static field. The duration of the field pulse is 1 ps and the amplitude is 1 Oe, small enough to ensure only small angle precessions in order to avoid nonlinear effects. After the excitation pulse, the time dependent behavior of the magnetization was stored for every point of the mesh and afterwards Fourier transformed pointwise. A subsequent convolution of the resulting spin-wave intensity with a Gaussian function representing the probing laser pulse allowed for a even better approximation of the experimentally observed local distribution of spin-wave intensities. The shift of the spin-wave frequencies to higher and lower frequencies in regions with parallel and anti-parallel alignment of magnetization and internal field, correspondingly, are well reproduced supporting the experimentally observed resonances.

In conclusion we investigated the field dependence of spin waves in a nano-scaled magnetic ring structure. The switching from onion to vortex state and reversed onion state during the magnetization reversal could be observed by the means of micro-focus Brillouin light scattering spectroscopy in a single magnetic field loop. The effect of broken symmetry on the spin waves in the flux closure vortex state was investigated and it could be shown that the spin-wave frequencies are locally changing corresponding to the distribution of the total internal field. We showed that micro-focus BLS enables the determination of the chirality of the vortex state of a single nano-scaled ring structure and in addition the excitation spectrum of a 360° domain wall was studied.

Support by the Priority Program SPP 1133 of the Deutsche Forschungsgemeinschaft and the NEDO International Joint Research Program 2004IT093, Japan, is gratefully acknowledged. The authors acknowledge S. Trellenkamp and S. Wolff from the Nano + Bio Center, University of Technology Kaiserslautern, for technical support.

## References

[1] I. Neudecker, M. Kläui, K. Perzlmaier, D. Backes, L.J. Heyderman, C.A.F. Vaz, J.A.C. Bland, U. Rüdiger, C.H. Back, Phys. Rev. Lett. **96**, 057207 (2006).

[2] G. Gubbiotti, M. Madami, S. Tacchi, G. Carlotti, H. Tanigawa, T. Ono, L. Giovannini, F. Montoncello, F. Nizzoli, Phys. Rev. Lett. **97**, 247203 (2006).

[3] M. Buess, R. Hüllinger, T. Haug, K. Perzlmaier, U. Krey, D. Pescia, M.R. Scheinfein, D. Weiss, C.H. Back, Phys. Rev. Lett. **93**, 077207 (2004).

[4] H. Schultheiss, S. Schäfer, P. Candeloro, B. Leven, B. Hillebrands, A.N. Slavin, submitted to Phys. Rev. Lett..

[5] V.E. Demidov, S.O. Demokritov, B. Hillebrands, M. Laufenberg, P.P. Freitas, Appl. Phys. Lett. **85**, 2866 (2004).

[6] M.J. Donahue, D.G. Porter, Report NISTIR 6376, National Institute of Standards and Technology, Gaithersburg, MD(1999).

[7] J. Jorzick, S.O. Demokritov, B. Hillebrands, M. Bailleul, C. Fermon, K.Y. Guslienko, A.N. Slavin, D.V. Berkov, N.L. Gorn, Phys. Rev. Lett. **88**, 047204 (2002).

## 6.11 Domain wall design in semi-circular $Ni_{81}Fe_{19}$ structures

*C. Sandweg, S.J. Hermsdörfer, H. Schultheiss, P.A. Beck, B. Leven, and B. Hillebrands*[1]

Domain walls in small ferromagnetic elements have recently attracted much experimental and theoretical interest due to their application potential in magnetic logic [1] and data storage [2] as well as for their fundamental physical properties [3]. Domain walls interact with electric currents and magnetic fields and their manipulation is of specific interest for the development of new 'domain wall' magnetoelectronics. A complementary approach is to study the interaction between domain walls and spin waves. We are particularly interested in how one can manipulate a domain wall by impinging spin waves and spin-wave pulses and vice versa. We employ Brillouin light scattering microscopy, which is a method providing the requested frequency and spatial resolution. First results are presented in Section 6.12. However, when using this method for spin wave characterization, a reliable domain wall injection method is required. Thus, a detailed study of the domain wall characteristics in $Ni_{81}Fe_{19}$ wires is necessary. We employ a wire design similar to the recently introduced domain wall pendulum, working equivalently to a gravitational pendulum, which provides information on the effective mass of a domain wall [4, 5]. For the present investigations it is not sufficient to know the existence and position of the domain wall, but also the domain wall microstructure needs to be characterized in detail, as numerous different domain wall types have been identified in $Ni_{81}Fe_{19}$ wires in the micro- and sub-micrometer regime. In particular, transverse domain walls, asymmetric transverse domain walls and vortex domain walls have been the subject of experimental and theoretical studies [6, 7]. Moreover, for wires with geometries close to the phase boundaries of different wall types, transformation during the course of an experiment is not unusual [8]. Hence observation to follow variations in the structure of a domain wall is frequently necessary.

Characterization of magnetic domains and the nature of the walls between them can be performed using various techniques including magneto-optical Kerr microscopy, magnetic force microscopy, X-ray magnetic circular dichroism and Lorentz microscopy [9]. Here, we report on Lorentz microscopy investigations of domain wall formation and manipulation in curved permalloy wires containing single anti-notches or protuberances. Experimental results are compared with results obtained using micromagnetic simulations. The reason for fabricating notches or anti-notches in magnetic wires is primarily to provide artificial domain wall pinning sites to define the exact position of the domain wall. For various applications it is important to know the precise localization of the domain wall and how the geometry of the notch affects the pinning potential. The latter quantity depends not only on the notch itself but also on the domain wall structure. For this reason we have also investigated the domain wall structure as a function of applied field until it is unpinned of the anti-notch, leaving the magnetization on both sides aligned.

The samples were produced using a combination of electron beam lithography and molecular beam epitaxy. The required wire pattern was written in 120 nm thick PMMA (950K 4%) spun onto $Si_3N_4$ 'window' substrates of the kind used extensively in transmission electron microscopy (TEM) [10], which provides electron transparency in the 'window' region. The wires to be studied were fabricated on top of 100 µm square regions of 50 nm thick unsupported $Si_3N_4$. After deposition of 10 nm of $Ni_{81}Fe_{19}$ lift-off of the PMMA in acetone left the desired pattern of wires.

---

[1] In collaboration with N. Wiese, D. McGrouther, S. McVitie and J. Chapman, Department of Physics and Astronomy, University of Glasgow, UK, and B. Lägel, C. Dautermann, and S. Wolff, Nano+Bio Center, TU Kaiserslautern, Germany.

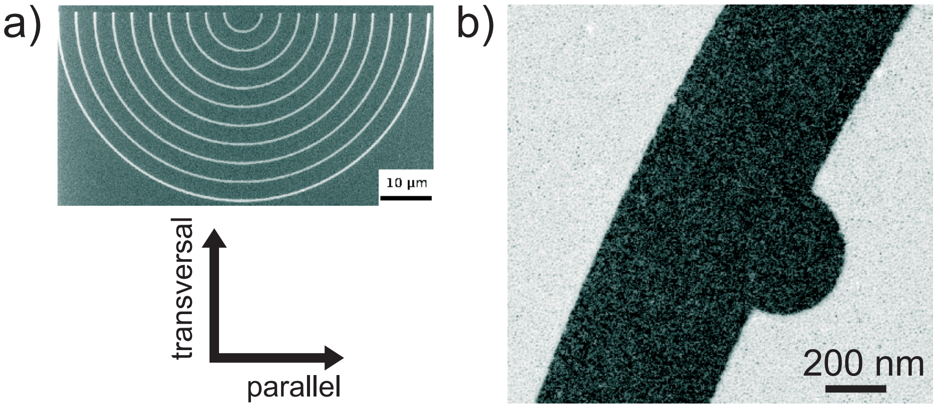

Fig. 1: a) SEM image of the fabricated $Ni_{81}Fe_{19}$ wires, b) low-magnification bright field TEM image showing an anti-notch.

Figure 1a shows a scanning electron microscopy image of the sample. It comprises 500 nm wide semi-circular wires with radii varying in steps of 5 µm from 5 µm to 50 µm. The anti-notch is semicircular in shape with a radius of 250 nm and is located midway along the wire. Such geometries are attractive since domain walls can be easily created and subsequently moved by external magnetic fields [5]. A domain wall can be created by letting the magnetization distribution relax following the application of a large field parallel to the symmetry axis (trasversal direction, see Fig. 1a). To move the domain wall along the wire an orthogonal field (parallel direction) needs to be applied. A low magnification bright field TEM image, Fig. 1b), shows that the wire is very well defined and also provides detail of the anti-notch.

To determine the detailed form of the domain walls generated, the differential phase contrast (DPC) mode of Lorentz microscopy was used [11]. The transmission electron microscope (TEM) was a modified Philips CM20 equipped with (non-immersion) Lorentz lenses, thereby allowing magnetic imaging in a field-free environment with the standard objective lens switched off [12]. In the experiments conducted here, the objective lens was weakly excited to provide a magnetic field suitable for moving the domain wall. Control of the field to which the wires were subjected was achieved by tilting the TEM holder, thereby subjecting the specimen to a component of field in the plane of the wires. In the DPC imaging mode, pairs of images sensitive to orthogonal components of induction perpendicular to the electron trajectory are formed. The images are derived from the currents falling on opposite sectors of a quadrant detector and, as all information is recorded simultaneously, are in perfect registration. Analysis of the image pairs then yields a quantitative vector map of averaged induction, vividly showing the detailed magnetic structure of the domain walls under investigation. The resolution of the resulting map is determined principally by the $\approx 25\,\mathrm{nm}$ probe diameter.

The results obtained by Lorentz microscopy imaging were compared to micromagnetic simulations using OOMMF [13]. Parameters used were standard for $Ni_{81}Fe_{19}$ ($M_s = 860\,\mathrm{emu/cm^3}$, $A = 1.3 \cdot 10^{-6}\,\mathrm{erg/cm}$ and $K = 0$) and the cell size was $5\,\mathrm{nm} \times 5\,\mathrm{nm} \times 10\,\mathrm{nm}$. The chosen cell dimensions in the plane of the film are comparable with the material exchange length, and the out-of-plane cell dimension was set equal to the film thickness. Figures 2a, 2b and 2c show the $B_x$ and $B_y$ components of induction and the calculated vector induction distribution displayed as a gray scale map,respectively. The domain wall itself was formed after a field of $\approx 3500\,\mathrm{Oe}$ was applied parallel to the transversal direction and then reduced to zero. The wire used was the one with the smallest radius of curvature.

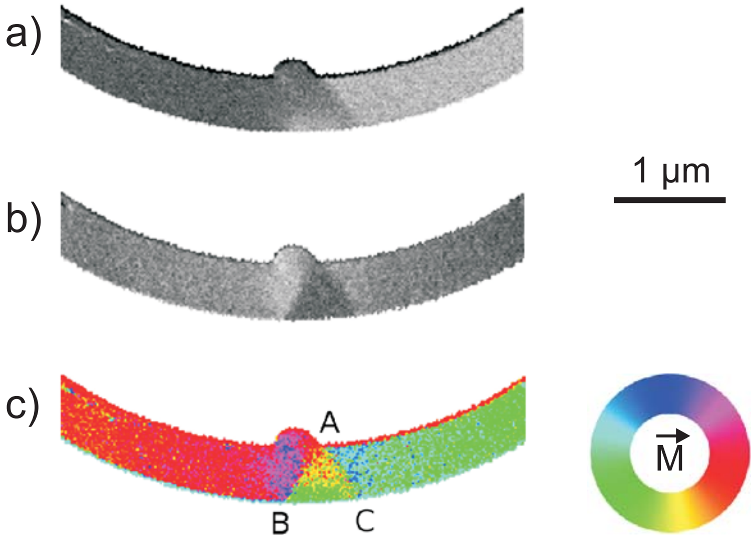

Fig. 2: Remanent states of the curved wire with radius $r = 5\,\mu\mathrm{m}$ after saturation in a field parallel to the transversal axis. a) and b), DPC images of the parallel and transversal components of magnetic induction, and c), gray scale induction map deduced from a) and b).

In Fig. 3 the equivalent micromagnetic simulation is displayed. Both the experiment and the simulation identify a domain wall of the head-to-head type. The apex of the wall appears to be pinned close to the right-hand side of the anti-notch (at A), while below the anti-notch a complex induction distribution exists. Thus the domain wall formed in the $Ni_{81}Fe_{19}$ wire should be thought of as a domain wall packet [14]. In can be seen that the dimension of this domain wall extends farther than the anti-notch diameter at the lower edge of the wire. The overall geometry is essentially that of an asymmetric transverse domain wall which can be represented schematically by two domain walls of unequal length as shown in the scheme in Fig. 3. Here, the principal difference from a standard asymmetric transverse domain wall is caused by the shape as well as the asymmetry of the anti-notch itself, in which there is inevitably some circulation of flux. Despite this, as seen from the arrows in Fig. 3, the circulation is never complete and no vortex can be discerned, as would be the case for a vortex domain wall.

As mentioned above, to be able to study the interaction between spin waves and these domain walls, the domain walls must be pinned effectively even when applying small fields in the negative parallel direction, and the domain wall microstructure must be reproducible in repeated measurements. To test the stability of the domain wall around the anti-notch position a small field was applied in the negative parallel direction. Application of a field in this direction should push the domain wall further into, and subsequently through, the anti-notch.

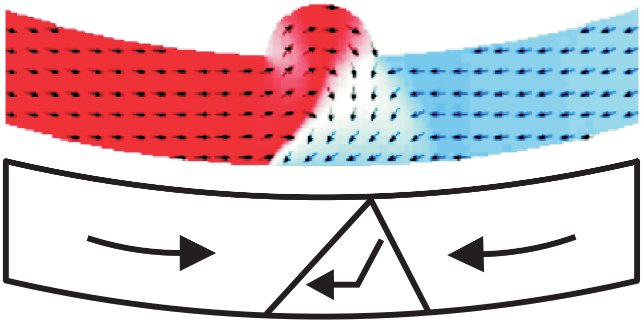

Fig. 3: OOMMF simulation of the magnetization distribution in the vicinity of the anti-notch for comparison with Fig. 2 ($M_s = 860\,\mathrm{emu/cm^3}$, $A = 1.3\times10^{-6}\,\mathrm{erg/cm}$ and $K = 0$). The cell size is $5\,\mathrm{nm} \times 5\,\mathrm{nm} \times 10\,\mathrm{nm}$. A simplified scheme is shown below.

Figure 4 shows the according results. At a field of $-7\,\text{Oe}$ a modest extension ($\sim 25\,\%$) of the domain wall width along the bottom edge of the wire can be observed. By increasing the field further, the wall marked AB in the original domain wall packet became more pronounced and in the end B moved progressively away from the anti-notch and the wall marked AC became increasingly indistinct as the wall angle decreased. At a field of $-13\,\text{Oe}$, B was displaced by almost $1\,\mu\text{m}$ from its original position and by $-15\,\text{Oe}$ the domain wall was completely depinned leaving the wire essentially uniformly magnetized. Only in the immediate vicinity of the anti-notch can a significant variation in the induction orientation be observed. The magnetization close to the edge of the anti-notch tries to follow its contour, thereby reducing magnetostatic energy at the expense of a modest increase in exchange energy.

Similar results were obtained when analyzing the domain wall formation in the $\text{Ni}_{81}\text{Fe}_{19}$ wires with larger radius of curvature.

To check the reproducibility of the domain wall formation and the domain wall character the experiments have been repeated several times, also investigating $\text{Ni}_{81}\text{Fe}_{19}$ structures with radii of 5, 40, 45 and $50\,\mu\text{m}$. It was found that the behavior described above is a qualitatively typical behavior. Quantitatively it was found that the field necessary to pull a domain wall through the anti-notch was about $4 \pm 1\,\text{Oe}$, and the field needed to depin the wall from the anti-notch was about $8.8 \pm 1.3\,\text{Oe}$. Furthermore it was found that local pinning centers in nominally identical wires, such as edge defects, clearly influence this behavior.

In conclusion, the formation and field response of head-to-head domain walls in curved $\text{Ni}_{81}\text{Fe}_{19}$ wires fabricated with a single anti-notch have been investigated successfully using Lorentz-microscopy. High spatial resolution gray scale maps of the vector induction distribution in the vicinity of the anti-notch have been derived from pairs of DPC images. At remanence, the domain wall is in the form of an asymmetric transverse domain wall with modest magnetization circulation occurring in the anti-notch itself. Experimental results and micromagnetic simulations are in good

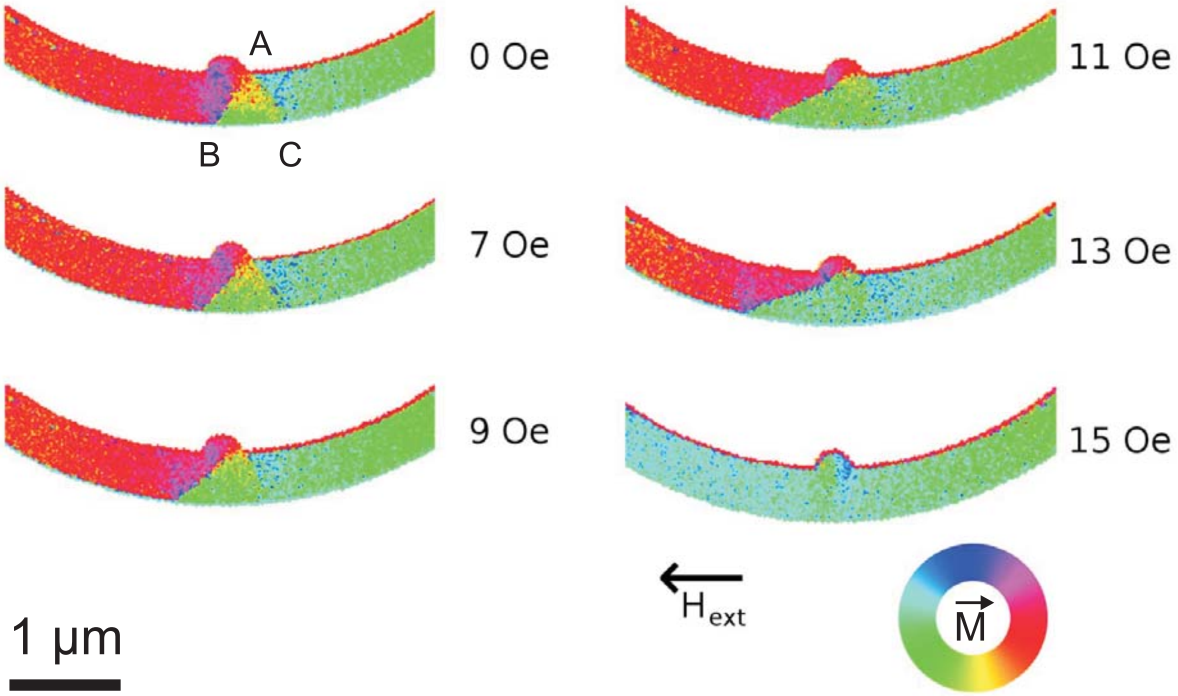

Fig. 4: Gray scale vector maps of the magnetic induction in a curved wire with radius $r = 5\,\mu\text{m}$ under application of increasing magnetic fields in the negative transversal direction.

agreement. Moreover, for wires with the radii of curvature studied here, the remanent domain wall structure was essentially independent of this parameter.

Financial support by the European Commission within the EU-RTN SPINSWITCH (MRTN-CT-2006-035327) and by the DFG within the SPP1133 is gratefully acknowledged.

## References

[1] D.A. Allwood, G. Xiong, C.C. Faulkner, D. Atkinson, D. Petit, R.P. Cowburn, Science **309**, 1688 (2005).

[2] G.A. Prinz, J. Magn. Magn. Mat. **200**, 57 (1999).

[3] R. Wieser, U. Nowak, K.D. Usadel, Phys. Rev. B **69**, 064401 (2004).

[4] C. Chappert, T. Devolder, Nature **432**, 162 (2004).

[5] E. Saitoh, H. Miyajima, T. Yamaoka, G. Tatara, Nature **432**, 203 (2004).

[6] Y. Nakatani, A. Thiaville, J. Miltat, Nature Materials **2**, 251 (2003).

[7] C.A.F. Vaz, T.J. Hayward, J. Llandro, F. Schackert, D. Morecroft, J.A.C. Bland, M. Kläui, M. Laufenberg, D. Backes, U. Rüdiger, F.J. Castano, C.A. Ross, L.J. Heyderman, F. Nolting, A. Locatelli, G. Faini, S. Cherifi, W. Wernsdörfer, J. Phys.: Condens. Matter **19**, 255207 (2007).

[8] F. Junginger, M. Kläui, D. Backes, U. Rüdiger, T. Kasama, R.E. Dunin-Borkowski, L.J. Heyderman, C.A.F. Vaz, J.A.C. Bland, Appl. Phys. Lett. **90**, 132506 (2007).

[9] A. Hubert, R. Schäfer, *Magnetic domains* (Springer, Berlin, Heidelberg, New York, 2000).

[10] B. Khamsehpour, C.D.W. Wilkinson, J.N. Chapman, A.B. Johnston, J. Vac. Sci. Technol. B **14**, 3361 (1996).

[11] J.N. Chapman, J. Phys. D: Appl. Phys. **17**, 623 (1984).

[12] J.N. Chapman, A.B. Johnston, L. J. Heyderman, S. McVitie, W.A.P. Nicholson, IEEE Trans. Magn.**30**, 4479 (1994).

[13] M.J. Donahue, D.G. Porter, *Oommf user's guide, version 1.0* (Interagency, Report NISTIR 6276, National Institute of Standards and Technology, Gaithersburg, MD, 1999).

[14] D. McGrouther, S. McVitie, Appl. Phys. Lett. **91**, 022506 (2007).

## 6.12 Spin waves in semi-circular $Ni_{81}Fe_{19}$ structures with defined domain walls

*C. Sandweg, S.J. Hermsdörfer, H. Schultheiss, B. Leven, and B. Hillebrands*

The properties of spin waves in structures with defined domain walls are a very promising research area, particularly to study the interaction of propagating spin waves and spin-wave pulses with domain walls. To realize this goal three main obstacles have to be identified: firstly, a measurement technique is required which provides spin-wave characterization with a lateral resolution in the sub-micrometer regime, but does not influence the domain distribution in the region of interest. The micro-focus Brillouin light scattering spectroscopy (hereafter referred to as: BLS microscopy) is by now a well established technique which meets the required properties. Secondly, the domain walls have to be reliably induced by applying a defined field sequence, as BLS microscopy does not provide *in-situ* domain characterization. The adjusted sample design of $Ni_{81}Fe_{19}$ structures, which guarantees the presence of a domain wall by applying a defined field sequence, as well as the detailed study of the domain wall structure has been presented in Section 6.11. Thirdly, the excitation of spin waves in the $Ni_{81}Fe_{19}$ structures needs to be achieved with sufficient efficiency. To do so a non-magnetic antenna structure has been adapted to the $Ni_{81}Fe_{19}$ structures.

This report gives an overview of the successful excitation of spin waves in semi-circular $Ni_{81}Fe_{19}$ structures and on the first results concerning the decay length of spin waves influenced by domain walls.

The design and fabrication of the samples has been described in Section 6.11. It follows an idea presented by Saitoh [1] and has also been discussed by Chappert [2] as a so-called domain wall pendulum. The semi-circular $Ni_{81}Fe_{19}$ structure contains a circular protrusion located at the pole of the semi-circle acting as a pinning site for the domain wall. In particular, the chosen semi-circular sample design allows for a defined nucleation and annihilation of a single domain wall in the vicinity of the protrusion by applying a magnetic field in transversal or parallel direction, respectively, and subsequent relaxation of the magnetization to remanence. A schematic view of the sample can be seen in Fig. 1. Here, the $Ni_{81}Fe_{19}$ structure is displayed in gray whereas the antenna realized by a narrow gold stripe is shown in black. The dark spots indicate the data acquisition positions used for obtaining the BLS-spectra. The sample dimensions are a $Ni_{81}Fe_{19}$ semi-circle with a radius of 10 µm, a wire width of 500 nm and a protrusion with a radius of 250 nm revealing a total width at the protrusion of 750 nm (see Fig. 1a). We also investigated a straight

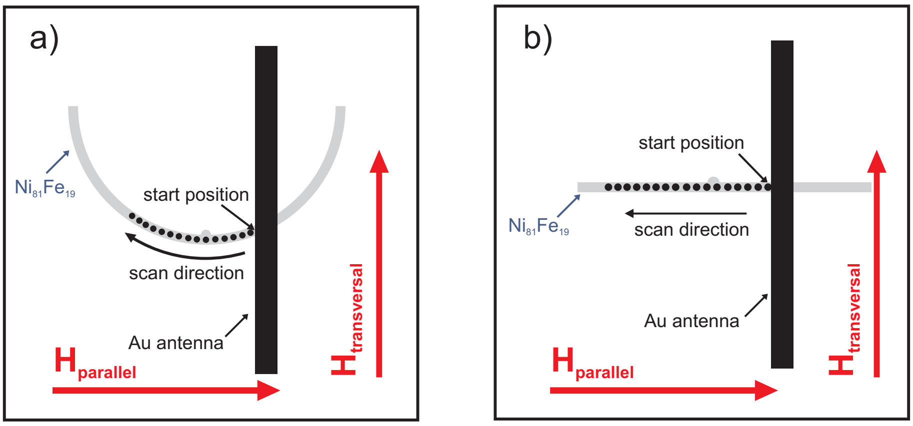

Fig. 1: Schematic view of the setup. Measurements have been carried out along the spots. The externally applied magnetic fields are shown as $H_{transversal}$ and $H_{parallel}$.

$Ni_{81}Fe_{19}$ wire with a width of 400 nm and a protrusion radius of 250 nm (see Fig. 1b). The $Ni_{81}Fe_{19}$ film thickness is 10 nm. The magnetic field directions used to nucleate a domain wall or to saturate the sample are also shown in Fig. 1.

The first step was to investigate the spectra of thermally activated spin waves. The measured BLS-spectra are summarized in a gray scale intensity map where dark gray represents low intensities and bright gray high intensities. The gray scale map comprises 71 data acquisition points, i.e., a length of 6.6 µm in the vicinity of the protrusion has been scanned. To clarify the data presentation we exemplarily show a cut at a certain position of the map representing the intensity profile of the BLS-spectrum at this position. First, the sample was saturated by applying a field $H_{parallel}$ of approximately 1600 Oe thus ensuring that no residual domain walls were present. Figure 2 shows the resulting BLS gray scale map. The inset herein shows the according magnetization distribution obtained by OOMMF-simulations.

Up to four modes of standing spin waves with frequencies near 2.5 GHz, 4.0 GHz, 4.9 GHz and 5.5 GHz can be clearly identified. These Damon-Eshbach modes (whose direction of propagation is perpendicular to the magnetization of the structure) are quantized due to the reduced dimension of the structure in transversal direction.

In the next step of the experiments, an external magnetic field was applied in parallel direction (see Fig. 1) and reversed to remanence. The domain structure which is initiated by this procedure has already been discussed in detail in Section 6.11. It was shown that an asymmetric transverse domain wall is nucleated in the structure and pinned in the vicinity of the protrusion. The corresponding BLS intensity map, as well as the resulting magnetization distribution obtained by OOMMF-simulations are shown in Fig. 3.

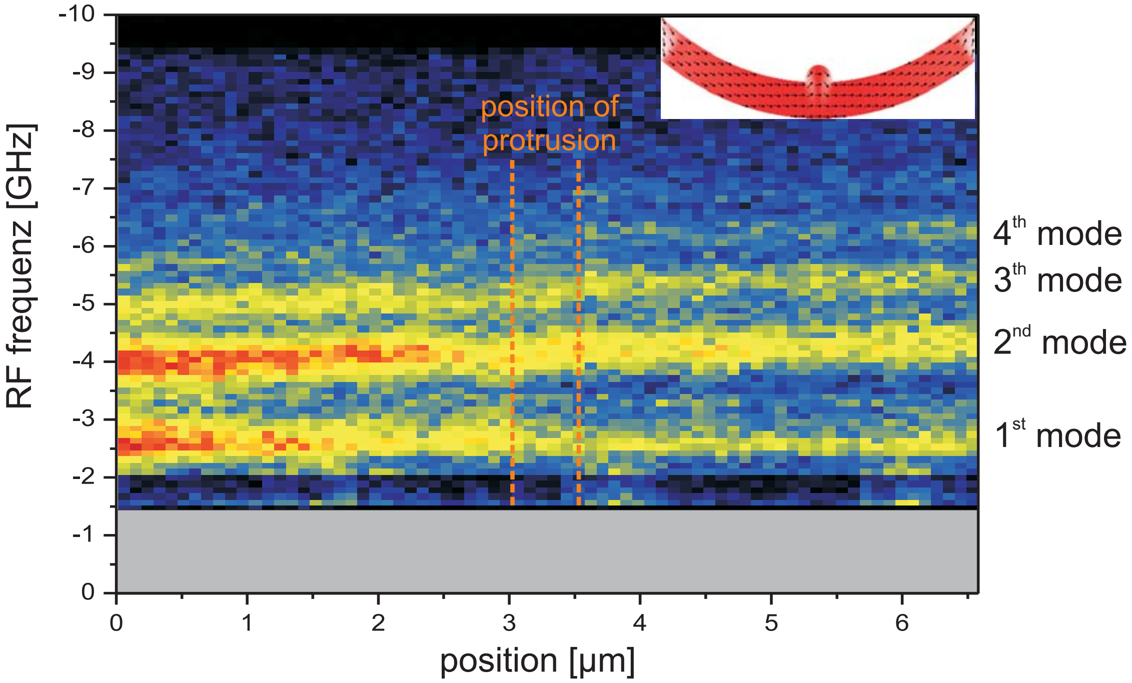

Fig. 2: Intensity map summarizing of the spectra of thermally activated spin waves in the semi-circular $Ni_{81}Fe_{19}$ structure in the absence of domain walls. Four magnetostatic surface modes can be identified being quantized due to the geometrical confinement of the structure in transversal direction. The minor shift of the modes can be explained by small variations of the width, the decrease of intensity by a slightly drifting focus. Inset: Result of corresponding OOMMF-simulation.

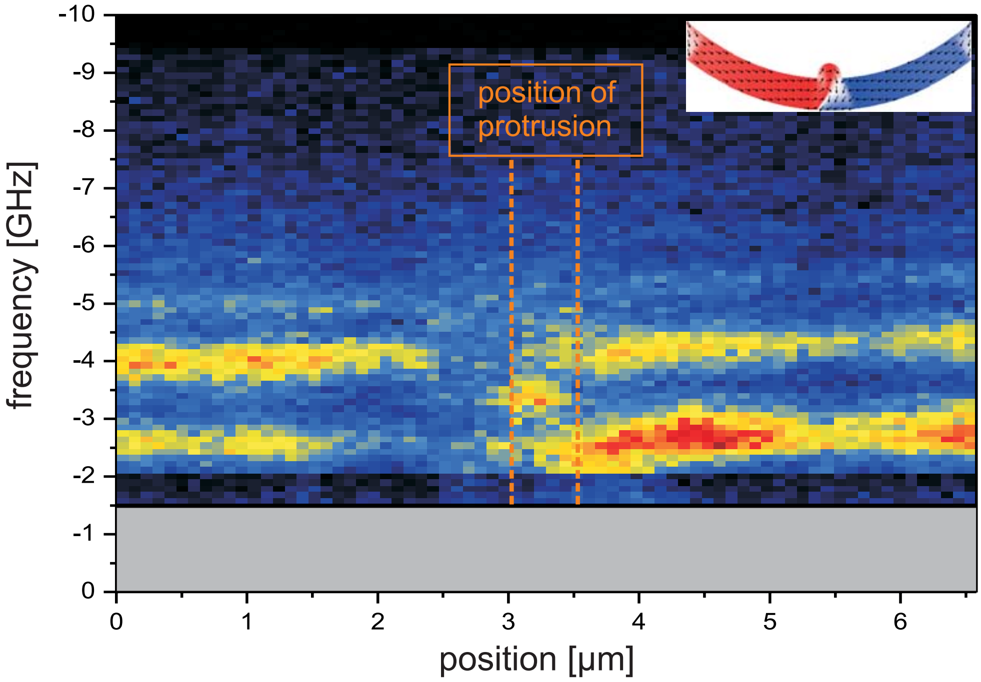

Fig. 3: Intensity map of the spin wave distribution in the semi-circular $Ni_{81}Fe_{19}$ structure in the presence of a domain wall. The gray scale code is defined in Fig. 2. Inset: Result of corresponding OOMMF-simulation.

By comparing the intensity maps obtained with and without a domain wall, obvious differences in the spectra can be determined: instead of the original four modes observed without a domain wall (see Fig. 2) a new mode arises directly before the position of the protrusion whereas the other modes vanish in this area. This behavior can be understood in terms of a decrease of the local internal magnetic field $\mathbf{h}_{\text{eff}}$ [3]. Thus, the spin-wave frequency is shifted according to the dispersion relation for magnetostatic spin waves:

$$\nu_{MSSW} = \frac{\gamma}{2\pi}\sqrt{H(H+4\pi M_s)+(2\pi M_s)^2(1-e^{-2k_\parallel d})}. \tag{1}$$

Furthermore, the magnetization distribution inside the domain wall causes a change in the spin-wave characteristics according to the variation of the angle between the magnetization **M** and the propagation direction of the spin waves inside the wall. Thus, inside the domain wall we find modes, which are better approximated by magnetostatic backward volume modes instead of magnetostatic surface waves.

After successful characterization of the thermally excited spin-wave distribution occurring in the semi-circular $Ni_{81}Fe_{19}$ structures, the excitation of spin waves by a microwave source with tunable frequency is of great interest. Hence, to excite spin waves in the GHz regime the sample was equipped with a gold antenna adjusted to the $Ni_{81}Fe_{19}$ structure leading the microwave current towards the magnetic semi-circle. The measurements have been carried out for the semi-circular structure as well as for a $Ni_{81}Fe_{19}$ stripe, as has been shown in Fig. 1a and 1b, respectively. A microwave generator with a frequency range between 2 GHz and 18 GHz and an additional microwave amplifier have been used. The nominal microwave power available was at most 43 dBm. However, the microwave power being transferred to the $Ni_{81}Fe_{19}$ structure was determined by employing a network analyzer. It turned out that the microwave transfer efficiency is quite weak resulting a microwave power of only around 29 dBm. This behavior is attributed to the impedance mismatch between the microwave source and the antenna structure and is going to be optimized in future experiments.

To characterize the excitation of the spin system, a FMR analysis has been performed. Note that this artificial excitation of the spin system is based on the Oersted field produced by the microwave current. In this particular case it is limited to the out-of-plane component of the Oersted field as only this component can transfer a torque to the in-plane aligned magnetic moments of the $Ni_{81}Fe_{19}$ sample according to the Landau-Lifshitz and Gilbert equation.

To obtain the FMR frequency of the system, BLS-spectra for varying frequencies have been taken at a fixed point of the sample. The frequency with the highest intensity in the spectrum was identified as the FMR-frequency of 2.2 GHz.

To study the characteristics of the excited spin system, the measurements have been performed by scanning along the stripe as described above. The first point was situated where the antenna touches the stripe ($x = 0\,\mu m$), the last point at the end of the stripe ($x = 12\,\mu m$). This means that the scanning direction was always away from the antenna.

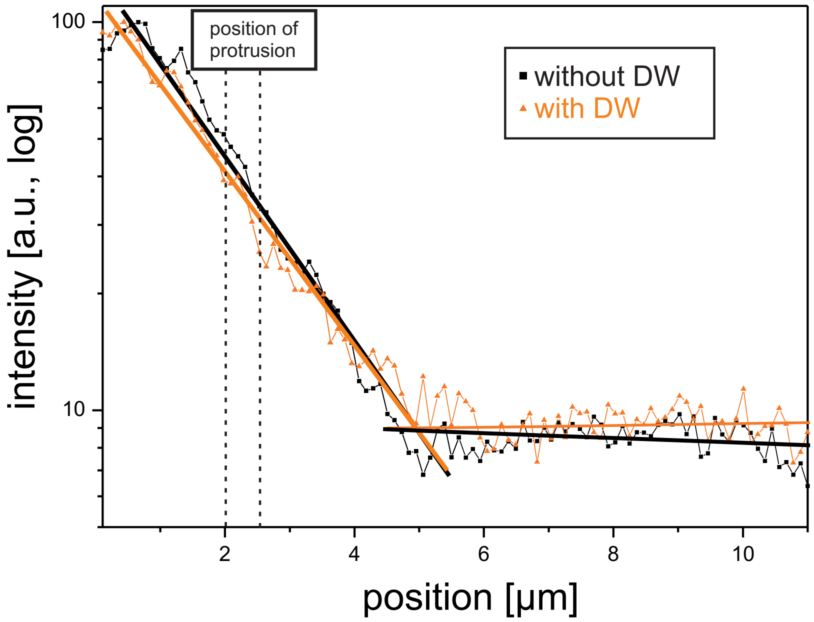

Fig. 4: Intensity profile of the measured spin wave modes before and after nucleation of a domain wall at the ferromagnetic resonance frequency of 2.2 GHz. The exponential decay can be clearly determined as well as the decay length from the linear regression line.

Figure 4 shows the intensity profiles of the spin waves at the resonance frequency in the presence and absence of a domain wall. A strong exponential decay is observed. In case of excitation with the resonance frequency, only spin waves with a wave vector $k = 0$ are excited and therefore a pure exponential decay can be observed. From this plot the decay length can be determined to be 4.2 µm without a domain wall and 4.5 µm with a domain wall using a linear regression.

The more interesting case are spin waves with a finite wave vector, which can be achieved by off-resonant excitation. Figure 5 shows an intensity profile taken from the same sample as before but with a frequency of 2.4 GHz. This time a clear difference in the results obtained before and after the nucleation of a domain wall can be observed. In the semi-logarithmic scale two areas can again be distinguished: one revealing a decay length of 4.3 µm, which is comparable to the results obtained when resonantly exciting the sample, and a second one with a decay length of 11.1 µm continuing towards the end of the structure. It can be concluded that we have excited propagating spin waves in the present $Ni_{81}Fe_{19}$ structure.

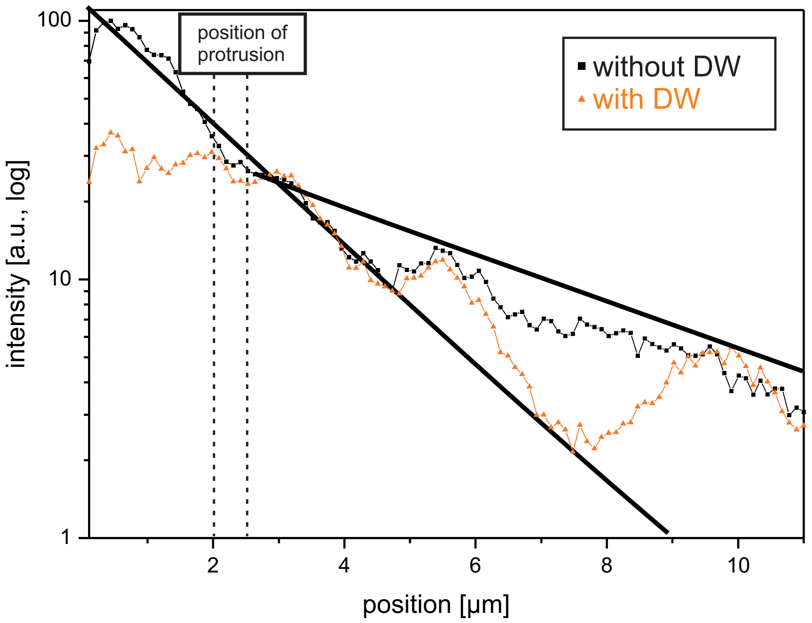

Fig. 5: Intensity of measured spin waves at 2.4 GHz but in the same configuration as Fig. 4. In the semi-logarithmic plot two areas can be distinguished: one which is still governed by the FMR and a second with a much higher decay length giving strong hints to propagating spin waves.

Next, we study artificial spin-wave excitation in particular of propagating spin waves in the semi-circular $Ni_{81}Fe_{19}$ structure. The results which are presented in Fig. 6 reveal a similar behavior as discussed in the case of the $Ni_{81}Fe_{19}$ stripe. This supports the conclusion that we succeeded to excite propagating spin waves in the $Ni_{81}Fe_{19}$ structures.

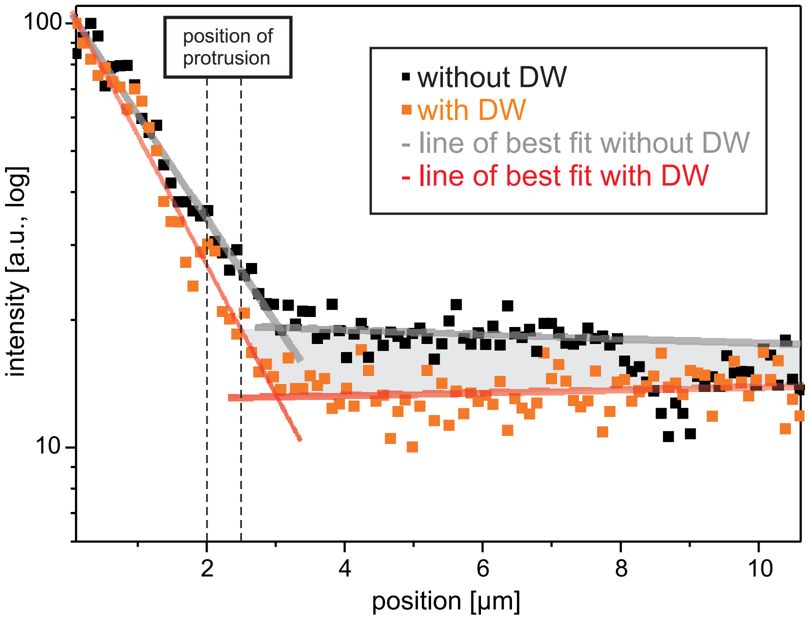

Fig. 6: Intensity of the spin waves at 2.4 GHz in the semi-circle structure (radius 10 μm). Again the strong decay in the area governed by the FMR can be observed as well as the propagating spin waves.

For a semi-circle with a radius of 10 μm and a width of 400 nm the difference between the intensity profiles before and after nucleation of a domain wall can be observed although it is less pronounced as before.

Financial Support by the DFG within the Priority Program 1133 is gratefully acknowledged.

## References

[1] E. Saitoh, H. Miyajima, T. Yamaoka, G. Tatara, Nature **432**, 203 (2004).
[2] C. Chappert, T. Devolder, Nature **432**, 162 (2004).
[3] C. Bayer, H. Schultheiss, B. Hillebrands, R.L. Stamps, IEEE Trans. Magn. **41**, 3094 (2005).

# D. Applied Research and Technology

## 6.13 XNOR and NAND spin-wave logic gates

*T. Schneider, A.A. Serga, B. Leven, and B. Hillebrands*[1]

Although commonly used for data storage applications, there are relatively few attempts to employ magnetic phenomena for performing logical operations. Recently a universal logic gate based on the collective magnetostatic field of a chain of magnetic nanoelements was demonstrated [1]. Another concept investigated theoretically in [2–4] is based on a spin-wave interferometer. Up to now there was only one experimental demonstration of that concept [5], where a logical NOT gate was realized in a Mach-Zehnder type interferometer structure. Here we demonstrate how this approach can be extended to realize two two-input spin-wave logical gates.

The XNOR logic gate is a direct extension of the NOT gate from [5]. For its implementation the reference interferometer arm of the NOT gate is replaced by an arm identical to the signal arm. The possibility to control the phases accumulated by the spin waves in both arms allows one to perform the XNOR operation.

The realization of a NAND gate is a considerable step forward in development of spin wave logic compared to the NOT and XNOR gates, since the NAND function belongs to a class of universal functions which means that combining NAND gates allows one to construct gates of other types. The principe used to realized that gate is the direct control of the spin wave amplitudes in the interferometer arms by strongly localized changes of the bias magnetic field.

Figure 1b shows the principle setup of an exclusive not OR (XNOR, also called logical equality) gate. It consists of two arms of a spin-wave Mach-Zehnder interferometer implemented as ferrite spin-wave waveguides. The phase accumulated by spin waves on their paths through the arms is controlled by applying dc currents $I_1$ and $I_2$ to the conductors placed in each arm. Figure 1a shows phases inserted due to the currents for both interferometer arms (for more details on this effect see [5]). One sees linear dependence of the accumulated phase on the current. One also sees that the phase characteristics for both arms are identical.

The logical inputs are realized by the currents passing through the phase shifter were a logical zero is represented by $I_0 = 0\,\mathrm{A}$ and logical one by the current $I_\pi$ necessary to create a phase shift of $\pi$. The interference signal of the combined spin waves represents the logical output (destructive interference (i.e., zero intensity) for logical zero and constructive interference (high intensity) for logical one). It is assumed that both branches are identical and thus both spin waves should reach the output with identical amplitude and phase if no current is applied. If we now apply a current of $I_\pi$ to one of the phase shifters (i.e., logical one to one input, zero to the other) one of the spin waves is shifted in phase by $\pi$ which will lead to destructive interference (logical 0). If the current for both phase shifters is identical (i.e., logical zero or one to both inputs) the interference will remain constructive (logical one). This behaviour (summarized in the inset a Fig. 1b) matches a XNOR gate.

To simplify demonstration of functionality of the XNOR gate we used a macroscopic structure based on two 6 µm thick and 1.5 mm wide yttrium-iron-garnet (YIG) films. It is necessary to note

---

[1] In collaboration with M.P. Kostylev, School of Physics, University of Western Australia, Crawley, Australia.

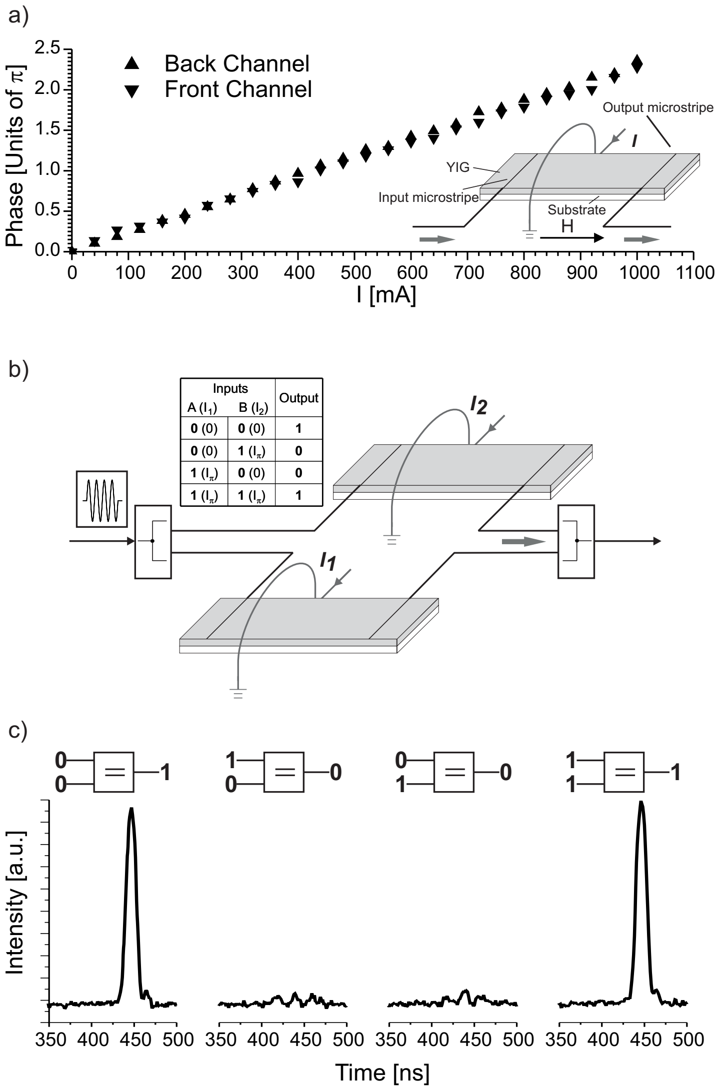

Fig. 1: XNOR gate. a) Inserted phase versus current for the current controlled spin wave phase shifters (CPS) used to construct the XNOR gate prototype. It is clearly visible that the phase shifts in both arms (channels) are identical. The inset shows the phase shifter geometry. b) Spin-wave XNOR gate geometry. The currents $I_1$ and $I_2$ represent the logical inputs (0 A corresponds to **0**, $I_\pi$ corresponds to **1**), the spin-wave interference signal represents the logical output. Inset: Truth table for an XNOR gate. c) Gate output signals for input signals shown in the diagrams.

that the physical principles underlying the device performance would remain practically the same if the prototype was implemented with micrometer sizes. In YIG films spin waves can travel over several tens of millimeters due to its extremely low magnetic damping. Conventional Permalloy films allow for spin wave propagation over distances up to several tens of micrometers and are well suited for miniature devices. The physical input and output of the interferometer are implemented as 50 µm wide microwave microstripe antennas placed 8 mm apart from each other. (Note that the interferometer physical input and output can be implemented as all-spin wave waveguides, as shown in [2]). This will make them compatible with a spin wave data bus, as recently suggested in [6].) Conductors for spin wave phase control are placed between the input and the output microwave transducers. Microwave carrier frequency of the pulses was 7.132 GHz, applied bias magnetic field was 1850 Oe. The used spin-wave pulses in both interferometer arms are 20 ns in length, control current pulses with a length of 990 ns are applied to the conductors. Additional experiments showed that the length of the current pulses can be reduced to the length of the spin-wave pulses at the cost of an increased current necessary to create the π shift due to the then shorter interaction time.

Figure 1c demonstrates the microwave signal at the output of the prototype gate for different input configurations. The expected behavior is clearly visible.

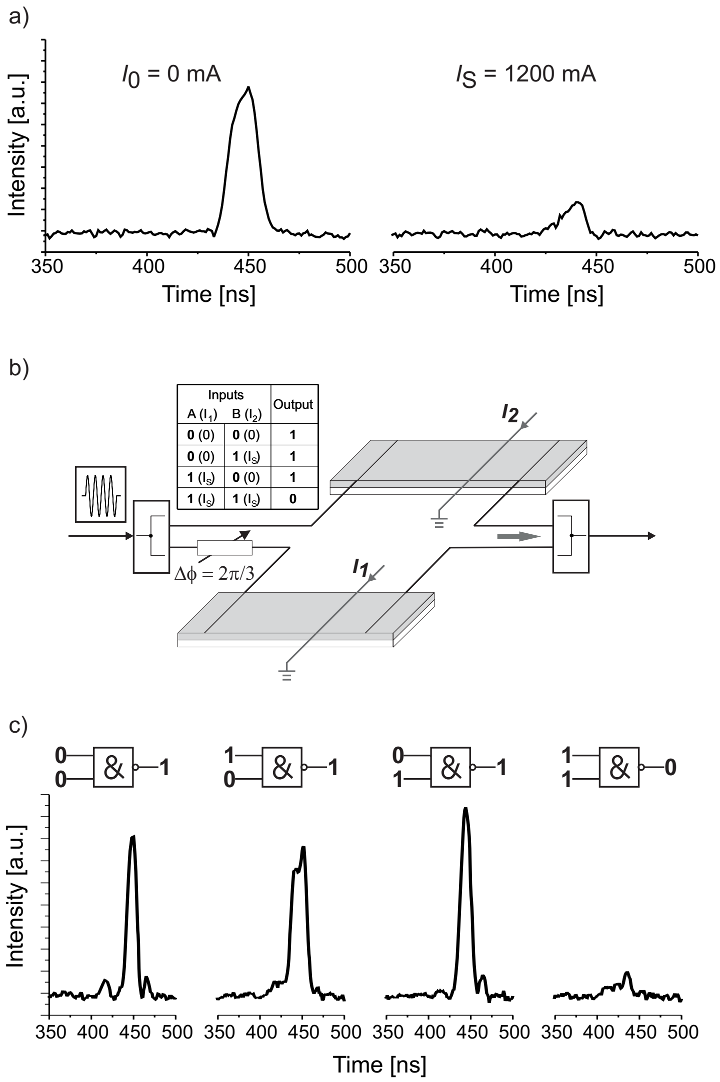

Fig. 2: NAND gate. a) Demonstration of a spin-wave switch. Left part: Output signal without applied current. Right part: Output signal with applied current. Suppression of the output pulse is clearly visible. b) Geometry of a spin-wave NAND gate. The currents $I_1$ and $I_2$ represent the logical inputs (0 A corresponds to **0**, $I_S$ corresponds to **1**); the spin-wave interference signal represents the logical output. Inset: Truth table for a NAND gate. c) Gate output signals for input signals as shown in the diagrams.

It has been shown [7, 8] that one can control spin wave amplitude by inserting a highly localized magnetic field inhomogeneity. These inhomogeneity can be created by a dc current applied to a narrow conductor placed on the surface of the used spin-wave waveguide. A conductor with a width of 100 µm produces such a highly localized Oersted field. In this work we choose the current direction which produces an Oersted field in the direction opposite to the applied field. Then by applying a relatively small current it is possible to shift the dispersion curve so that the carrier frequency of the spin wave pulse incident onto the inhomogeneity is not longer inside of the frequency band of spin waves, thus creating a prohibited zone were spin waves cannot propagate, but only tunnel. This leads to a strong back reflection of the incident pulse and one observes a strong change in the intensity of the spin wave [7]. It is important to notice that one can reduce the spin wave amplitude to nearly zero and thus can use this setup as a spin-wave switch. The functionality of such a switch is demonstrated in Fig. 2a.

The realization of a logic not AND (NAND) gate is demonstrated in Fig. 2b. The setup mainly consist of a Mach-Zehnder interferometer but this time the phase shifters in the arms are replaced by switches. Similar to the XNOR gate the logical output is implemented by the interference signal, while the inputs are implemented by the currents. Logical zero is represented by $I_0 = 0\,\text{A}$, and logical one by the current $I_S$ necessary to suppress the spin wave pulse transmission.

Experimentally measured output interferometer pulses are shown in Fig. 2c. If a current is applied to one of the switches only (logical one to one input, zero to the other) a microwave pulse of large intensity is transmitted (logical one at the output). The same occurs if no current is applied to both arms (logical zero to both inputs). An additional permanent phase shift of $2\pi/3$ introduced in one of the interferometer arms ensures that in this case the output intensity is the same as in the two other cases of logical one at the output. While we used an external coaxial microwave phase shifter in this prototype, one can use other possibilities to create an additional phase shift such as making spin-wave propagation paths in the arms differing by $2\pi/3$ by slightly increasing the length of one of the arms or using a thin permanent magnet to apply a small additional bias magnetic field to one of the arms. A current applied to both switches (logical one to both inputs) leads to a nearly complete suppression of the output signal (logical zero). The described behavior (summarized in the inset of Fig. 2b) is the one of a NAND gate.

In summary, we demonstrated a new possibility to realize NAND and XNOR logical gates using spin waves propagating in a Mach-Zehnder type interferometer. The prototypes have been created using YIG waveguides. By changing the used material (e.g., to Permalloy) a downscaling of the presented devices should be possible.

This work has been supported by the DFG (Graduiertenkolleg 792), the Australian Research Council and the European Community under the Sixth Framework Programme Contract Number 510993: MAGLOG. The views expressed are solely those of the authors, and the other Contractors and/or the European Community cannot be held liable for any use that may be made of the information contained herein.

## References

[1] A. Imre et al., Science, **311**, 205 (2006).

[2] R. Hertel, Phys. Rev. Lett. **93**, 257202 (2004).

[3] S.V. Vasiliev, V.V. Kruglyak, M.L. Sokolovskii, A.N. Kuchko, J. Appl. Phys., **101**, 113919 (2007).

[4] S. Kim, K. Lee, S. Choi, 10th Joint Intermag-MMM Conference, Baltimore, Poster CU-10 (2007).

[5] M.P. Kostylev, A.A. Serga, T. Schneider, B. Leven, B. Hillebrands, Appl. Phys. Lett. **87**, 153501 (2005).

[6] A. Khitun, K.L. Wang, Superlattices and Microstructures, **38**, 184-200 (2005).

[7] S.O. Demokritov, A.A. Serga, A. André, V.E. Demidov, M.P. Kostylev, B. Hillebrands, A.N. Slavin, Phys. Rev. Lett. **93**, 047201 (2004).

[8] M.P. Kostylev, A.A. Serga, T. Schneider, B. Leven, B. Hillebrands, R.L. Stamps, Phys. Rev. B in press.; M.P. Kostylev, A.A. Serga, T. Schneider, B. Leven, B. Hillebrands, R.L. Stamps, arXiv:0705.4191v1.

## 6.14 *Ex-vivo* investigations on the friction behavior of amorphous carbon coated ureteral stents

*L. Kleinen, U. Böde, and B. Hillebrands*[1]

The Institute of Thin Film Technology (IDST) is a specialist for plasma-deposited multifunctional coating systems and biocompatible surfaces developing tailor-made solutions for industry and the private sector. Located at the TZO Rheinbreitbach near Bonn the IDST supports local business start-ups in the field of surface and plasma technology.

One of the major topics currently investigated at the IDST is the reduction of biofilm formation on urological implants. An especially developed flexible yet dense amorphous carbon (a-C:H) film was plasma-deposited on ureteral stents and showed significant advantage over conventional coatings and materials with respect to biofilm reduction. The convincing *in-vitro* results were already confirmed in clinical studies. Beyond the reduction of biofilm formation and prolongation of implant-indwelling time, patients report on the good wear comfort of the a-C:H coated stents, that often is accredited to the low friction coefficient of amorphous carbon. With an *ex-vivo* model we investigate, if the amorphous carbon coated stents really show lower friction coefficients against wet tissue or if other properties of the a-C:H coated stent cause the subjective impression "higher wear comfort".

Surface wettability and reduced friction are considered to play a major role in the wearing comfort of urological implants. Ureteral stents and transurethral catheters are routinely placed in the urinary tract to ensure unobstructed urine transport from the kidney to the bladder or from the bladder to the outside. These treatments are necessary in case of dysfunctional urine transport, e.g. related to tumor diseases.

Figure 1 shows a diagram of the urinary tract and examples for the placement of ureteral stents and transurethral catheters. The computer tomography in the right image reveals a large tumor in the patient's abdomen. The stent placement procedure (insertion via the urethra, bladder and ureter) strongly suggests the importance of low friction for patient comfort, especially in the presence of ureter confining tumors. Friction should be as low as possible to facilitate insertion of the implant and to reduce any risk of micro-trauma related inflammation. Indwelling ureteral stents are affected

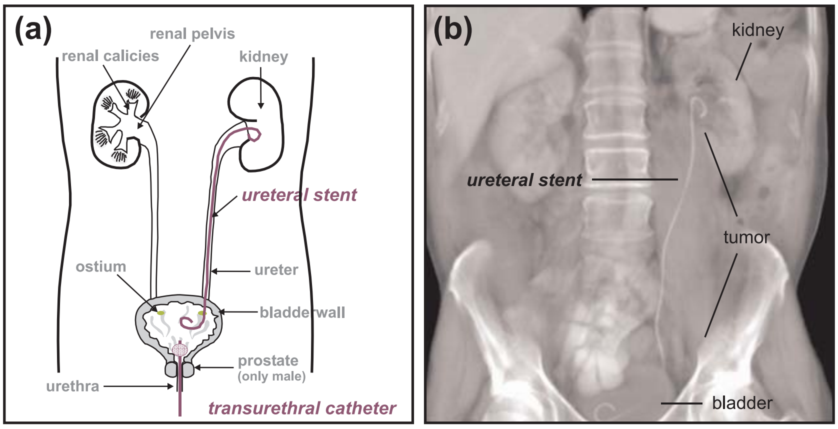

Fig. 1: Urinary tract with implants (a) and computer tomography (b) of patient's abdomen with indwelling ureteral stent. A ureter enclosing tumor required stent placement.

---

[1] In collaboration with N. Laube, Universitätsklinikum Bonn.

by pulsatile dislocations and relative movements with each breath (approximately 15 breaths/min). The stent itself may become twisted, bent, extended, or compressed. Overlying body movements may additionally lead to stress and strain pulses in the ureter-stent-system.

Recently, we reported on the advantages of amorphous carbon coatings for urological implants [1, 2]. *In-vitro* and *in-vivo* studies on amorphous carbon (a-C:H) coated ureteral stents revealed a significant reduction of biofilm formation by some of these thin films. This allows for distinctly prolonged indwelling times of the implants. Furthermore, facile handling, less painful replacement procedure and high tolerance during indwelling were reported by physicians and patients.

In this study, we investigate the friction behavior of a-C:H coatings on ureteral stents as a possible cause for the observed advantages in wearing comfort. Conventional tribological methods (e.g. ball-on-disc measurements) do not represent the *in-vivo* conditions sufficiently with possibly misleading results. Animal models, however, often lack in reproducibility and require large logistic, legal and time-consuming efforts. Therefore, an *ex-vivo* friction testing device was developed to simulate conditions in the urinary tract and to allow reproducible determination of the friction coefficient of different surfaces on a macroscopic scale in wet surroundings.

Uncoated PU (polyurethane) tubes supplied by a stent manufacturer were coated with three different, 50 nm thick a-C:H-films. a-C:H(1) was deposited from pure $C_2H_2$ precursor gas. In order to achieve different surface wettabilities, $NH_3$ or $CF_4$, respectively, was added during the coating process. Uncoated PU tubes were used as reference material. In addition, three commercially available ureteral stents with different coatings were included in the study (stent type 1, 2 and 3). Prior to analysis of wettability and friction behavior, all samples were pre-soaked for one hour in physilogical NaCl solution, a procedure recommended by several stent manufacturers.

To determine surface wettability of samples, optical contact angle (OCA) measurements were performed using the sessile drop method. The baseline was defined manually according to the substrate curvature (see photo inserts in Fig. 2).

The drop contur was fitted and the contact angle was determined as the slope of the contour-line at the three-phase contact point. In order to determine the influence of pre-soaking in NaCl solution, water contact angles (WCA) were measured on dry and pre-soaked samples. Before applying the sessile drop method, any surplus NaCl solution was carefully removed with filter paper. The results of the water contact angle measurements are shown in Fig. 2. In any case, the water contact angles on pre-wetted surfaces are smaller.

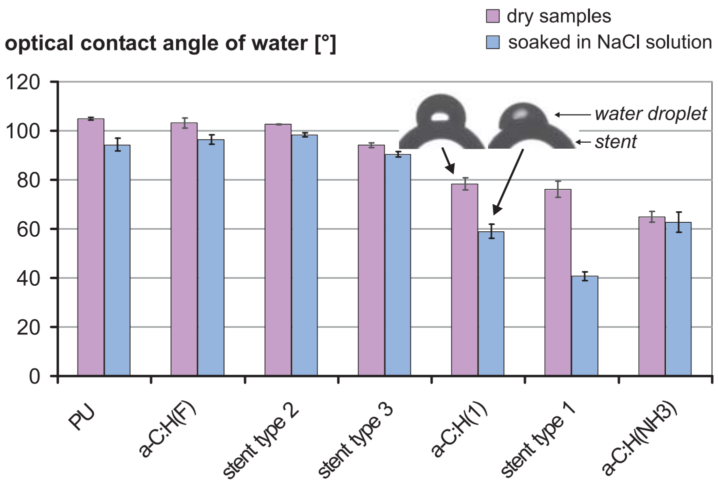

Fig. 2: Results of optical water contact angle measurements (mean values ± standard deviation) on various surfaces. PU: uncoated polyurethane reference, stent type 1-3: commercially available stents. a-C:H(F), a-C:H(1), a-C:H(NH3): differently composed amorphous carbon films.

The friction coefficients of the surfaces were determined in an *ex-vivo* model using porcine liver as phantom material and saline solution as lubricant (Fig. 3). The liver's outer surface is supposed to show a similar friction behavior to that of the ureter's endothelial tissue with its specialized mucosa and secretory capabilities. The stents were placed between the liver slices, and distance-force diagrams were taken at different loads simulating variable tumor pressures. In order to ensure the same initial load with different liver slices, differences in the weight of the covering block were adjusted by an additional load of sand. Based on the experiment's geometry, the stent specimens were loaded with pressures of 103 to 309 Pa. These relatively low pressures do not lead to stent deformation, confining the friction interaction on the sample surface.

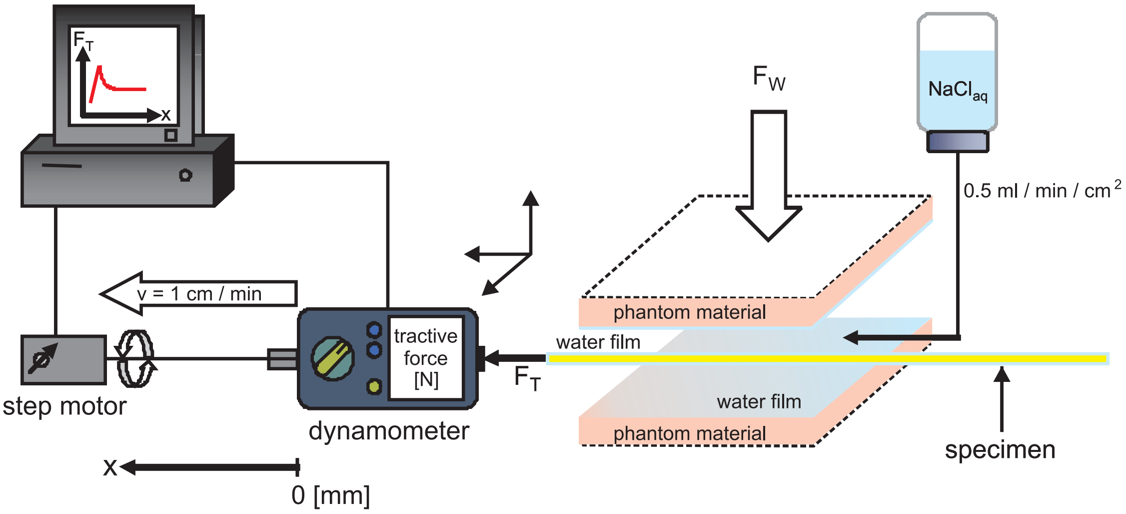

Fig. 3: Experimental setup for determination of the coefficients of static and dynamic friction. This device allows for standardized tests without extensive logistic efforts prior to measurements and fulfills the important requirements of reproducibility of the experiment. We favored this *ex-vivo* model over an *in-vivo* animal model with always-different ureter diameters and hardly reproducible pressures within the animal's abdomen.

Seven different surface types of ureteral stents and coated PU tubes were tested with the *ex-vivo* model. Each surface type was tested three-times under each particular load to obtain a statistically valid number of results. For each test cycle, a new gliding trajectory was adjusted by lateral movement of the phantom material. For each load, a new specimen was used. Each sample type was tested against a new uncoated reference PU sample. For each sample type and its reference, two fresh liver slices were used. A typical force-path diagram is shown in figure 4.

To compare the friction behavior of different surfaces, the relative friction coefficients are determined by dividing the highest friction coefficients $\mu_{sample}$ determined for the specific sample by the highest friction coefficient $\mu_{PU}$ of the uncoated PU reference (both measured with the same liver slices). Figure 5 shows the dependency of the relative friction coefficients on the applied pressure for the six evaluated surface types. With the exception of stent type 3 and the a-C:H(1) and a-C:H(NH3) coatings under very low load, all tested surfaces have higher friction coefficients than the PU reference samples. These relationships do not change when using the median or mean values of the friction coefficients for the samples and references to determine the relative friction coefficient. Furthermore, no direct correlation between wettability of the surfaces and their friction behavior could be established.

As opposed to common expectations, no reduction of friction by coating with different a-C:H films could be verified. On closer examination, these observations are consistent with the results

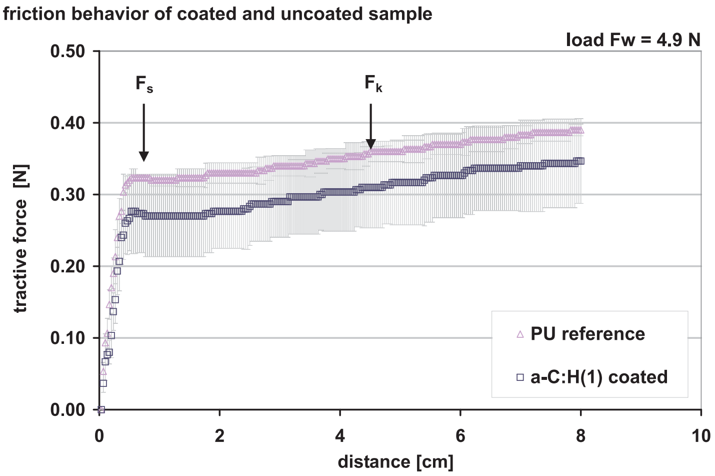

Fig. 4: Typical plot showing a distance *vs.* tractive force path obtained from the measurements with the *ex-vivo* friction testing device. Two distinct points are marked in the graph: first, the force $F_s$ applied at the moment the instant motion between surfaces starts, and second, the section marked with $F_k$. $F_s$ ist the force required to pull the stent with constant velocity.

of several studies on the dependency of the friction behavior of amorphous carbon thin films on the relative humidity of the surroundings [3–5]. The biofilm reducing a-C:H coatings prepared for this study contain a large fraction (approx. 40 %) of hydrogen within the amorphous network. These films show ultra-low friction only in vacuum [4], while in humid air, the friction coefficient increases substantially [5].

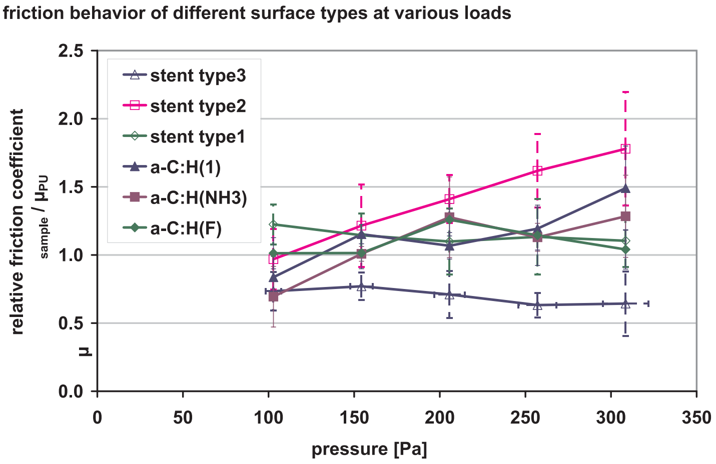

Fig. 5: Dependency of the relative friction coefficients $\mu_{sample}/\mu_{PU}$ on the applied pressure for several surface types. With the exception of one sample (stent type(3)) all measured values lie within the same order of magnitude. The a-C:H coatings showed no significant reduction of friction *ex-vivo*.

Claimed benefits of commercially available stents with hydrophilic coatings imply a strong influence of the surface wettability on the friction behavior. This could not be verified in this study. The independent, positive experiences of patients with stents with biofilm reducing a-C:H coatings suggest that the relevance of low friction surfaces for the patient's subjective wear comfort might be overrated [6]. Rather do various properties of the coated stents (e.g. dense surface, less biofilm formation) contribute to the observered good wearing comfort.

Support by the *BMBF* is gratefully acknowledged. We thank Mrs. Dentler for editorial help.

## References

[1] N. Laube, L. Kleinen, J. Bradenahl, A. Meißner, J. Urol. **177**, 1923 (2007).
[2] L. Kleinen, U. Böde, K. Schenk, H. Busch, J. Bradenahl, S.C. Müller, B. Hillebrands, N. Laube, Plasma Process. Polym. **4**, 386 (2007).
[3] J. Robertson, Mat. Sci. Eng. R **37**, 129 (2002).
[4] C. Donnet, Surf. Coatings Technol. **100**, 180 (1998).
[5] A. Erdemir, C. Donnet, J. Phys. D: Appl. Phys. **39**, R311 (2006) .
[6] L. Kleinen, U. Böde, N. Laube, submitted to Diam. Rel. Mat..

# Chapter 7: Publications

Most publications can be downloaded from http://www.physik.uni-kl.de/hillebrands.

## 7.1 published

1. *Investigation of Spin Waves and Spin Dynamics by Optical Techniques*
   B. Hillebrands, J. Hamrle
   in Handbook of Magnetism and Advanced Magnetic Materials, Vol. 3
   H. Kronmüller, S.P. Parkin editors, Wiley-Interscience (2007).

2. *Kerr microscopy studies of microwave assisted switching*
   P. Martín Pimentel, H. Grimm, B. Leven, B. Hillebrands
   J. Appl. Physics **102**, 063913 (2007).

3. *Observation of coupled magnetic vortex structure dynamics by time-resolved magneto-optical Kerr effect microscopy*
   R. Antos, J. Hamrle, H. Masaki, T. Kimura, J. Shibata, Y. Otani
   Proc. SPIE 6479 (2007).

4. *Preparation, Characterization and Magneto-optical investigations of electrodeposited Co/Au films*
   P. Prod'homme, F. Maroun, R. Cortès, P. Allongue, J. Hamrle, J. Ferré, J.-P. Jamet, N. Vernier
   J. Magn. Magn. Mater. **315**, 26 (2007).

5. *Ion beam-induced magnetic nanopatterning of interlayer exchange coupled Fe/Cr/Fe trilayers*
   S. Blomeier, P. Candeloro, B. Hillebrands, B. Reuscher, A. Brodyanski, M. Kopnarski
   J. Magn. Magn. Mater. **310**, 2353 (2007).

6. *Huge quadratic magneto-optical Kerr effect in the $Co_2FeSi$ Heusler compound* J. Hamrle, S. Blomeier, O. Gaier, B. Hillebrands, H. Schneider, G. Jakob, K. Postava, C. Felser
   J. Phys. D: Appl. Phys. **40**, 1563 (2007).

7. *Ion beam induced modification of exchange interaction and spin-orbit coupling in the $Co_2FeSi$ Heusler compound*
   J. Hamrle, S. Blomeier, O. Gaier, B. Hillebrands, H. Schneider, G. Jakob, B. Reuscher, A. Brodyanski, M. Kopnarski, K. Postava, C. Felser
   J. Phys. D: Appl. Phys. **40**, 1558 (2007).

8. *Linear and nonlinear phase accumulation of backward volume magnetostatic spin waves in yttrium-iron-garnet spin-wave waveguides*
   T. Schneider, A.A. Serga, B. Hillebrands, M.P. Kostylev
   Europhys. Lett. **77**, 57002 (2007).

9. *Microwave assisted switching in a $Ni_{81}Fe_{19}$ ellipsoid*
   H.T. Nembach, P. Martín Pimentel, S.J. Hermsdoerfer, B. Leven, S.O. Demokritov, B. Hillebrands
   Appl. Phys. Lett. **90**, 062503 (2007).

10. *Shaping of microwave pulses using phase-sensitive spin-wave amplifier*
    A.A. Serga, T. Schneider, B. Hillebrands, M.P. Kostylev, A.N. Slavin
    Appl. Phys. Lett. **90**, 022502 (2007).

11. *Diamond-like carbon coatings on ureteral stents - A new strategy in reducing formation of crystalline bacterial biofilms?*
    N. Laube, J. Bradenahl, A. Meißner, L. Kleinen
    Journal of Urology, **177**, 1923 (2007).

12. *Amorphous carbon coatings inhibit crystalline biofilm formation on urological implants*
    L. Kleinen, U. Böde, K. Schenk, H. Busch, J. Bradenahl, S.C. Müller, B. Hillebrands, N. Laube
    Plasma Processes and Polymers **4**, 386, (2007).

13. *Plasmadeponierte funktionalisierte Kohlenstoffschichten zur Minderung von Inkrustationen auf urologischen Implantaten*
    N. Laube, L. Kleinen, U. Böde, C. Fisang, A. Meißner, J. Bradenahl, I. Syring, H. Busch, W. Pinkowski, S.C. Müller
    Der Urologe **9**, 1249 (2007).

14. *Magnetic anisotropies and magnetization reversal of the* $Co_2Cr_{0.6}Fe_{0.4}Al$ *Heusler compound*
    J. Hamrle, S. Blomeier, O. Gaier, B. Hillebrands, R. Schäfer, M. Jourdan
    J. Appl. Phys. **100**, 103904 (2006)

15. *Micromagnetism and magnetization reversal of embedded ferromagnetic elements*
    S. Blomeier, P. Candeloro, B. Hillebrands, B. Reuscher, A. Brodyanski, M. Kopnarski
    Phys. Rev. B, **74**, 184405 (2006).

## 7.2 in press

1. *Resonant and non-resonant scattering of dipole-dominated spin waves from a region of inhomogeneous magnetic field in a ferromagnetic film*
   M.P. Kostylev, A.A. Serga, T. Schneider, T. Neumann, B. Leven, B. Hillebrands, R.L. Stamps
   Phys. Rev. B., in press.

2. *Parametically stimulated recovery of microwave signal stored in stadnding spin-wave modes of a magnetic film*
   A.A. Serga, A.V. Chumak, A. André, G.A. Melkov, A.N. Slavin, S.O. Demokritov, B. Hillebrands
   Phys. Rev. Lett., in press.

3. *Induced anisotropies in exchange-coupled systems on rippled substrates*
   M.O. Liedke, B. Liedke, A. Keller, B. Hillebrands, A. Mucklich, S. Facsko, J. Fassbender
   Phys. Rev. B, in press.

4. *Spin dynamics in Magnetic Nanostructures: Micro-Brillouin Light Scattering Spectroscopy*
   V.E. Demidov, S.O. Demokritov, B. Hillebrands
   The Encyclopedia of Materials - Science and Technology (EMSAT), in press.

## 7.3 submitted

1. *Direct observation of domain wall structures in curved permalloy wires containing an anti-notch*
   C.W. Sandweg, N. Wiese, D.R. McGrouther, S.J. Hermsdoerfer, H. Schultheiss, B. Leven, B. Hillebrands, J.N. Chapman
   submitted to J. Appl. Phys..
2. *Exchange interaction and magnetic domain formation in periodically inhomogeneous magnetic media*
   S. Blomeier, B. Hillebrands, B. Reuscher, A. Brodyanski, M. Kopnarski, R.L. Stamps
   submitted to Phys. Rev. B.
3. *Observation of coherence and partial decoherence of quantized spin waves in nano-scaled magnetic ring structures*
   H. Schultheiss, S. Schäfer, P. Candeloro, B. Leven, B. Hillebrands, A.N. Slavin
   submitted to Phys. Rev. Lett..
4. *Influence of the* $L2_1$ *ordering degree on the magnetic properties in* $Co_2MnSi$ *Heusler films*
   O. Gaier, J. Hamrle, S.J. Hermsdoerfer, B. Hillebrands, Y. Sakuraba, M. Oogane, Y. Ando
   submitted to J. Appl. Phys..
5. *Ex-vivo investigations on the friction behavior of amorphous carbon coated ureteral stents*
   L. Kleinen, U. Böde, N. Laube
   submitted to Diamond and Related Materials.

## 7.4 Ph.D. theses

1. *Ionenstrahlinduzierte magnetische Mikrostrukturierung zwischenschicht-austauschgekoppelter Fe/Cr/Fe-Trilagen*
   Steffen Blomeier, Ph.D. thesis, Technische Universität Kaiserslautern, 2007.
2. *The role pf patterning for the magnetization reversal in the exchange bias systems*
   Maciej Oskar Liedke, Ph.D. thesis, Technische Universität Kaiserslautern, 2007.
3. *Studies of the magnetization dynamics in micron sized elements*
   Patricia Martín Pimentel, Ph.D. thesis, Technische Universität Kaiserslautern, 2007.
4. *Modifikation der Grenzflächenrauigkeit durch niederenergetischen Ionenbeschuss in magnetischen Tunnelstrukturen zur Reduktion der Néel-Kopplung*
   Peter Andreas Beck, Ph.D. thesis, Technische Universität Kaiserslautern, 2007.

# Chapter 8: Conferences, Workshops, Schools, Seminars

(shown in chronological order with the speaker named)

## 8.1 Conferences

### 8.1.1 Invited talks

B. Hillebrands:
*Dynamics in small magnetic elements for magnetoelectronic applications*
Japan-Germany Joint Workshop, Tokyo, Japan, November 2006

B. Hillebrands:
*Linear and nonlinear optics with new light: optics with spin waves*
International Workshop on Spin Dynamics in Restricted Geometry, Seoul, Korea, May 2007

B. Hillebrands:
*Observation of nonlinear phase splitting of spin-wave packets using phase sensitive Brillouin light scattering spectroscopy*
ISAMMA 2007, Jeju, Korea, May 2007

B. Hillebrands:
*Linear and nonlinear optics with new light: optics with spin waves – plenary talk*
52nd Annual Conference of the South African Institute of Physics (SAIP), Johannesburg, South Africa, July 2007

A.A. Serga:
*Brillouin light scattering spectroscopy of nonliner spin waves*
International Conference “Functional Materials” (ICFM-2007), Partenit, Ukraine, October 2007

B. Hillebrands:
*Linear and nonlinear optics with new light: optics with spin waves – plenary talk*
MML, Perth, Australia, October 2007

### 8.1.2 Contributed talks and posters

B. Leven:
*Microwave assisted switching in* $Ni_{81}Fe_{19}$ *elements*
10th Joint MMM/Intermag Conference, Baltimore, USA, January 2007

B. Hillebrands:
*Observation of partial decoherence of quantized spin waves in nanoscaled magnetic ring structures*
10th Joint MMM/Intermag Conference, Baltimore, USA, January 2007

J. Hamrle:
*Magnetic and magneto-optical properties of* $Co_2FeSi$ *and* $Co_2Cr_{0.6}Fe_{0.4}Al$ *Heusler compounds*
10th Joint MMM/Intermag Conference, Baltimore, USA, January 2007

N.A. Sergeeva:
*Self-generation of soliton-like spin wave pulses in magnetic-film-based active ring under external pumping*
11th Colloquium of Louis Néel, Lyon, March 2007

B. Hillebrands:
*Huge quadratic magneto-optical Kerr effect and its modification by ion irradiation in* $Co_2FeSi(100)$
ISAMMA 2007, Jeju, Korea, May 2007

B. Hillebrands:
*Observation of coherence and of partial decoherence of quantized spin waves in nanoscaled magnetic ring structures*
ISAMMA 2007, Jeju, Korea, May 2007

A. Chumak:
*Evolution of magnon spectrum under parallel parametric pumping in perpendicularly magnetized ferrite film*
Seventh International Young Scientists' Conference on Applied Physics, Kyiv, Ukraine,
June 2007

J. Hamrle:
*Unique magnetic and magneto-optical properties of the* $Co_2FeSi$ *Heusler compound and their modification by ion irradiation*
13th Czech and Slovak Conference on Magnetism (CSMAG'07), Košice, Slovakia, July 2007

J. Hamrle:
*Unique magnetic and magneto-optical properties of the* $Co_2FeSi$ *Heusler compound and their modification by ion irradiation*
1st WUN International Conference on Spintronic Materials and Technology, York, UK,
August 2007

T. Schneider:
*Phase resolved investigation of spin-wave excitation by microwave pulses*
3rd Seeheim Conference on Magnetism (SCM07), Frankfurt a.M., Germany, August 2007

T.M. Neumann:
*BLS observation of thermal modes in YIG films on GGG substrate*
International Conference "Functional Materials" (ICFM-2007), Partenit, Ukraine,
October 2007

O. Gaier:
*Modification of spin-orbital coupling by* $Ga^+$ *and* $He^+$ *ion irradiation in the* $Co_2FeSi$ *Heusler compound*
MML, Perth, Australia, October 2007

B. Hillebrands:
*Phase resolved Brillouin light scattering spectroscopy investigation of linear and nonlinear spin wave packets*
MML, Perth, Australia, October 2007

H. Schultheiss:
*Observation of coherence and of partial decoherence of quantized spin waves in nanoscaled magnetic ring structures*
MML, Perth, Australia, October 2007

H. Schultheiss:
*Field dependency of quantized spin waves in nano-scaled magnetic ring structures*
MML, Perth, Australia, October 2007

### 8.1.3 Contributions to the DPG Frühjahrstagung

10 contributions: DPG Frühjahrstagung, Regensburg, March 2007

## 8.2 Workshops and Schools

### 8.2.1 Invited talks

B. Hillebrands:
*Dynamics in magnetic micro- and nanostructures*
Workshop "Dynamics of Solids", University of Witwatersrand, Johannesburg, South Africa, July 2007

### 8.2.2 Contributed talks and posters

H. Schultheiss:
*Observation of coherence and of partial decoherence of quantized spin waves in nanoscaled ring structures*
381th WE-Heraeus Seminar, Bad Honnef, January 2007

S. Hermsdörfer:
*Microwave assisted switching in* $Ni_{81}Fe_{19}$ *elements*
Fast Magnetic Imaging Workshop, TU Kaiserslautern, October 2007

S. Hermsdörfer:
*Spin waves in semi-circular Permalloy ring segments in the presence off domain walls*
Fast Magnetic Imaging Workshop, TU Kaiserslautern, October 2007

P. Martín Pimentel:
*Magnetization dynamics in magnetic logic devices*
Fast Magnetic Imaging Workshop, TU Kaiserslautern, October 2007

T. Schneider:
*Phase resolved Brillouin light scattering spectroscopy investigation of linear and nonlinear spin wave packets*
Fast Magnetic Imaging Workshop, TU Kaiserslautern, October 2007

T. Schneider:
*Space-, time- and phase-resolved Brillouin light scattering investigations of spin waves*
Fast Magnetic Imaging Workshop, TU Kaiserslautern, October 2007

H. Schulthheiss:
*Micro-focus Brillouin Light Scattering Spectroscopy of Magnetization Dynamics in Spin Momentum Transfer Devices*
Fast Magnetic Imaging Workshop, TU Kaiserslautern, October 2007

H. Schultheiss:
*Observation of coherency and of partial decoherency of quantized spin waves in nanoscaled magnetic ring structures*
Fast Magnetic Imaging Workshop, TU Kaiserslautern, October 2007

## 8.3 Meetings

B. Leven:
*Progress of micro-focus Brillouin light scattering spectroscopy*
6 Month Meeting SPINSWITCH, Poznan, Poland, March 2007

J. Hamrle:
*Spin-orbit coupling and magnetic anisotropy in* $Co_2$*-based Heusler alloys*
Meeting of the DFG Research Unit 559 and 3rd Meeting of NEDO International Joint research, Wiesbaden, September 2007

H. Schultheiss:
*Micro-focus Brillouin Light Scattering Spectroscopy of Magnetization Dynamics in Spin Momentum Transfer Devices*
Meeting of the DFG Research Unit 559 and 3rd Meeting of NEDO International Joint research, Wiesbaden, September 2007

B. Leven:
*Dynamic characterization of TMR- and nanowire logic elements*
30 Month Meeting MAGLOG, Orsay, France, October 2007

B. Leven:
*Financing and reporting in EU research training networks in the 6th framework programme*
12 Month Meeting SPINSWITCH, Lisbon, Portugal, October 2007

## 8.4 Invited colloquia

B. Hillebrands:
*Lineare und nichtlineare Optik mit Spinwellen*
Physikal. Kollog., Technische Universität Braunschweig, Germany, January 2007

B. Hillebrands:
*New aspects of magnetization dynamics: linear and nonlinear optics with spin waves*
Physical Colloquium, University of Poznan, Poland, March 2007

B. Hillebrands:
*Lineare und nichtlineare Optik in neuem Licht: Optik mit Spinwellen*
Physikal. Kollog., TH Karlsruhe, May 2007

B. Hillebrands:
*Lineare und nichtlineare Optik in neuem Licht: Optik mit Spinwellen*
Physikal. Kollog., Universität Marburg, May 2007

B. Hillebrands:
*Physik mit neuem Licht: Optik und Materialwissenschaften mit Spinwellen*
Kolloquium des FB Chemie, TU Kaiserslautern, May 2007

B. Hillebrands:
*Brillouin light scattering spectroscopy: a tool for understanding magnetization dynamics and spin wave physics*
Physical Colloquium, Department of Radiophysics, Kiev Taras Shevchenko National University, Kiev, Ukraine, June 2007

B. Hillebrands:
*Lineare und nichtlineare Optik in neuem Licht: Optik mit Spinwellen*
Kolloquium des SFB 559, Universität Hamburg, July 2007

## 8.5 Seminars

P. Martín Pimentel:
*Micro and nano structures for ultrafast switching studies in SAF element*
Seminar, AG Oesterschulze, TU Kaiserslautern, November 2006

P. Martín Pimentel:
*Magneto-optical studies of the magnetization in* $Ni_{81}Fe_{19}$ *elements*
Seminar, IMEC, Leuven, Belgium, November 2006

S. Hermsdörfer:
*Time resolved measurement techniques: Time resolved MOKE (Microwave assisted switching) & Brillouin light scattering*
Seminar AG Miyazaki/Ando, Tohoku University, Sendai, Japan, November 2006

L. Kleinen:
*Oberflächenmodifikation mit Plasmatechnologie für bio/medizinische Anwendungen*
Seminar, IDST, Rheinbreitbach, Germany, May 2007

B. Hillebrands:
*Linear and nonlinear optics with new light: optics with spin waves*
Seminar, Department of Electrical Engineering, National University of Singapore, October 2007

H. Schultheiss:
*Brillouin Light Scattering Spectroscopy of Magnetization Dynamics in Nano-scaled Devices*
Seminar, AG Stamps, University of Western Australia, Perth, Australia, October 2007

## 8.6 Contributions to other meetings

S. Hermsdörfer:
*Spin waves in semi-circular Permalloy ring segments in the presence of domain walls*
Berichtskolloquium SPP1133, Bad Honnef, Germany, April 2007

H. Schultheiss:
*Field dependency of quantized spin waves in nano-scaled magnetic ring structures*
Berichtskolloquium SPP1133, Bad Honnef, Germany, April 2007

B. Leven:
*How to characterize MTJs dynamically - an overview on Kerr microscopy and Brillouin light scattering microscopy*
Kick-Off Meeting HEUSPIN, Kahl/Main, Germany, September 2007

## 8.7 Contributions of the Institute for Thin Film Technology

### 8.7.1 Contributed talks and posters

L. Kleinen:
*Reduction of crystalline biofilm formation on medical implants by amorphous carbon coatings*
European BioPerspectives 2007, Cologne, Germany, June 2007

L. Kleinen:
*Reduction of crystalline biofilm formation on medical implants by amorphous carbon coatings*
EuroNanoforum 2007, Nanotechnology in Industrial Applications, Düsseldorf, Germany, June 2007

L. Kleinen:
*Ex-vivo investigations on the friction behavior of amorphous carbon coated ureteral stents*
18th European Conference on Diamond, Diamond-Like Materials, Carbon Nanotubes and Nitrides, Berlin, Germany September 2007

### 8.7.2 Meetings

L. Kleinen:
*Möglichkeiten der Verbesserung der bakterienbiofilmreduzierenden Eigenschaften amorpher Kohlenstoffe durch Wirkstoffankopplung*
6 Month Meetings BIOMINMED, Rheinbreitbach, Germany, July 2007

U. Böde:
*Einfluss der Freier Oberflächenenergie amorpher Kohlenstoffschichten auf die Bakterienbiofilmbildung*
6 Month Meetings BIOMINMED, Rheinbreitbach, Germany, January 2007

L. Kleinen:
*Charakterisierung der zur Erarbeitung bakterienbiofilmreduzierender Kohlenstoffschichten eingesetzten Plasmen*
6 Month Meetings BIOMINMED, Rheinbreitbach, Germany, January 2007

### 8.7.3 Contributions to other meetings

| | |
|---|---|
| 5 contributions: | Hannover-Messe, Hannover, April 2007 |
| 1 contribution: | Biotechnica, Hannover, October 2007 |
| 19 contributions: | Seminar des NanoBioNet e.V., Rheinbreitbach, May 2007 |

## 8.8 Awards

L. Kleinen:
Cologne BioInnovation Award 2007 (2. Platz) im Rahmen der European BioPerspectives verliehen für hervorragende Forschungs- und Entwicklungsleistungen im Bereich der Biotechnologie mit besonderen praktischen Anwendungs- und wirtschaftlichen Verwertungsmöglichkeiten vergibt.

# Appendix: Impressions from 2007

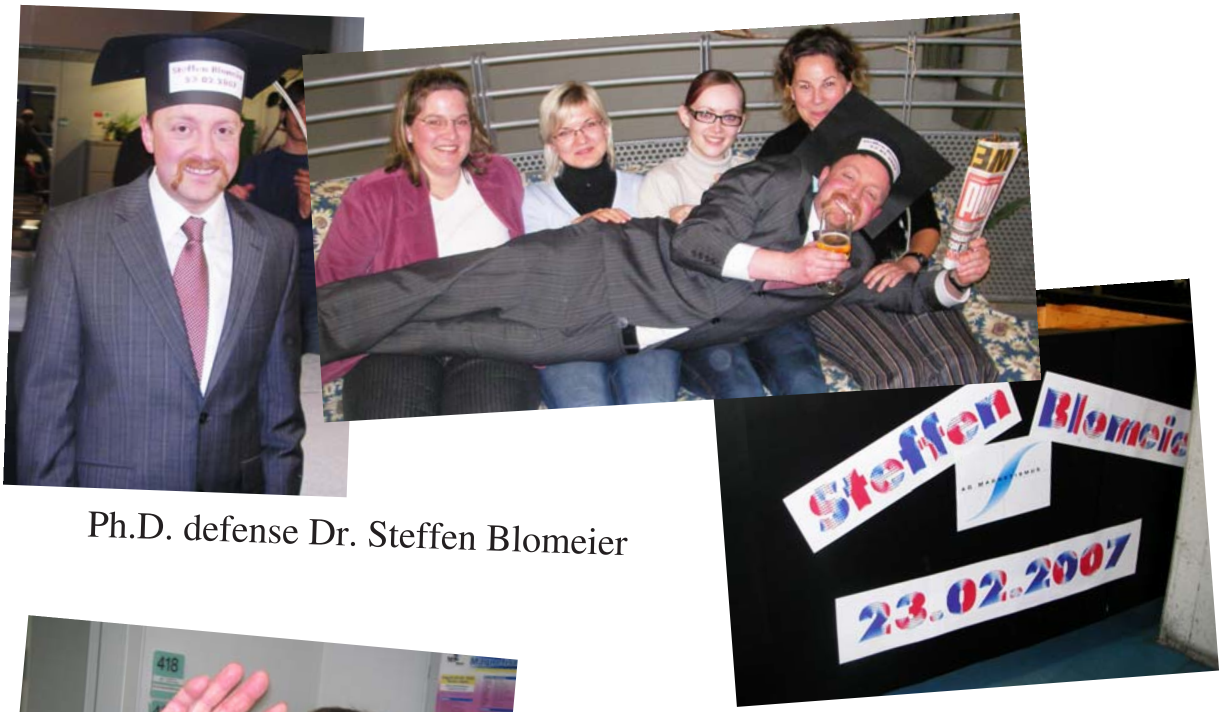

Ph.D. defense Dr. Steffen Blomeier

Retirement Bernd Pfaff

Ph.D. defense Dr. Oskar Liedke

Ph.D. defense Dr. Patricia Martín Pimentel

Ph.D. defense Dr. Andreas Beck